THIN CIRCULAR METAL PLATES SUBJECTED TO LOCALISED IMPULSIVE LOADS

by

A.M. Radford

1995

Submitted to the University of Cape Town in partial fulfilment of the requirements for the Degree of Master of Science.

ABSTRACT

This thesis presents a theoretical model to predict the response of thin circular metal plates subjected to localised impulsive loads. These predictions are compared to experimental data and a finite element model.

The theoretical model is described by two models where the first model predicts the plate deformation and the second model, using the deformation from the first, predict the strains in the plate. The first model or theoretical displacement model presents a stepwise velocity field approach, in which it is assumed that the explosive burns as a set of discretised rings spreading from the centre of the plate to the outer radius of the explosive. For each ring a velocity field for the plate is developed, and after including strain rate effects, a corresponding displacement is calculated. The total final displacement is determined by summing each of the individual displacements. The predictions are compared with all experimental data and a satisfactory correlation is found for both the mid-point displacements and the final plate shape. The second model or theoretical strain model uses the final displaced shape calculated using the theoretical displacement model to determine the strain in the deformed plates, with results being compared to uniaxial tensile strain and mean cap diameters obtained from experimentation. The maximum strain at failure calculated using the theoretical strain model gave good correlation to the uniaxial tensile strain and its position correlated well with the mean cap diameter.

The experimental data compared to the predictions made by the theoretical model was obtained from Bodner and Symonds [4] and from tests conducted on mild steel circular plates, with a thickness of 1.6mm and outer plate radius of 100mm. The plates were loaded over the load diameters 18.3mm, 25mm, 33mm and 40mm using a plastic explosive placed onto a polystyrene foam pad and located centrally on the plate. Loading of the plates was varied to give deformations up to the onset of and including plate tearing. The plates failed under tensile tearing, forming a circular cap

that blew out of the centre of the plate with diameters proportional to the load diameter.

Furthermore the theoretical displacement model was compared to a finite element model. The finite element model assumed that the pressure applied by the explosive acted over the load area only, and no attempt was made to model its spread. For the smaller load diameters relatively low impulses resulted in high pressures, causing numerical instabilities to form in the finite element solution. The impulses required for numerical stability were lower than the experimentally determined impulse and hence, no comparison between the model and experimentation could be made. However, comparisons between the finite element model and theoretical displacement model showed that the deflections predicted by the finite element model, were greater than those predicted by the theoretical displacement model.

DECLARATION

I, Anthony Michael Radford, declare that this thesis is essentially my own work and has not been submitted in this or any other form for a degree at any other university.

ACKNOWLEDGEMENTS

The author would like to thank the following:

1. G.N. Nurick for his advice, support and many hours spent conducting experimentation.
2. M. Eastman, G.P. Mitchell and G.H. Farrow for their assistance with developing the finite element model.
3. J. Fitton for his photographic work.
4. The Mechanical Engineering work shop staff for their general assistance.
5. The Department of Mechanical Engineering and Cerecam both at the University of Cape Town for their financial assistance.
6. My Parents for their support and financial assistance.
7. K. Gifford Nash for her support.

NOMENCLATURE

R_b	Burn point
R_0	Load radius
R	Outer plate radius
r	Plate radius
ϕ	Shape function
$\theta_{1,2}$	Gradient function
$\varphi_{1,2}$	Gradient function constant
$Z1,2$	Gradient function constant
V_0	Initial velocity amplitude
t	Time
t_f	Response time
V	Velocity function
$\dot{W}$	Velocity field
I_E	Applied impulse
I_c	Calculated impulse
$\tilde{I}_c$	$I_c = V_0 \cdot \tilde{I}_c$
H	Plate thickness
ρ	Plate density
ν	Possion's ratio
W	Displacement field
E_p	Plastic strain energy
E_k	Initial kinetic energy
σ_0'	Dynamic yield stress
$\dot{\varepsilon}_r$	Radial strain rate
$\dot{\varepsilon}_{ave}$	Average radial strain rate
W_T	Total displacement
ε	Strain in the deformed plate
r_{ave}	Radius at which strain occurs

t_B	Explosive burn time
P_t	Maximum pressure for a triangular pressure pulse

The subscripts R, L and RL refer to the shape function group.

TABLE OF CONTENTS

LIST OF FIGURES

LIST OF TABLES

1. LITERATURE REVIEW

The response of thin plates fixed at the outer edges and subjected to impulsive loading conditions has been studied for many years. Nurick and Martin [1,2] present an overview of the theoretical and experimental results from which it is evident that most of the investigations deal with a plate that is loaded uniformly over the entire plate area. The predictions for these cases include the final mid-point displacement, time response and in some cases the shape of the plate. The correlation between the predictions and experimental results are favourable for both mid-point displacements and final deformation shape. Farrow, Nurick and Mitchell [3] used the Abaqus finite element code to predict the large inelastic (Mode I) deformation of circular plates under uniformly distributed impulsive loads. Plate displacements, deformation shapes, residual strains and dynamic yield stress predictions show satisfactory correlation with experimental and analytical results. However, the case of plates centrally loaded has received relatively little consideration.

Analytical methods have been employed in order to predict the deformation of centrally loaded fully edged clamped circular plates. The mode approximation technique has proven to give good predictions for the mid-point displacements, but not for the plate shapes, as reported by Bodner and Symonds [4], and Symonds and Wierzbicki [5]. The material (steel and titanium) used was strain rate sensitive, and this was incorporated in their model. It was assumed that the explosive imparted a rectangular pressure pulse over the load diameter of the plate and no attempt was made to model the way in which the pressure spread outside the load area. These predictions were compared to experimental data in which the load ratios used (i.e. load radius to plate radius) were 1/3, 1/2 and 1. Another method used to predict the deformation of plates under central blast load conditions was that reported by Florence [6]. Similarly, it was assumed that the explosive applied a rectangular pressure pulse to the plate with a diameter equal to that of the load diameter. Again

no attempt was made to model the way in which the pulse from the explosive spreads outside the load diameter. It was further assumed that the plate material undergoing plastic deformation followed the Tresca yield condition. The blast pressure on detonation was assumed to instantaneously rise to a peak, followed by a monotonic decay over time. This allowed a steady progress through the various mechanisms of deformation. These deformation mechanisms relate to the movement of plastic hinges through the plate. Each mechanism is determined by the load diameter and plastic hinges reaching the centre of the plate and the outer diameter of the plate.

Predictions of simply supported plates subjected to localised blast loads have been reported by Lui and Stronge [7], however no attempt was made to correlate the predictions with experimental data.

The prediction of plate failure through tensile tearing or other modes has been reasonably well covered for fully loaded plates. Such predictions of plate failure include those presented by Teeling-Smith and Nurick [8] and Thomas [9]. Together with these predictions McClintock, Zhou and Wierzbicki [10] presented a numerical approach to predicting thinning and failure of plates at built-in supports.

However, very few predictions of plate tearing for localised loading conditions have been made. Duffey [11] presents an over view on the dynamic rupture of shells, wherein it is stated that very few predictions for ductile material failure by actual separation are presented. This lack of predictions coupled with the lack of available data makes the prediction of ductile material through separation difficult. However, Duffey does go on to say that it appears that ductile failure of dynamically loaded shells can be initiated as a result of tensile type failure. Florence [6] using the movement of plastic hinges towards the centre of the plate and plate radius, made some predictions as to the load radius to plate radius ratio required for the two hinges to simultaneously reach the centre and outer plate radius. This ratio was found to be 0.56. This suggests that for a load to plate radius ratio of 0.56 tearing of the plate will occur "simultaneously" at the plate centre and plate radius.

2. INTRODUCTION

This document considers circular plates fixed at the boundaries and subjected to localised loading conditions, for which a theoretical model is developed in an attempt to predict the plate deformation and resulting strain. The theoretical model is described by two models where the first model uses the mode approximation technique to predict the plate deformation and the second model uses this deformation to predict the strain in the plate. The predicted deformations and strains are compared to experimental data and predictions made using a finite element model.

The theoretical model, using the mode approximation technique, predicts plate mid-point displacement, final deformation shape and strain in the deformed plate, up to the onset of tearing. The plates are assumed to be thin enough to be considered as membranes (that is no bending effects are taken into account) and strain rate effects are included. Although the deformation process is globally dynamic the failure criterion is assumed to be quasistatic uniaxial tensile strain at failure. It is also assumed that the explosive used to impulsively load the plate is detonated at the centre and moves outwards as a ring of burning explosive. The total burn time (approximately 1-2 μs) is very small in comparison with the response time of the plate (approximately 100-150 μs, as reported by Bodner and Symonds [4]), that is the burning time is considered to be complete at the response starting time ($t = 0$). The burning process is discretised, and at each of these discrete burn rings it is assumed that the explosive imparts a velocity field onto the plate causing deformation of the plate. The velocity fields give a velocity over the entire plate area. Along with the discretised burn rings, the rest of the plate, that is from the load diameter to the plate diameter, is discretised in a similar way. At each of these discretised points across the plate the deformations are summed to give the total deformation of the plate. Using the total deformation at each discretised point, the strain in the plate can be found

using the ratio of the deformed and undeformed lengths between each discretised point.

The predictions of the theoretical model are compared with experimental data for load diameters of 18.3mm, 25mm, 33mm, 40mm (with a plate diameter of 100mm) and experimental data generated by Bodner and Symonds [4].

As a further comparison, the predictions made by the theoretical model are compared to predictions made using a finite element model. The finite element model criteria used are the same as those used by Farrow, Nurick and Mitchell [3] in which strain rate sensitivity, non-linear geometry and material effects are incorporated. Farrow, Nurick and Mitchell [3] attained good comparisons with experimental results for a 40 element mesh with convergence of the solution taking place at around 4 elements. However, for localised loading conditions it was found that around 400 elements were necessary in order to achieve numerical stability for relatively low impulses in the solution. The impulsive load applied to the plate was taken to act over the localised load diameter only, and no attempt was made to model its spread.

3. THEORETICAL MODEL

The following model is proposed using the mode approximation technique and predicts the deformation of and strain in thin metal plates subjected to localised impulsive loads. The theoretical model is described by two models where the first, or theoretical displacement model predicts the plate deformation and the second, or theoretical strain model uses these deformations to predict the strain in the deformed plates. The theoretical displacement and strain models, as well as the plate discretisation process required by both these models, are discussed in brief and then separately in detail later on in this section.

3.1 SUMMARY OF ANALYSIS

1. Both the theoretical displacement and strain models require that the plate be discretised. The models predict the deformation at and strain between each discretised point. This discretisation process is carried out over the load and non-load plate areas. Discretising the plate over the load area results in pairs of burn points R_b on either side of the plate centre, while the rest of the plate, that is, from the load to the plate radius, is discretised in a similar way.

2. Shape functions (ϕ) are used to define the velocity of the plate for each burn point. These shape functions have a magnitude that varies from unity at each of the burn points ($\phi(R_b) = 1$), to zero at the plate radius ($\phi(R) = 0$), and are recalculated at each of the burn points, since the shape changes with each burn point.

3. Velocity functions (V) define the plate velocity applied by the shape functions to the plate. These velocity functions have a maximum initial velocity V_0 when time is zero ($V(t=0)=V_0$) and zero velocity at the time when the plate has deformed completely ($V(t=t_f)=0$). Multiplying the velocity functions (V) by each shape function (ϕ) gives the velocity fields ($\dot{W}$) for each burn point ($\dot{W}=\phi \cdot V$).

4. The initial velocity V_0 for each velocity function is calculated by equating the impulse I_E applied to the plate by the explosive to the calculated impulses I_c applied to the plate by each velocity field for each burn point ($I_E=\sum I_c$). The calculated impulse I_c is rewritten as $I_E=\sum \tilde{I}_c \cdot V_0$, and hence $V_0=\sum \tilde{I}_c / I_E$. Once the initial velocity has been calculated the velocity fields can be integrated with respect to time to give the displacement fields for each of the burn points ($W=\int \dot{W} dt$).

5. The displacement fields define the plate deformation with time for each burn point. In order to find the total deformation of the plate it is necessary to calculate the time for each displacement field to come to rest, at each burn point. These times are called the response times t_f.

6. The response times t_f are calculated by equating the initial kinetic energy E_k, applied to the plate by the velocity fields, when $t=0$, to the plastic energy E_p absorbed by the displacement fields for each burn point ($\sum E_k=\sum E_p$). The plastic energy absorbed is dependent on the dynamic yield stress σ_0'.

7. The dynamic yield stress σ_0' for each burn point is determined by the average radial strain rate $\dot{\varepsilon}_{ave}$ for each displacement field at each burn point. The dynamic yield stress is then substituted into the plastic energy equation E_p and the response times calculated. Thereafter, the final displacement fields $W(t_f)$ for each burn point can be found.

8. The final displacement fields for each burn point are then summed to give the total displacement of the plate W_T.

9. Once the total displacement W_T at each discretised point has been determined, the average strain ε using the ratio of the lengths between two respective discretised points in the deformed and undeformed state can be calculated.

3.2 PLATE DISCRETISATION

It is necessary to divide the discretisation of the plate into two sections. The first section is the load area of the plate and the second section is the rest of the plate, that is from the load radius to the plate radius. Each of these sections are described below.

After detonation it is assumed that the explosive burns radially outwards. This process of burning is discretised as a discrete series of rings. These discrete rings start at the centre of the plate and increase in radius R_b, up to the explosive's outer radius R_0, as shown in Figure 3.1.

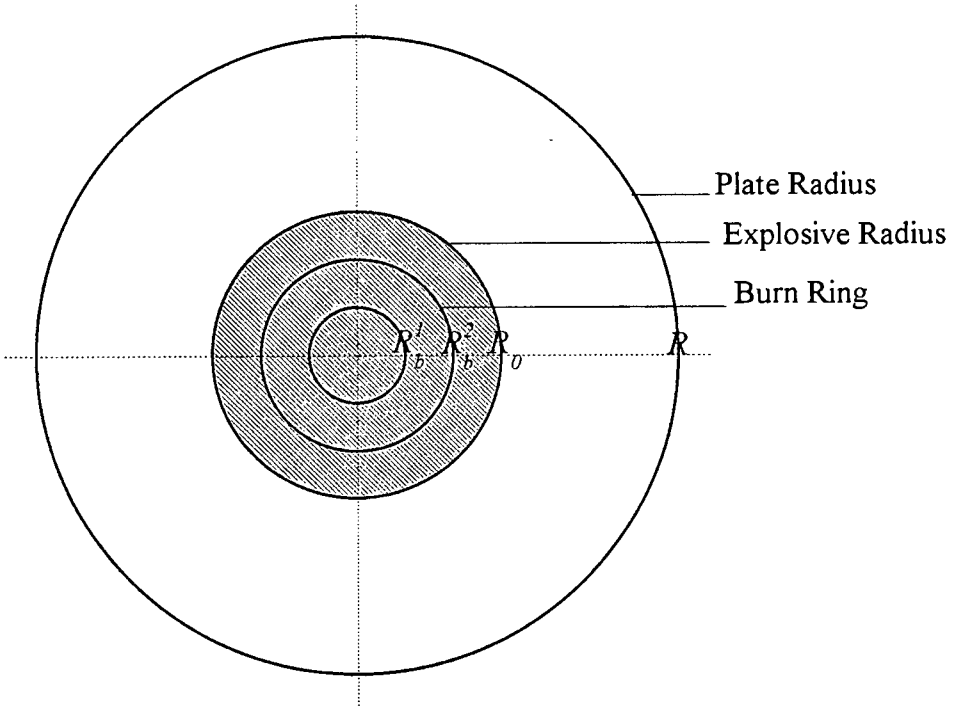

Figure 3.1 Discretisation of the plate from the centre up the load radius.

Since the system is axisymmetric it is possible to simplify this analysis by only considering the plate in one dimension, along a radius. Each burn ring will thus be considered as a pair of burn points on this radius.

The remainder of the plate from the load radius to the outer plate radius, is discretised in a similar way as shown in Figure 3.2. Again, due to symmetry, the discrete rings become pairs of discrete points on the plate radius.

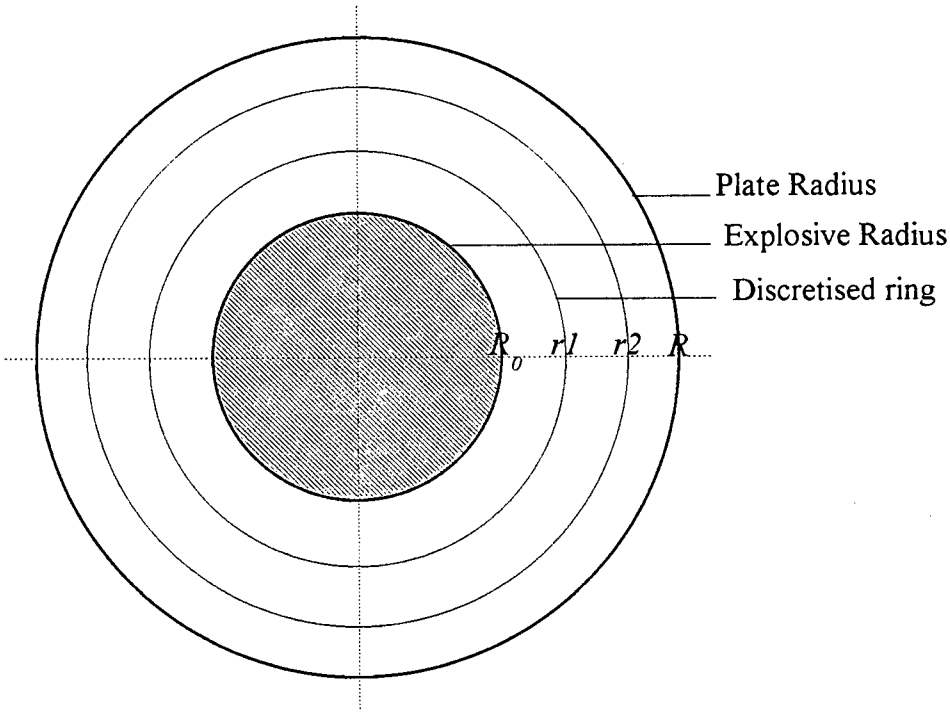

Figure 3.2 Discretisation of the plate from the load radius to the plate radius.

3.3 THEORETICAL DISPLACEMENT MODEL

The theoretical displacement model is developed as follows.

3.3.1 SHAPE FUNCTION GROUPS

For each burn ring there are two corresponding burn points with each burn point having two associated shape functions, one that spreads from the burn point to the right boundary and the other that spreads from the burn point to the left boundary. This gives four shape functions per pair of burn points, as shown in Figure 3.3, Figure 3.9 and Figure 3.10. However due to symmetry, the analysis can be further simplified by only considering the right hand side and therefore only the shape functions affecting this side. These shape functions are ϕ_R, ϕ_L and ϕ_{RL}, and form a shape function group.

Different shape functions have been derived (cubic, quadratic and linear) and are discussed in detail below.

3.3.1.1 CUBIC SHAPE FUNCTION GROUP

The cubic shape function group is shown in Figure 3.3, and the associated equations are,

Eq. 3.1 $$\phi_R(r,R_b) = A_R(R_b) + B_R(R_b)\cdot r + C_R(R_b)\cdot r^2 + D_R(R_b)\cdot r^3$$

Eq. 3.2 $$\phi_L(r,R_b) = A_L(R_b) + B_L(R_b)\cdot r + C_L(R_b)\cdot r^2 + D_L(R_b)\cdot r^3$$

Eq. 3.3 $$\phi_{RL}(r,R_b) = A_{RL}(R_b) + B_{RL}(R_b)\cdot r + C_{RL}(R_b)\cdot r^2 + D_{RL}(R_b)\cdot r^3$$

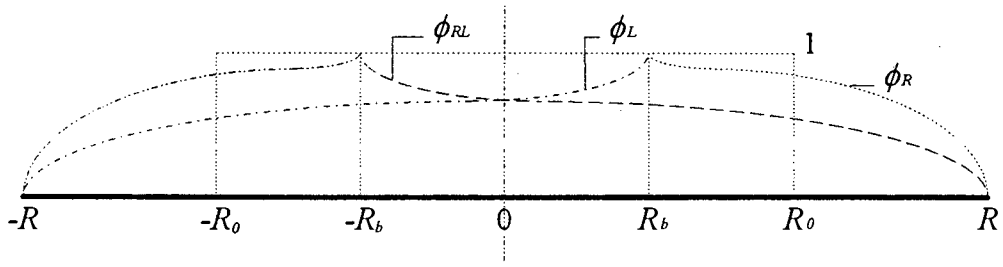

Figure 3.3 Cubic shape function group.

For this shape function group, A, B, C and D are functions of the gradient functions θ_1 and θ_2. The gradient functions θ_1 and θ_2 define the gradients of the shape functions for the burn points R_b and the plate radius R respectively as shown in Figure 3.4, Figure 3.5 and Figure 3.6.

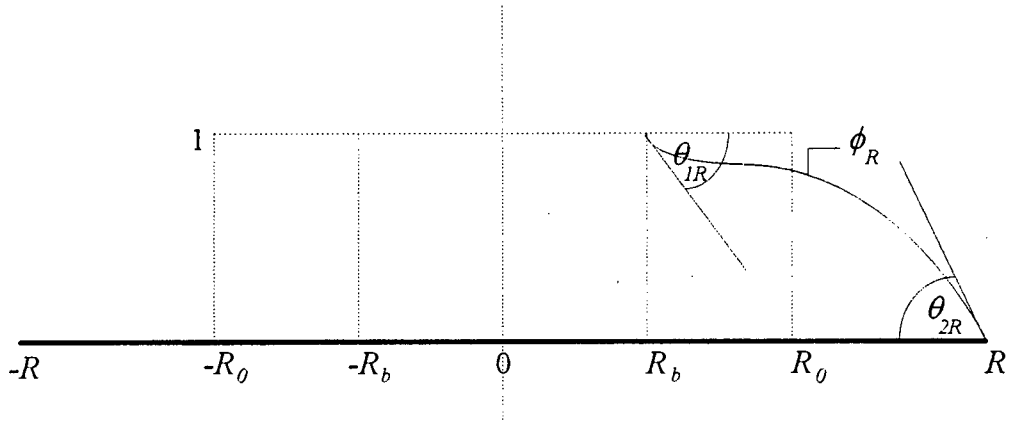

Figure 3.4 Illustrating the gradient of the cubic shape function ϕ_R at R_b and R, defined by θ_1 and θ_2.

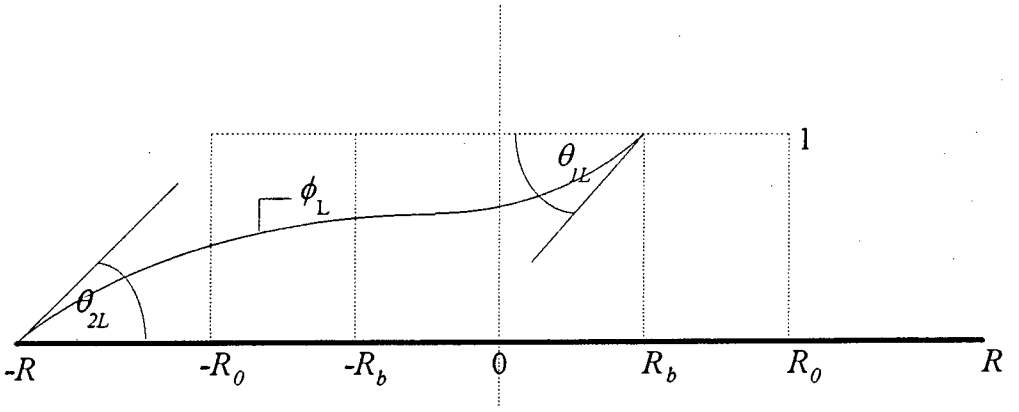

Figure 3.5 Illustrating the gradient of the cubic shape function ϕ_L at R_b and R, defined by θ_1 and θ_2.

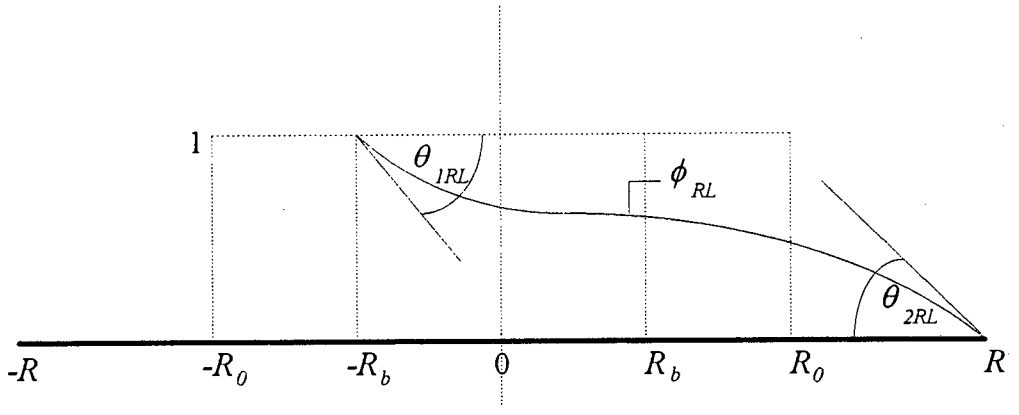

Figure 3.6 Illustrating the gradient of the cubic shape function ϕ_{RL} at R_b and R, defined by θ_1 and θ_2.

For ϕ_R the value of the gradient function θ_1 decreases at the burn point R_b and the value of the gradient function θ_2 increases at the plate radius R as the burn points move from the centre of the plate to the load radius, as illustrated in Figure 3.7.

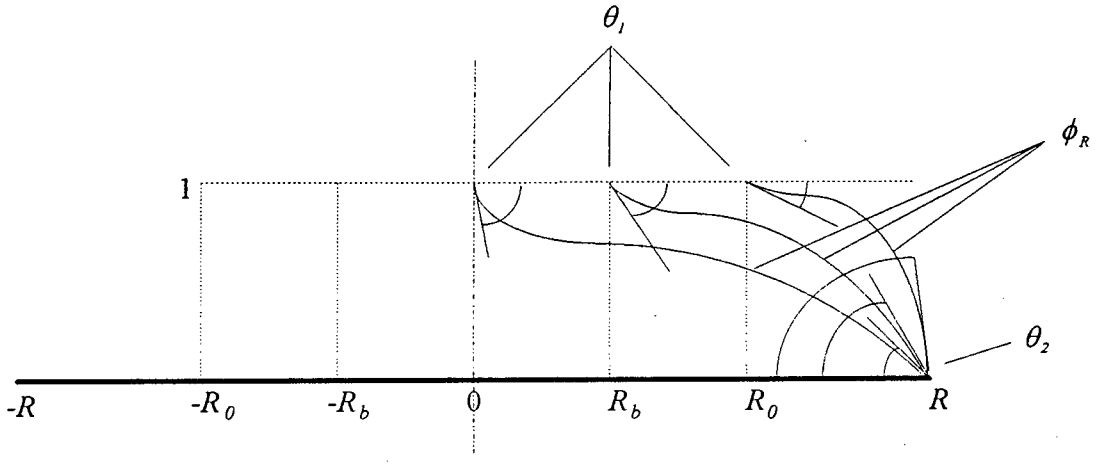

Figure 3.7 Illustrating the gradient changes of ϕ_R for the burn point R_b and the plate radius R as R_b moves from the centre of the plate to the load radius.

Concurrently for ϕ_L the value of the gradient function θ_1 at the burn point R_b increases and the value of the gradient function θ_2 decreases at the plate radius R as the burn points move from the centre of the plate to the load radius, as illustrated in Figure 3.8. Due to the symmetrical nature of ϕ_L and ϕ_{RL} the values of the gradient functions θ_1 and θ_2 for ϕ_{RL} increase and decrease in the same manner as for ϕ_L.

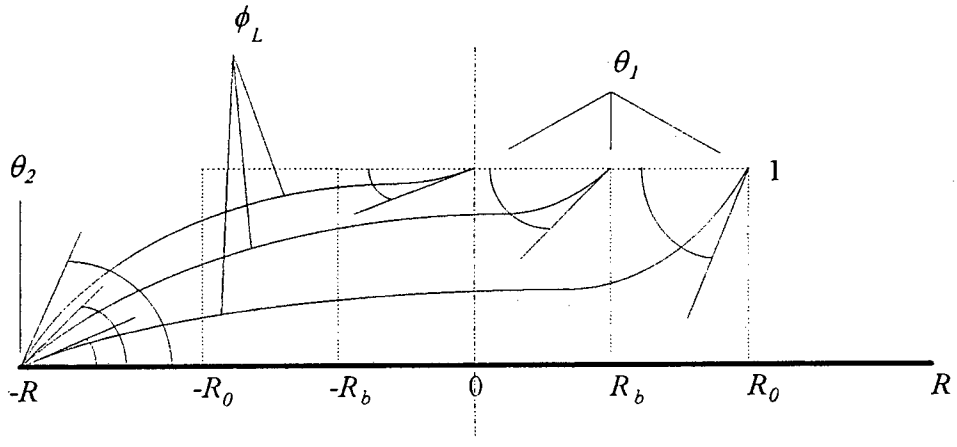

Figure 3.8 Illustrating gradient changes of ϕ_L at the burn point R_b and the plate radius R as the burn point moves from the centre of the plate to the plate radius.

The gradient functions are defined as follows,

For ϕ_R

Eq. 3.4 $$\theta_{1R}(R_b) = -\varphi_1 \cdot \tan\left(\frac{\pi}{4 \cdot R} \cdot (R - R_b)\right)^{Z1}$$

Eq. 3.5 $$\theta_{2R}(R_b) = -\varphi_2 \cdot \tan\left(\frac{\pi}{4 \cdot R} \cdot (R + R_b)\right)^{Z2}$$

For ϕ_L

Eq. 3.6 $$\theta_{1L}(R_b) = \varphi_1 \cdot \tan\left(\frac{\pi}{4 \cdot R} \cdot (R + R_b)\right)^{Z1}$$

Eq. 3.7 $$\theta_{2L}(R_b) = \varphi_2 \cdot \tan\left(\frac{\pi}{4 \cdot R} \cdot (R - R_b)\right)^{Z2}$$

For ϕ_{RL}

Eq. 3.8 $$\theta_{1RL}(R_b) = -\varphi_1 \cdot \tan\left(\frac{\pi}{4 \cdot R} \cdot (R + R_b)\right)^{Z1}$$

Eq. 3.9 $$\theta_{2RL}(R_b) = -\varphi_2 \cdot \tan\left(\frac{\pi}{4 \cdot R} \cdot (R - R_b)\right)^{Z2}$$

where φ_1, φ_2, $Z1$ and $Z2$ are chosen constants. The affects of varying each constant separately and as a group is illustrated in Appendix K. Based on these comparisons the gradient function values were chosen and are given in Table 3.1.

φ_1	35
$Z1$	0.25
φ_2	20
$Z2$	2.1

Table 3.1 Value of gradient function constants.

A, B, C and D are solved by applying the following boundary conditions to equations Eq. 3.1, Eq. 3.2 and Eq. 3.3.

$\phi = 1$ at $r = R_b$

$\phi = 0$ at $r = R$

$d\phi/dr = \theta_1$ at $r = R_b$

$d\phi/dr = \theta_2$ at $r = R$

A, B, C and D for the cubic shape function group are given in Appendix A.

3.3.1.2 QUADRATIC SHAPE FUNCTION GROUP

The quadratic shape function group shown in Figure 3.9, is made up of the shape functions ϕ_R, ϕ_L and ϕ_{RL}.

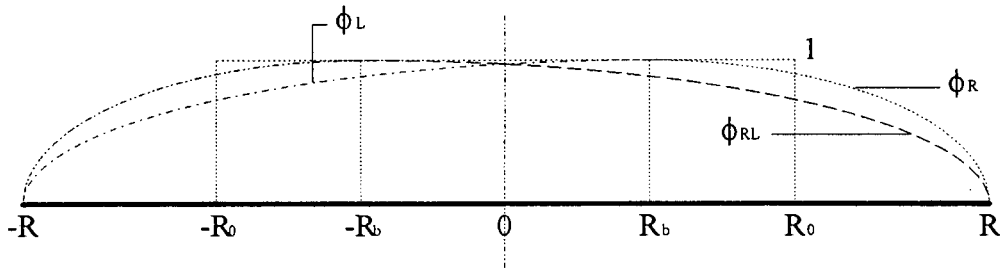

Figure 3.9 Quadratic shape function group.

The equations for the three shape functions ϕ_R, ϕ_L and ϕ_{RL}, illustrated in Figure 3.9, are defined below.

Eq. 3.10 $$\phi_R(r,R_b) = A_R(R_b) + B_R(R_b)\cdot r + C_R(R_b)\cdot r^2 + D_R(R_b)\cdot r^3$$

Eq. 3.11 $$\phi_L(r,R_b) = A_L(R_b) + B_L(R_b)\cdot r + C_L(R_b)\cdot r^2 + D_L(R_b)\cdot r^3$$

Eq. 3.12 $$\phi_{RL}(r,R_b) = A_{RL}(R_b) + B_{RL}(R_b)\cdot r + C_{RL}(R_b)\cdot r^2 + D_{RL}(R_b)\cdot r^3$$

A, *B*, *C* and *D* for the quadratic shape functions are derived by applying the boundary conditions to equations Eq. 3.10, Eq. 3.11 and Eq. 3.12, with *D* having a value of zero.

The boundary conditions for the quadratic shape function group are,

$\phi = 1$ at $r = R_b$

$\phi = 0$ at $r = R$

$d\phi/dr = \theta_1$ at $R_b = 0$

A, *B*, *C* and *D* for the quadratic shape function group are given in Appendix A.

3.3.1.3 LINEAR SHAPE FUNCTION GROUP

The linear shape function group shown in Figure 3.10 is made up of ϕ_R, ϕ_L and ϕ_{RL}.

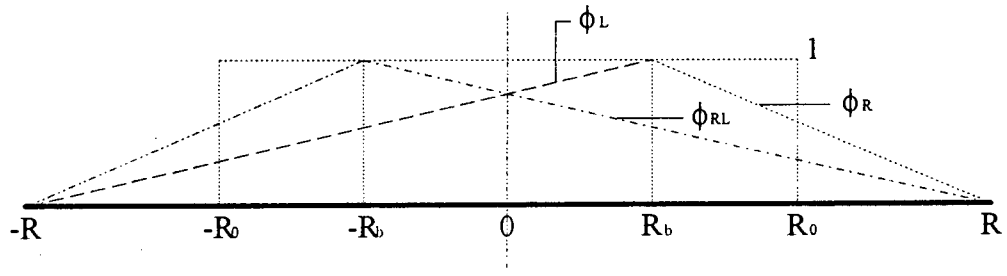

Figure 3.10 Linear shape function group.

The equations for the three shape functions, ϕ_R, ϕ_{RL} and ϕ_{RL}, illustrated in Figure 3.10, are defined below.

Eq. 3.13 $$\phi_R(r,R_b) = A_R(R_b) + B_R(R_b)\cdot r + C_R(R_b)\cdot r^2 + D_R(R_b)\cdot r^3$$

Eq. 3.14 $$\phi_L(r,R_b) = A_L(R_b) + B_L(R_b)\cdot r + C_L(R_b)\cdot r^2 + D_L(R_b)\cdot r^3$$

Eq. 3.15 $$\phi_{RL}(r,R_b) = A_{RL}(R_b) + B_{RL}(R_b)\cdot r + C_{RL}(R_b)\cdot r^2 + D_{RL}(R_b)\cdot r^3$$

A, *B*, *C* and *D* for the linear shape functions are derived by applying the boundary conditions to equations Eq. 3.13, Eq. 3.14 and Eq. 3.15, with *D* and *C* having values of zero.

The boundary conditions for the linear shape function group are,

$\phi = 1$ at $r = R_b$

$\phi = 0$ at $r = R$

A, *B*, *C* and *D* for the linear shape function are given in Appendix A.

3.3.2 VELOCITY FIELDS

Velocity fields $\dot{W}$ are defined as the shape functions ϕ multiplied by the velocity functions V, where the velocity functions have a velocity magnitude that varies from $V = V_0$ (the initial velocity amplitude) at $t = 0$ to $V = 0$ at $t = t_f$ (where t_f is the time for the plate to come to rest).

The velocity functions are defined as

Eq. 3.16 $$V_R(t) = V_0 \cdot \cos\left(\frac{\pi}{2 \cdot t_{fR}} \cdot t\right)$$

Eq. 3.17 $$V_L(t) = V_0 \cdot \cos\left(\frac{\pi}{2 \cdot t_{fL}} \cdot t\right)$$

Eq. 3.18 $$V_{RL}(t) = V_0 \cdot \cos\left(\frac{\pi}{2 \cdot t_{fRL}} \cdot t\right)$$

Multiplying the velocity functions by the shape functions gives the velocity fields

Eq. 3.19 $$\dot{W}_R(r,t,R_b) = V_R(t) \cdot \phi_R(r,R_b)$$

Eq. 3.20 $$\dot{W}_L(r,t,R_b) = V_L(t) \cdot \phi_L(r,R_b)$$

Eq. 3.21 $$\dot{W}_{RL}(r,t,R_b) = V_{RL}(t) \cdot \phi_{RL}(r,R_b)$$

3.3.3 INITIAL VELOCITY AMPLITUDE

The initial velocity amplitude V_0 is calculated by equating an impulse applied to the plate I_E to the sum of the calculated impulses I_c applied by the velocity fields, for each burn point R_b.

The calculated impulse I_c is given at $t = 0$ as

Eq. 3.22 $$dI_c(r, R_b) = dm \cdot \dot{W}(r, R_b)$$

where,

Eq. 3.23 $dm = 2 \cdot \pi \cdot r \cdot \rho \cdot H \cdot dr$ (as illustrated in Figure 3.11)

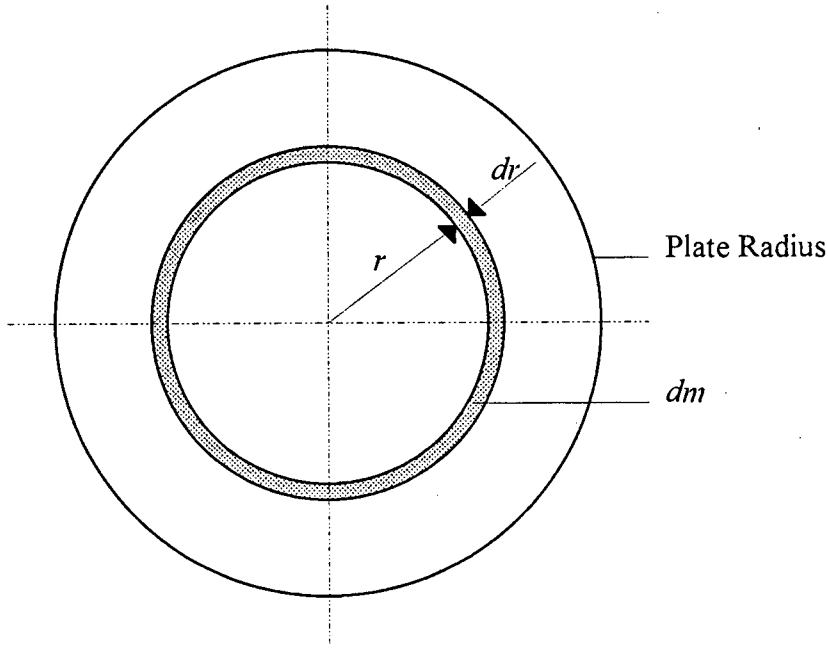

Figure 3.11 Diagram showing section of plate.

Substituting Eq. 3.23 into Eq. 3.22 gives the calculated impulse I_c in terms of dr.

Eq. 3.24 $$dI_c(r, R_b) = 2 \cdot \pi \cdot r \cdot \rho \cdot H \cdot \dot{W}(r, R_b) \cdot dr$$

The calculated impulses I_c for each velocity field $\dot{W}_R$, $\dot{W}_L$ and $\dot{W}_{RL}$, are found by substituting the velocity fields into Eq. 3.24 and integrating with respect to *r*.

For $\dot{W}_R$

Substituting the velocity field $\dot{W}_R$ Eq. 3.19 into the calculated impulse Eq. 3.24 yields

Eq. 3.25
$$I_{cR}(R_b) = 2\cdot\pi\cdot\rho\cdot H\cdot V_0\cdot \int_{R_b}^{R}\left(A_R(R_b)+B_R(R_b)\cdot r+C_R(R_b)\cdot r^2+D_R(R_b)\cdot r^3\right)\cdot r dr$$

Eq. 3.26
$$I_{cR}(R_b) = 2\cdot\pi\cdot\rho\cdot H\cdot V_0\cdot\left(1/2\cdot A_R(R_b)\cdot\left(R^2-{R_b}^2\right)+ 1/3\cdot B_R(R_b)\cdot(R^3-{R_b}^3)+1/4\cdot C_R(R_b)\cdot\left(R^4-{R_b}^4\right)+ 1/5\cdot D_R(R_b)\cdot\left(R^5-{R_b}^5\right)\right)$$

For $\dot{W}_L$

Similarly, substituting the velocity field $\dot{W}_L$ Eq. 3.20 into the calculated impulse Eq. 3.24 yields

Eq. 3.27
$$I_{cL}(R_b) = 2\cdot\pi\cdot\rho\cdot H\cdot V_0\cdot\left(\int_0^{R_b}\left(A_L(R_b)+B_L(R_b)\cdot r+C_L(R_b)\cdot r^2+D_L(R_b)\cdot r^3\right)\cdot r dr+ \int_0^{R}\left(A_L(R_b)+B_L(R_b)\cdot r+C_L(R_b)\cdot r^2+D_L(R_b)\cdot r^3\right)\cdot r dr\right)$$

Eq. 3.28
$$I_{cL}(R_b) = 2\cdot\pi\cdot\rho\cdot H\cdot V_0\cdot\left(1/2\cdot A_L(R_b)\cdot\left(R^2+{R_b}^2\right)+ 1/3\cdot B_L(R_b)\cdot\left(-R^3+{R_b}^3\right)+1/4\cdot C_L(R_b)\cdot\left(R^4+{R_b}^4\right)+ 1/5\cdot D_L(R_b)\cdot\left(-R^5+{R_b}^5\right)\right)$$

$\dot{W}_L$ and $\dot{W}_{RL}$ are axisymmetric about the centre of the plate, hence the calculated impulse applied to the plate by $\dot{W}_{RL}$ is taken into account by calculating the calculated impulse I_{cL} applied to the plate by $\dot{W}_L$.

Eq. 3.26 and Eq. 3.28 are rewritten as a function of V_0 as

Eq. 3.29 $$I_{cR}(R_b) = V_0 \cdot \tilde{I}_{cR}(R_b)$$

Eq. 3.30 $$I_{cL}(R_b) = V_0 \cdot \tilde{I}_{cL}(R_b)$$

Summing Eq. 3.29 and Eq. 3.30 for each burn point R_b over the load radius R_0, and equating to I_E gives the following

Eq. 3.31 $$I_E = \sum_{R_b=0}^{R_0} V_0 \cdot \tilde{I}_{cR}(R_b) + V_0 \cdot \tilde{I}_{cL}(R_b)$$

Rearranging Eq. 3.31 gives the initial velocity amplitude V_0.

Eq. 3.32 $$V_0 = \frac{I_E}{\sum_{R_b=0}^{R_0} \tilde{I}_{cR}(R_b) + \tilde{I}_{cL}(R_b)}$$

3.3.4 DISPLACEMENT FIELDS

The displacement fields give the displacement of the plate at time *t*. These displacement fields are derived by integrating the velocity fields with respect to time.

For $\dot{W}_R$

Integrating velocity field $\dot{W}_R$ Eq. 3.19 gives

Eq. 3.33 $$W_R(r,t,R_b) = \int_0^t \dot{W}_R(r,t,R_b)dt$$

Eq. 3.34 $$W_R(r,t,R_b) = \frac{2 \cdot V_0 \cdot t_{fR}(R_b)}{\pi} \cdot \sin\left(\frac{\pi}{2 \cdot t_{fR}(R_b)} \cdot t\right) \cdot \phi_R(r,R_b)$$

For $\dot{W}_L$

Integrating the velocity field $\dot{W}_L$ Eq. 3.20 gives

Eq. 3.35 $$W_L(r,t,R_b) = \int_0^t \dot{W}_L(r,t,R_b)dt$$

Eq. 3.36 $$W_L(r,t,R_b) = \frac{2 \cdot V_0 \cdot t_{fL}(R_b)}{\pi} \cdot \sin\left(\frac{\pi}{2 \cdot t_{fL}(R_b)} \cdot t\right) \cdot \phi_L(r,R_b)$$

For $\dot{W}_{RL}$

Integrating velocity field $\dot{W}_{RL}$ Eq. 3.21 gives

Eq. 3.37 $$W_{RL}(r,t,R_b) = \int_0^t \dot{W}_{RL}(r,t,R_b)dt$$

Eq. 3.38 $$W_{RL}(r,t,R_b) = \frac{2 \cdot V_0 \cdot t_{fRL}(R_b)}{\pi} \cdot \sin\left(\frac{\pi}{2 \cdot t_{fRL}(R_b)} \cdot t\right) \cdot \phi_{RL}(r,R_b)$$

3.1.1 RESPONSE TIMES

The times for each displacement field W_R, W_L and W_{RL}, at each burn point, to come to rest (i.e. $V = 0$) are called the response times, t_{fR}, t_{fRL} and t_{fL}. To calculate these response times an energy approach is used, with the following assumptions:

1. No bending effects are taken into account and the energy absorbed by the plate is due only to radial membrane plastic strains.
2. The residual elastic energy remaining in the plate after deformation is negligible.
3. No consideration for the change of the plate thickness H is included in this analysis.

The response times t_f are found by equating the initial kinetic energy E_k applied to the plate by the velocity fields at $t = 0$, with the plastic energy E_p absorbed by the corresponding displacement fields for each burn point.

The plastic strain energy in the plate for the displacement fields, at each burn point, is given by [8],

Eq. 3.39 $$E_p(t_f, R_b) = \pi \cdot H \int \frac{\sigma_0'(R_b)}{(1-\nu+\nu^2)} \cdot \left(\frac{\partial W(r, t_f, R_b)}{\partial r}\right)^2 \cdot r dr$$

where W is the displacement field at the response time t_f.

The initial kinetic energy E_k applied to the plate by the velocity fields $\dot{W}$, when $t = 0$, for each burn point is given by,

Eq. 3.40 $$dE_k(r, R_b) = \frac{1}{2} \cdot dm \cdot \left(\dot{W}(r, R_b)\right)^2$$

where *dm* is given by Eq. 3.23

Using Eq. 3.39 and Eq. 3.40, E_k and E_p can be calculated for each displacement and corresponding velocity field at each burn point.

For W_R and $\dot{W}_R$

Differentiating the displacement field W_R Eq. 3.34, when $t = t_{fR}$, with respect to *r*, substituting into the plastic energy E_p Eq. 3.39 and integrating from R_b to *R*, gives the plastic strain energy of the plate for each burn point R_b.

Eq. 3.41 $$E_{pR}(R_b) = \frac{\pi \cdot H \cdot \sigma_{0R}' \cdot 4 \cdot V_0^2 \cdot t_{fR}^2}{\sqrt{1 - \nu + \nu^2} \cdot \pi^2} \cdot \int_{R_b}^{R} \left(B_R(R_b) + 2 \cdot C_R(R_b) \cdot r + 3 \cdot D_R(R_b) \cdot r^2\right)^2 \cdot r dr$$

Eq. 3.42 $$E_{pR}(R_b) = \frac{\pi \cdot H \cdot \sigma_{0R}'(R_b) \cdot 4 \cdot V_0^2 \cdot t_{fR}(R_b)^2}{\sqrt{(1 - \nu + \nu^2)} \cdot \pi^2} \cdot \alpha_R(R_b)$$

The variable α_R was substituted to simplify Eq. 3.42 and derived by integrating Eq. 3.41, where

Eq. 3.43
$$\begin{aligned}\alpha_R(R_b) = {} & 1/2 \cdot B_R(R_b)^2 \cdot \left(R^2 - R_b{}^2\right) + \\ & 4/3 \cdot B_R(R_b) \cdot C_R(R_b) \cdot \left(R^3 - R_b{}^3\right) + \\ & \left(3/2 \cdot B_R(R_b) \cdot D_R(R_b) + C_R(R_b)^2\right) \cdot \left(R^4 - R_b{}^4\right) + \\ & 12/5 \cdot C_R(R_b) \cdot D_R(R_b) \cdot \left(R^5 - R_b{}^5\right) + \\ & 3/2 \cdot D_R(R_b)^2 \cdot \left(R^6 - R_b{}^6\right)\end{aligned}$$

Substituting the velocity field $\dot{W}_R$ Eq. 3.19, when $t = 0$, into the kinetic energy E_k Eq. 3.40, and integrating from R_b to R, gives the initial kinetic energy E_k for each burn point.

Eq. 3.44
$$E_{kR}(R_b) = \pi \cdot \rho \cdot H \cdot V_0{}^2 \cdot \int_{R_b}^{R} \left(A_R(R_b) + B_R(R_b) \cdot r + C_R(R_b) \cdot r^2 + D_R(R_b) \cdot r^3\right)^2 \cdot r dr$$

Eq. 3.45
$$E_{kR}(R_b) = \pi \cdot \rho \cdot H \cdot V_0{}^2 \cdot \beta_R(R_b)$$

The variable β_R was substituted to simplify Eq. 3.45 and derived by integrating Eq. 3.44, where

Eq. 3.46
$$\begin{aligned}\beta_R(R_b) = {} & 1/2 \cdot A_R(R_b)^2 \cdot \left(R^2 - R_b{}^2\right) + 2/3 \cdot A_R(R_b) \cdot B_R(R_b) \cdot \left(R^3 - R_b{}^3\right) + \\ & \left(1/2 \cdot A_R(R_b) \cdot C_R(R_b) + 1/4 \cdot B_R(R_b)^2\right) \cdot \left(R^4 - R_b{}^4\right) + \\ & \left(2/5 \cdot A_R(R_b) \cdot D_R(R_b) + 2/5 \cdot B_R(R_b) \cdot C_R(R_b)\right) \cdot \left(R^5 - R_b{}^5\right) + \\ & \left(1/3 \cdot B_R(R_b) \cdot D_R(R_b) + 1/6 \cdot C_R(R_b)^2\right) \cdot \left(R^6 - R_b{}^6\right) + \\ & 2/7 \cdot C_R(R_b) \cdot D_R(R_b) \cdot \left(R^7 - R_b{}^7\right) + \\ & 1/8 \cdot D_R(R_b)^2 \cdot \left(R^8 - R_b{}^8\right)\end{aligned}$$

To find the response time t_{fR}, Eq. 3.42 and Eq. 3.45 are equated and hence

Eq. 3.47 $$t_{fR}(R_b) = \sqrt{\frac{\rho}{\sigma_{0R}'(R_b)}} \cdot \frac{(1-\nu+\nu^2)^{\frac{1}{4}} \cdot \pi}{2} \cdot \sqrt{\frac{\beta_R(R_b)}{\alpha_R(R_b)}}$$

For W_L and $\dot{W}_L$

Since W_{RL}, W_L and $\dot{W}_{RL}$, $\dot{W}_L$ are axisymmetric about the centre of the plate, E_k will be the same for $\dot{W}_L$ and $\dot{W}_{RL}$, and E_p will be the same for W_L and W_{RL} for each burn point. This means t_{fL} and t_{fRL} will have the same value for each burn point.

Differentiating the displacement field W_L Eq. 3.36, when $t = t_{fL}$, with respect to r, substituting into the plastic energy E_p Eq. 3.39, and integrating from R_b to $-R$, gives the plastic strain energy of the plate for each burn point.

Eq. 3.48 $$E_{pL}(R_b) = \frac{\pi \cdot H \cdot \sigma_{0L}' \cdot 4 \cdot V_0^2 \cdot t_{fL}^2}{\sqrt{(1-\nu+\nu^2)} \cdot \pi^2} \cdot \left(\int_0^{R_b} \left(B_L(R_b) + 2 \cdot C_L(R_b) \cdot r + 3 \cdot D_L(R_b) \cdot r^2 \right)^2 \cdot r dr + \int_0^{-R} \left(B_L(R_b) + 2 \cdot C_L(R_b) \cdot r + 3 \cdot D_L(R_b) \cdot r^2 \right)^2 \cdot r dr \right)$$

Eq. 3.49 $$E_{pL}(R_b) = \frac{\pi \cdot H \cdot \sigma_{0L}'(R_b) \cdot 4 \cdot V_0^2 \cdot t_{fL}(R_b)^2}{\sqrt{(1-\nu+\nu^2)} \cdot \pi^2} \cdot \alpha_L(R_b)$$

The variable α_L was substituted to simplify Eq. 3.49 and derived by integrating Eq. 3.48, where

Eq. 3.50
$$\begin{aligned}\alpha_L(R_b) = {} & 1/2 \cdot B_L(R_b)^2 \cdot \left(R^2 + R_b{}^2\right) + \\ & 4/3 \cdot B_L(R_b) \cdot C_L(R_b) \cdot \left(-R^3 + R_b{}^3\right) + \\ & \left(3/2 \cdot B_L(R_b) \cdot D_L(R_b) + C_L(R_b)^2\right) \cdot \left(R^4 + R_b{}^4\right) + \\ & 12/5 \cdot C_L(R_b) \cdot D_L(R_b) \cdot \left(-R^5 + R_b{}^5\right) + \\ & 3/2 \cdot D_L(R_b)^2 \cdot \left(R^6 + R_b{}^6\right)\end{aligned}$$

Substituting the velocity field $\dot{W}_L$ Eq. 3.20 into the kinetic energy E_k Eq. 3.40, letting $t = 0$, and integrating from R_b to -R, gives the initial kinetic energy of the plate for each burn point.

Eq. 3.51
$$\begin{aligned}E_{kL}(R_b) = {} & \pi \cdot \rho \cdot H \cdot V_0^2 \cdot \\ & \left(\int_0^{R_b} \left(A_L(R_b) + B_L(R_b) \cdot r + C_L(R_b) \cdot r^2 + D_L(R_b) \cdot r^3\right)^2 \cdot r dr + \right. \\ & \left. \int_0^{-R} \left(A_L(R_b) + B_L(R_b) \cdot r + C_L(R_b) \cdot r^2 + D_L(R_b) \cdot r^3\right)^2 \cdot r dr\right)\end{aligned}$$

Eq. 3.52
$$E_{kL}(R_b) = \pi \cdot \rho \cdot H \cdot V_0^2 \cdot \beta_L(R_b)$$

The variable β_L was substituted to simplify Eq. 3.52 and derived by integrating Eq. 3.51, where

Eq. 3.53
$$\begin{aligned}\beta_L(R_b) = {} & 1/2 \cdot A_L(R_b)^2 \cdot \left(R^2 + R_b{}^2\right) + 2/3 \cdot A_L(R_b) \cdot B_L(R_b) \cdot \left(-R^3 + R_b{}^3\right) + \\ & \left(1/2 \cdot A_L(R_b) \cdot C_L(R_b) + 1/4 \cdot B_L(R_b)^2\right) \cdot \left(R^4 + R_b{}^4\right) + \\ & \left(2/5 \cdot A_L(R_b) \cdot D_L(R_b) + 2/5 \cdot B_L(R_b) \cdot C_L(R_b)\right) \cdot \left(-R^5 + R_b{}^5\right) + \\ & \left(1/3 \cdot B_L(R_b) \cdot D_L(R_b) + 1/6 \cdot C_L(R_b)^2\right) \cdot \left(R^6 + R_b{}^6\right) + \\ & 2/7 \cdot C_L(R_b) \cdot D_L(R_b) \cdot \left(-R^7 + R_b{}^7\right) + \\ & 1/8 \cdot D_L(R_b)^2 \cdot \left(R^8 + R_b{}^8\right)\end{aligned}$$

To find the response time t_{fL} Eq. 3.49 and Eq. 3.52 are equated giving

Eq. 3.54 $$t_{fL}(R_b) = \sqrt{\frac{\rho}{\sigma_0{}'_L(R_b)}} \cdot \frac{\left(1-\nu+\nu^2\right)^{\frac{1}{4}} \cdot \pi}{2} \cdot \sqrt{\frac{\beta_L(R_b)}{\alpha_L(R_b)}}$$

3.1.2 DYNAMIC YIELD STRESS

To calculate the response times t_f, the dynamic yield stresses $\sigma_0{}'$ for each displacement and corresponding velocity field for each burn point are determined. These dynamic yield stresses are found by calculating the average strain rate for each displacement and corresponding velocity field for each burn point, and substituting these into the Cowper-Symonds relationship. The strain rates are averaged over both time and radius.

The Cowper-Symonds relationship is [5].

Eq. 3.55 $$\sigma_0{}'(R_b) = \sigma_0 \cdot \left(1+\left(\frac{\dot{\varepsilon}_{ave}(R_b)}{\dot{\varepsilon}_0}\right)^{\frac{1}{n}}\right)$$

Radial middle surface strain rate can be written as [5].

Eq. 3.56 $$\dot{\varepsilon}_r(r,t,R_b) = \frac{\partial W(r,t,R_b)}{\partial r} \cdot \frac{\partial \dot{W}(r,t,R_b)}{\partial r}$$

Using Eq. 3.56, the strain rates are found for each displacement and corresponding velocity field for each burn point.

For W_R and $\dot{W}_R$

Differentiating both the displacement field W_R Eq. 3.34 and the velocity field $\dot{W}_R$ Eq. 3.19 with respect to r and substituting into the strain rate Eq. 3.56, gives the strain rate for each burn point.

Eq. 3.57
$$\dot{\varepsilon}_{rR}(r,t,R_b)=\frac{2\cdot V_0^{\,2}\cdot t_{fR}(R_b)\cdot\sin\left(\frac{\pi}{2\cdot t_{fR}(R_b)}\cdot t\right)\cdot\cos\left(\frac{\pi}{2\cdot t_{fR}(R_b)}\cdot t\right)}{\pi}\cdot\frac{\pi}{\left(B_R(R_b)+2\cdot C_R(R_b)\cdot r+3\cdot D_R(R_b)\cdot r^2\right)^2}$$

Averaging Eq. 3.57 from time $t=0$ to $t=t_{fR}$ and over the radius from $r=R$ to $r=R_b$, gives the average strain rate for each burn point as

Eq. 3.58
$$\dot{\varepsilon}_{aveR}(R_b)=\frac{2\cdot V_0^{\,2}\cdot t_{fR}(R_b)}{\pi^2\cdot(R-R_b)}\cdot\chi_R(R_b)$$

The variable χ_R was substituted to simplify Eq. 3.58 and was derived by averaging Eq. 3.57, where

Eq. 3.59
$$\begin{aligned}\chi_R(R_b)=&B_R(R_b)^2\cdot(R-R_b)+2\cdot B_R(R_b)\cdot C_R(R_b)\cdot\left(R^2-R_b^{\,2}\right)+\\&\left(2\cdot B_R(R_b)\cdot D_R(R_b)+4/3\cdot C_R(R_b)^2\right)\cdot\left(R^3-R_b^{\,3}\right)+\\&3\cdot C_R(R_b)\cdot D_R(R_b)\cdot\left(R^4-R_b^{\,4}\right)+9/5\cdot D_R(R_b)^2\cdot\left(R^5-R_b^{\,5}\right)\end{aligned}$$

By substituting the response time t_{fR} Eq. 3.47, into Eq. 3.58, the strain rate is now in a form that can be substituted into the Cowper-Symonds equation, i.e.

Eq. 3.60 $$\dot{\varepsilon}_{aveR}(R_b)=\frac{2\cdot V_0^{\,2}}{\pi^2\cdot(R-R_b)}\sqrt{\frac{\rho}{\sigma_{0R}{}'(R_b)}}\cdot\frac{\left(1-\nu+\nu^2\right)^{\frac{1}{4}}\cdot\pi}{2}\cdot\sqrt{\frac{\beta_R(R_b)}{\alpha_R(R_b)}}\cdot\chi_R(R_b)$$

Eq. 3.60 substituted into Eq. 3.55 and using an iterative solution scheme $\sigma_{0R}{}'$ is calculated for each burn point. $\sigma_{0R}{}'$ is substituted into Eq. 3.47 to give the response time t_{fR} for each burn point.

For W_L and $\dot{W}_L$

Differentiating both the displacement field W_L Eq. 3.36 and the velocity field $\dot{W}_L$ Eq 3.20 with respect to r and substituting into Eq. 3.56, gives the strain rate for each burn point.

Eq. 3.61 $$\dot{\varepsilon}_{rL}(r,t,R_b)=\frac{2\cdot V_0^{\,2}\cdot t_{fL}(R_b)\cdot\sin\left(\frac{\pi}{2\cdot t_{fL}(R_b)}\cdot t\right)\cdot\cos\left(\frac{\pi}{2\cdot t_{fL}(R_b)}\cdot t\right)}{\pi\left(B_L(R_b)+2\cdot C_L(R_b)\cdot r+3\cdot D_L(R_b)\cdot r^2\right)^2}.$$

Averaging Eq. 3.61 over time $t=0$ to $t=t_{fL}$, and over the radius from $r=-R$ to $r=R_b$, the average strain rate for each burn point is obtained.

Eq. 3.62 $$\dot{\varepsilon}_{aveL}(R_b)=\frac{2\cdot V_0^{\,2}\cdot t_{fL}(R_b)}{\pi^2\cdot(R-R_b)}\cdot\chi_L(R_b)$$

The variable χ_L was substituted to simplify Eq. 3.62 and was derived by averaging Eq. 3.61, where

Eq. 3.63
$$\chi_L(R_b) = B_L(R_b)^2 \cdot (R + R_b) + 2 \cdot B_L(R_b) \cdot C_L(R_b) \cdot \left(-R^2 + R_b^2\right) + \left(2 \cdot B_L(R_b) \cdot D_L(R_b) + 4/3 \cdot C_L(R_b)^2\right) \cdot \left(R^3 + R_b^3\right) + 3 \cdot C_L(R_b) \cdot D_L(R_b) \cdot \left(-R^4 + R_b^4\right) + 9/5 \cdot D_L(R_b)^2 \cdot \left(R^5 + R_b^5\right)$$

By substituting the response time t_{fL} Eq. 3.54 into Eq. 3.62, the strain rate for each burn point can now be used in the Cowper-Symonds equation, i.e.

Eq. 3.64
$$\dot{\varepsilon}_{aveL}(R_b) = \frac{2 \cdot V_0^2}{\pi^2 \cdot (R + R_b)} \sqrt{\frac{\rho}{\sigma_{0L}'(R_b)}} \cdot \frac{\left(1 - \nu + \nu^2\right)^{\frac{1}{4}} \cdot \pi}{2} \cdot \sqrt{\frac{\beta_L(R_b)}{\alpha_L(R_b)}} \cdot \chi_L(R_b)$$

Eq. 3.64 substituted into Eq. 3.55, and using an iterative solution scheme σ_{0L}' is calculated for each burn point. σ_{0L}' is then substituted into Eq. 3.54 to give the response time t_{fL} for each burn point.

3.1.3 TOTAL DISPLACEMENTS

The total displacements give the final plate shape and are found by summing the maximum deflections of the displacement fields, i.e. when $t = t_f$, at each discretised point. Due to axisymmetry, only the total displacements over the right hand side of the plate are required. Displacement fields at maximum deflection are called the final displacement fields and are given as,

Eq. 3.65 $$W_R(r, R_b) = \frac{2 \cdot V_0 \cdot t_{fR}(R_b)}{\pi} \cdot \phi_R(r, R_b)$$

Eq. 3.66 $$W_L(r, R_b) = \frac{2 \cdot V_0 \cdot t_{fL}(R_b)}{\pi} \cdot \phi_L(r, R_b)$$

Eq. 3.67 $$W_{RL}(r, R_b) = \frac{2 \cdot V_0 \cdot t_{fL}(R_b)}{\pi} \cdot \phi_{RL}(r, R_b)$$

The displacements of the final displacement fields W_R and W_L, at $r = 0$, are continuous when the burn point is at the centre of the plate, as shown in Figure 3.12. However, it is noted that the fields W_R and W_L have different response times t_{fR} and t_{fL} for all other burn points. Thus the final displacement fields W_R and W_L, at $r = R_b$, are discontinuous, as illustrated in Figure 3.13, Figure 3.14 and Figure 3.15. This discontinuity is partially smoothed out by taking an average between W_R and W_L, at $r = R_b$, for each burn point.

Calculation of the total displacements requires that the plate be divided into four regions with each region having a governing equation. The four regions are $r = 0$, $0 > r > R_0$, $r = R_0$ and $R_0 < r \le R$. The equations for the four regions are given as,

Total Displacement For $r = 0$

Eq. 3.68
$$W_T(r) = \sum_{R_b=r}^{R_b=r} \frac{\left(W_L(r,R_b) + W_{RL}(r,R_b)\right) + \left(W_R(r,R_b) + W_{RL}(r,R_b)\right)}{2} + \sum_{R_b=R_0}^{R_b>r} \left(W_L(r,R_b) + W_{RL}(r,R_b)\right)$$

Total Displacement For $0 < r < R_0$

Eq. 3.69
$$W_T(r) = \sum_{R_b<r}^{R_b=0} \left(W_R(r,R_b) + W_{RL}(r,R_b)\right) + \sum_{R_b=r}^{R_b=r} \frac{\left(W_L(r,R_b) + W_{RL}(r,R_b)\right) + \left(W_R(r,R_b) + W_{RL}(r,R_b)\right)}{2} + \sum_{R_b=R_0}^{R_b>r} \left(W_L(r,R_b) + W_{RL}(r,R_b)\right)$$

Total Displacement For $r = R_0$

Eq. 3.70
$$W_T(r) = \sum_{R_b<r}^{R_b=0} \left(W_R(r,R_b) + W_{RL}(r,R_b)\right) + \sum_{R_b=r}^{R_b=r} \frac{\left(W_L(r,R_b) + W_{RL}(r,R_b)\right) + \left(W_R(r,R_b) + W_{RL}(r,R_b)\right)}{2}$$

Total Displacement For $R_0 < r \le R$

Eq. 3.71
$$W_T(r) = \sum_{R_b=R_0}^{R_b=0} \left(W_R(r,R_b) + W_{RL}(r,R_b)\right)$$

The manner in which the total displacement is calculated at each discretised point is illustrated in Figure 3.12, Figure 3.13, Figure 3.14 and Figure 3.15. In the illustrations, the plate is discretised into six points (*0,r1, r2,* R_0, *r3* and *R*) four of which are burn points (*0,r1, r2* and R_0). These four burn points result in four of each of the final displacement fields W_R, W_L and W_{RL}.

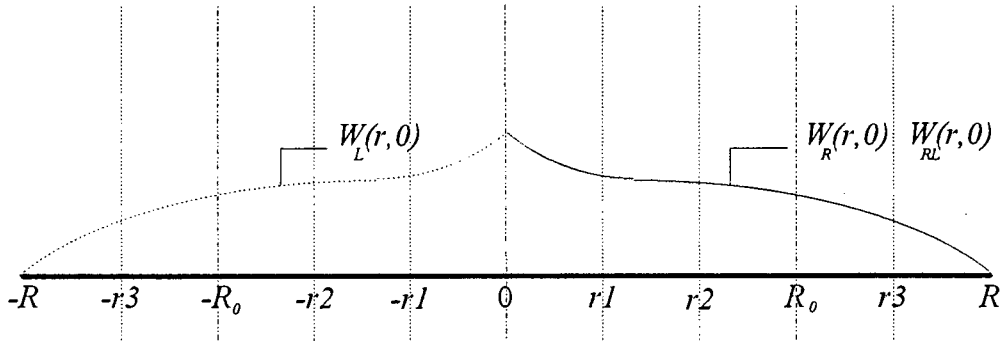

Figure 3.12 Cubic displacement fields W_R, W_L and W_{RL} when $t = t_f$ and $R_b = 0$.

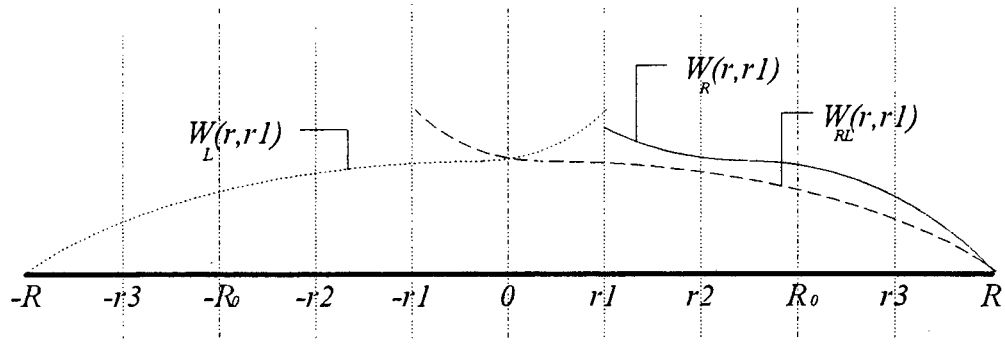

Figure 3.13 Cubic displacement fields W_R, W_L and W_{RL} when $t = t_f$ and $R_b = r1$.

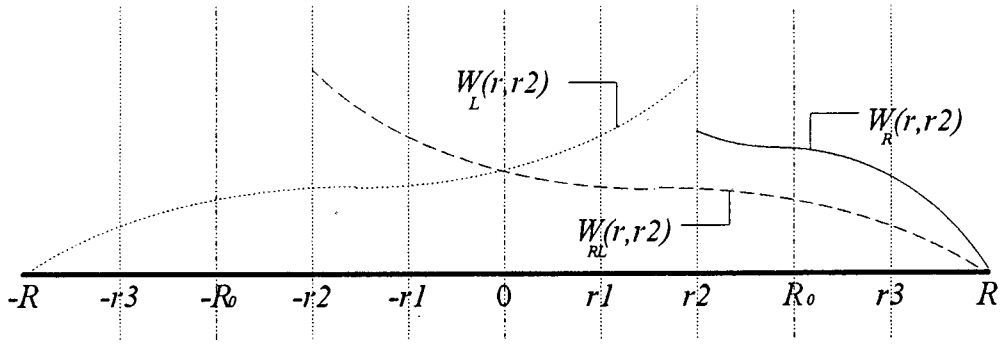

Figure 3.14 Cubic displacement fields W_R, W_L and W_{RL} when $t = t_f$ and $R_b = r2$.

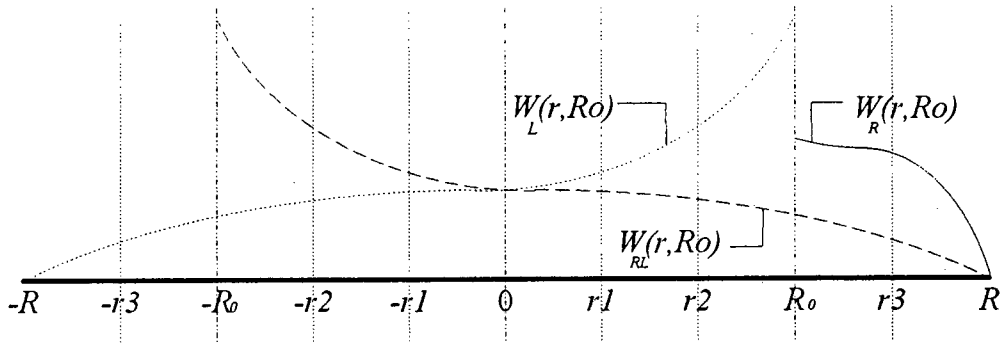

Figure 3.15 Cubic displacement fields W_R, W_L and W_{RL} when $t = t_f$ and $R_b = R_0$.

An example calculating the total displacement using Eq. 3.68 to Eq. 3.71 with reference to Figure 3.12, Figure 3.13, Figure 3.14 and Figure 3.15 is given in Appendix B.

3.1.4 SOLUTION SCHEME

Using the analysis in the previous sections a solution scheme to find the total displacement of a circular plate subjected to a central blast load is given in Figure 3.16.

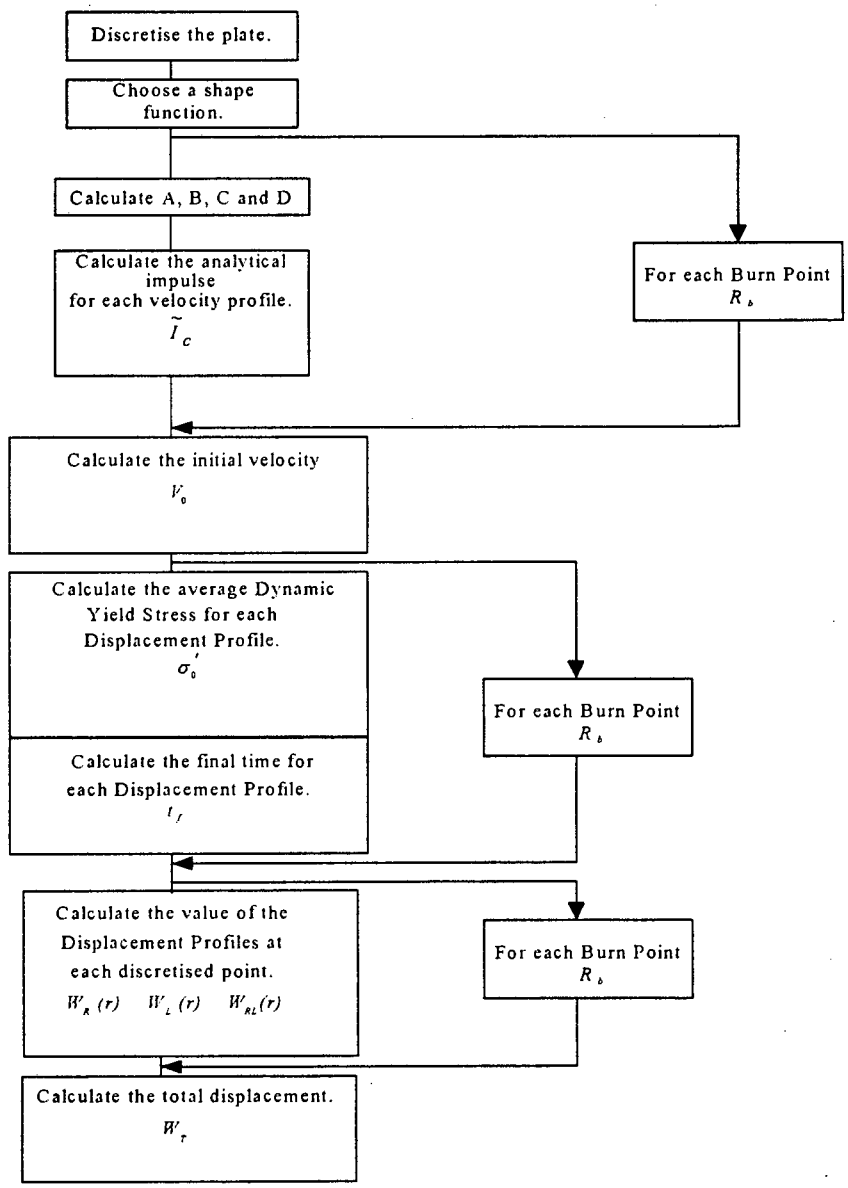

Figure 3.16 Plate displacement solution scheme.

3.2 THEORETICAL STRAIN MODEL

The strain in the deformed plates is assumed to be radial and uniform throughout the thickness, with no bending effects being taken into account. From the observations made on the deformed plates, failure of the plates occurred through a cap blowing out of the centre of the plate. This failure was observed to be due to tensile tearing and as an approximation the plate failure criterion is taken to be quasistatic uniaxial tensile strain at failure. This data is available from uniaxial tensile tests done on the plate material.

From the total displacement W_T, the strain distribution through the plate can be found, and is calculated from the change in length between two consecutive discretised points in the deformed and undeformed plate. Thus an average strain between two consecutive discretised points is determined and is assumed to occur mid-way between these two points.

3.2.1 EQUATION FORMULATION

Strain is defined as follows

Eq. 3.72 $$\varepsilon = \frac{\Delta l}{l}$$

where Δl is the change between the deformed and undeformed length l as shown in Figure 3.17. l and Δl, between two consecutive discretised points (r_1 and r_2 with $r_2 \geq r_1$), can be defined in terms of the deformed and undeformed plate as

Eq. 3.73 $$l = r_2 - r_1$$

Eq. 3.74 $$\Delta l = \left(l^2 + \left(W_T(r_2) - W_T(r_1) \right)^2 \right)^{1/2} - l$$

where W_T is the total displacement.

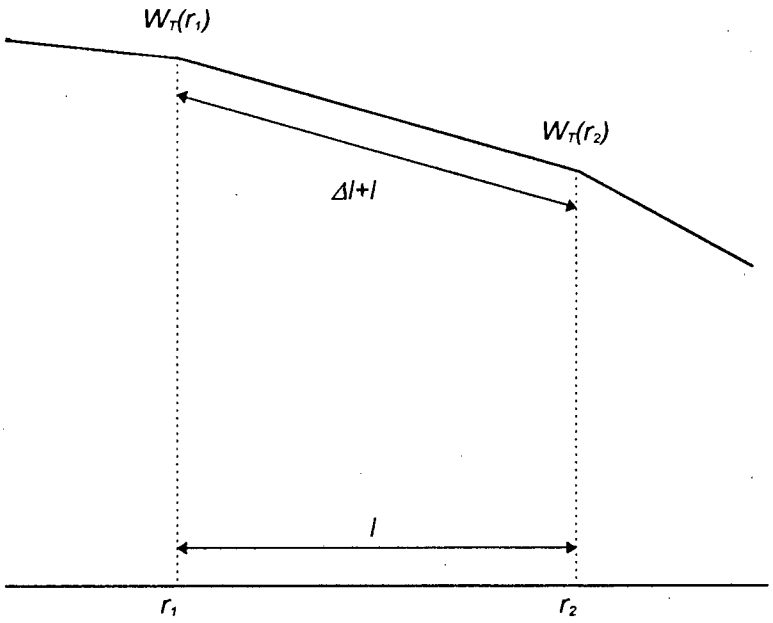

Figure 3.17 Undeformed plate length l and deformed plate length $\Delta l + l$ between two consecutive discretised points r_1 and r_2.

Substituting Eq. 3.73 and Eq. 3.74 into Eq. 3.72 gives the average strain between two consecutive discretised points r_1 and r_2. The average strain is assumed to occur at a point r_{ave} mid-way between r_1 and r_2 as defined below.

Eq. 3.75 $$r_{ave} = r_1 + \frac{r_2 - r_1}{2}$$

4. EXPERIMENTATION

The experimentation reported on in this document was done by the author as an undergraduate project and was carried out with the aim of investigating the effect of a centralised blast load on thin metal plates. The following sections give the experimental procedures, materials tested, explosive material used, the observations that were made and results obtained from the experimentation. Other data used in this investigation was generated by Bodner and Symonds [4]. The test plate geometry and localised load to plate diameter ratios used by Bodner and Symonds were, plate radius 31.75mm, plate thickness 1.93mm and load to plate diameter ratios of 1/2 and 1/3.

4.1 EXPERIMENTAL PROCEDURE

The experimental procedure used is similar to that used by Bodner and Symonds [4], Teeling-Smith and Nurick [8] and Thomas [9], and is described as follows:

4.1.1 BALLISTIC PENDULUM

A ballistic pendulum was used to measure the impulse applied to the plates. It consists of a steel I beam suspended from a solid concrete roof by four spring steel wires, as can be seen in Figure 4.1. The spring steel wires have adjustable screws attached to them, enabling the pendulum to be levelled. At either end of the pendulum the plate clamping frame and balancing masses are attached. The balancing masses are used to balance the pendulum to ensure that the spring steel wires carry approximately the same weight thus ensuring that the impulse acts through the centroid of the pendulum. Also attached to the ballistic pendulum is a recorder pen. This pen is used to record the oscillation amplitude of the pendulum onto a sheet of tracing paper. The oscillation amplitude relates directly to the impulse imparted onto the test specimen.

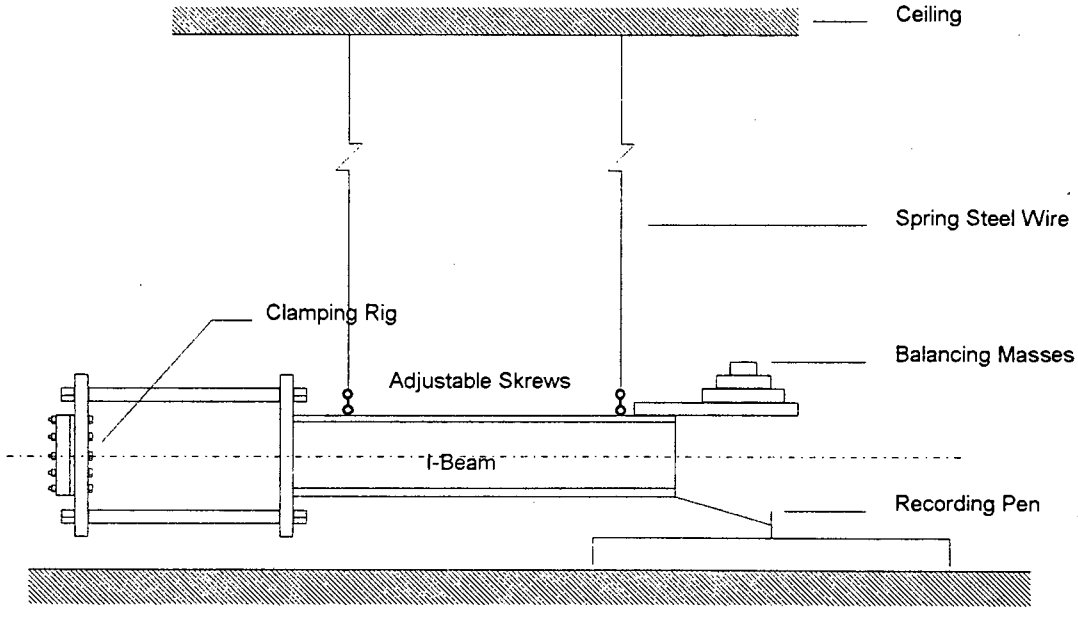

Figure 4.1 Ballistic pendulum.

The clamping rig consists of two thick steel plates, each having 100mm diameter holes drilled in them. The thick plates clamp the test specimen between them by means of 8 high tensile steel bolts. This is illustrated in Figure 4.2. The clamping force applied to the test plates was assumed to be sufficient to prevent slippage of the plates at the boundary and no visible evidence was noted.

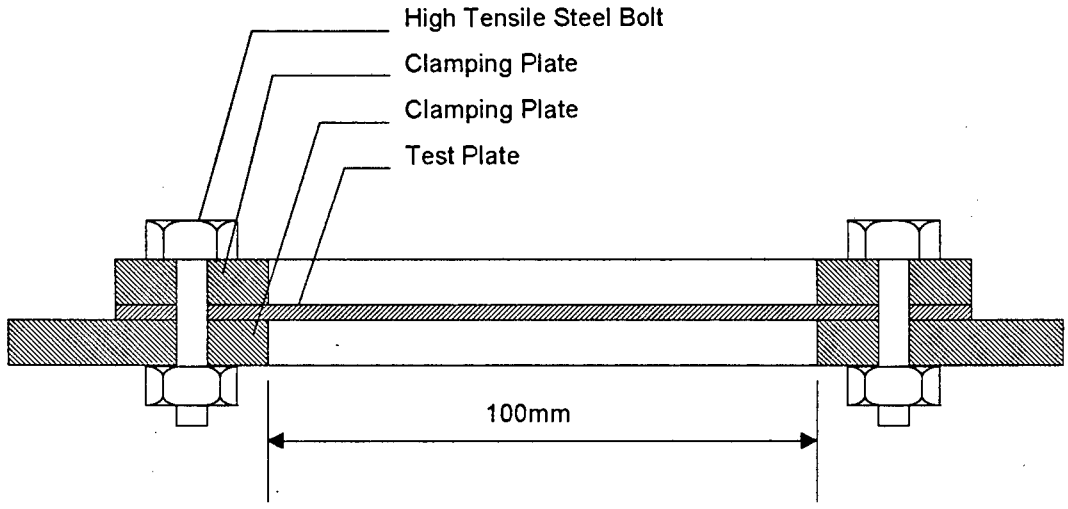

Figure 4.2 Clamping rig.

The equations relating the motion of the pendulum to the impulse applied to the test plates are given Appendix C.

Table 4.1 gives the ballistic pendulum constants used during the experiments.

Mass of I-Beam	28155g
Mass of Clamping Rig	11525g
Mass of Counter Balance	23751g
TOTAL PENDULUM MASS (M)	63431g
R	2565mm
Z	183.5mm
a	62.5mm
T	3.19 s

Table 4.1 Ballistic pendulum details.

4.1.2 EXPLOSIVE LOAD GEOMETRY AND MATERIAL PROPERTIES

The plates were centrally loaded using a plastic explosive (PE 4), with an approximate burn speed of 7500 m/s. This explosive was spread evenly onto a polystyrene foam pad over the load diameters 18.3mm, 25mm, 33mm and 40mm with a detonator in the centre. Differing masses of explosive were used giving different impulses, resulting in plate deformations from approximately two deformation thickness up to the onset of and including plate tearing. The foam pads had a diameter equal to the plate diameter 100mm and an approximate thickness of 12mm, and disintegrated on detonation. The load configuration is illustrated in Figure 4.3.

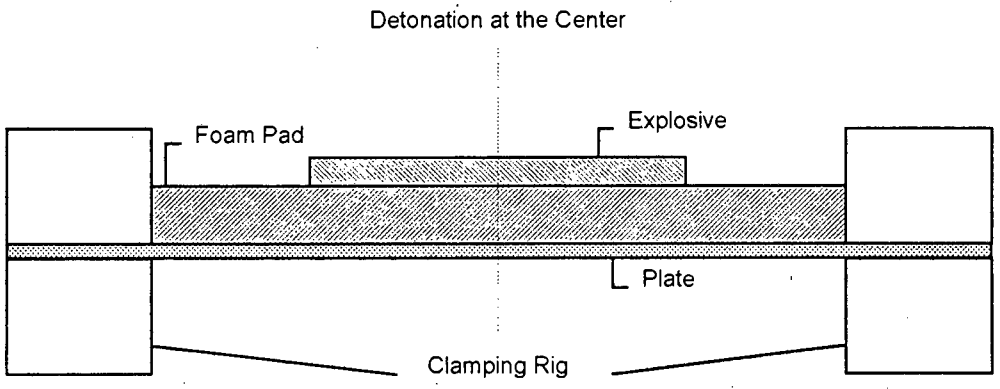

Figure 4.3 Load configuration.

4.1.3 TEST PLATE GEOMETRY AND MATERIAL PROPERTIES

The test plates were made from hot rolled mild steel and had an outer diameter of 100mm and thickness of 1.6mm. The material properties and plate geometry are given in Table 4.2.

Radius (R)	100mm
Thickness (t)	1.6mm
Density (ρ)	7850 Kg/m^3
$\dot{\varepsilon}_0$	40.4 sec^{-1}
n	5
Possion's Ratio (ν)	0.33
Uniaxial Tensile Stress	193.5 MPa
Young's Modulus (E)	210 GPa
% Uniaxial Tensile Strain at Failure	32.5

Table 4.2 Plate material properties and geometry.

The uniaxial tensile stress and strain at failure for the plate material was measured using standard tensile test specimens extended at a constant cross-head speed until failure occurred. Several specimens were tested at different cross-head speeds varying from 0.025 mm/min up to 508.3 mm/min and the dynamic uniaxial tensile stresses σ_0' and strains at failure for each specimen were measured. Using the dynamic uniaxial tensile stress, the quasistatic uniaxial tensile stress σ_0 was

determined using the Cowper-Symonds relationship (Eq. 4.1). The results are shown in Appendix D.

Eq. 4.1 $$\frac{\sigma_0'}{\sigma_0} = 1 + \left(\frac{\dot{\varepsilon}}{\dot{\varepsilon}_0}\right)^{\frac{1}{n}}$$

Where $\dot{\varepsilon}$ is the strain rate and $\dot{\varepsilon}_0$ and n are constants given in Table 4.2.

4.2 EXPERIMENTAL OBSERVATIONS

The following observations were made concerning the general overall deformation and necking of the plates.

4.2.1 GENERAL PLATE DEFORMATION

The plate deflections were not uniform due to the formation of a nipple at the centre of the plate, with the nipple size being proportional to the load diameter. This plate deformation increased with an increasing impulse up to a point were a cap blew out of the centre of the plate, likewise the cap size was proportional to the load diameter. These observations can be seen in the general views of the plates given in Figure 4.4 to Figure 4.7 and a side view of the plates cut through the centre in Figure 4.8 to Figure 4.11.

In each of the general views Figure 4.4, Figure 4.5, Figure 4.6 and Figure 4.7 the top right hand plate has had a cap blown out which is placed next to the plate, except for the 40mm load diameter where the cap is still attached. Similarly in the side views, Figure 4.8, Figure 4.9, Figure 4.10 and Figure 4.11, the top plate has had a cap blown out again with the exception of the 40mm load diameter were the cap is still attached.

4.2.1.1 GENERAL VIEW OF DEFORMED PLATES

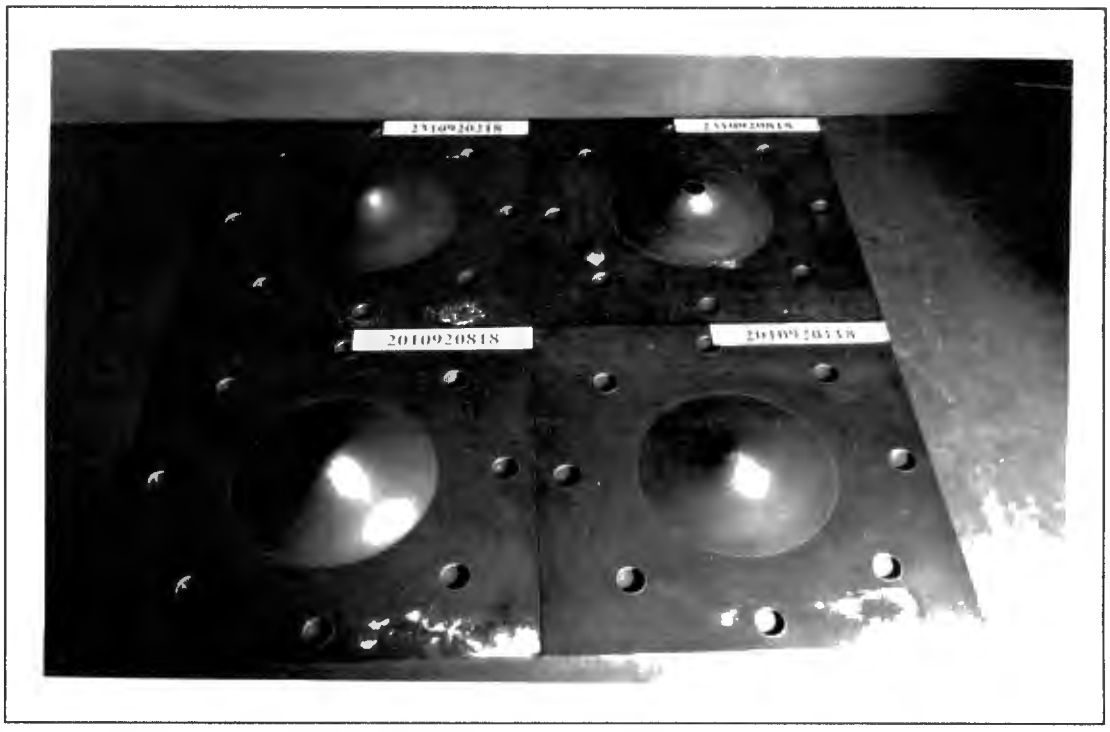

Figure 4.4 Deformed plates with a load diameter of 18.3mm.

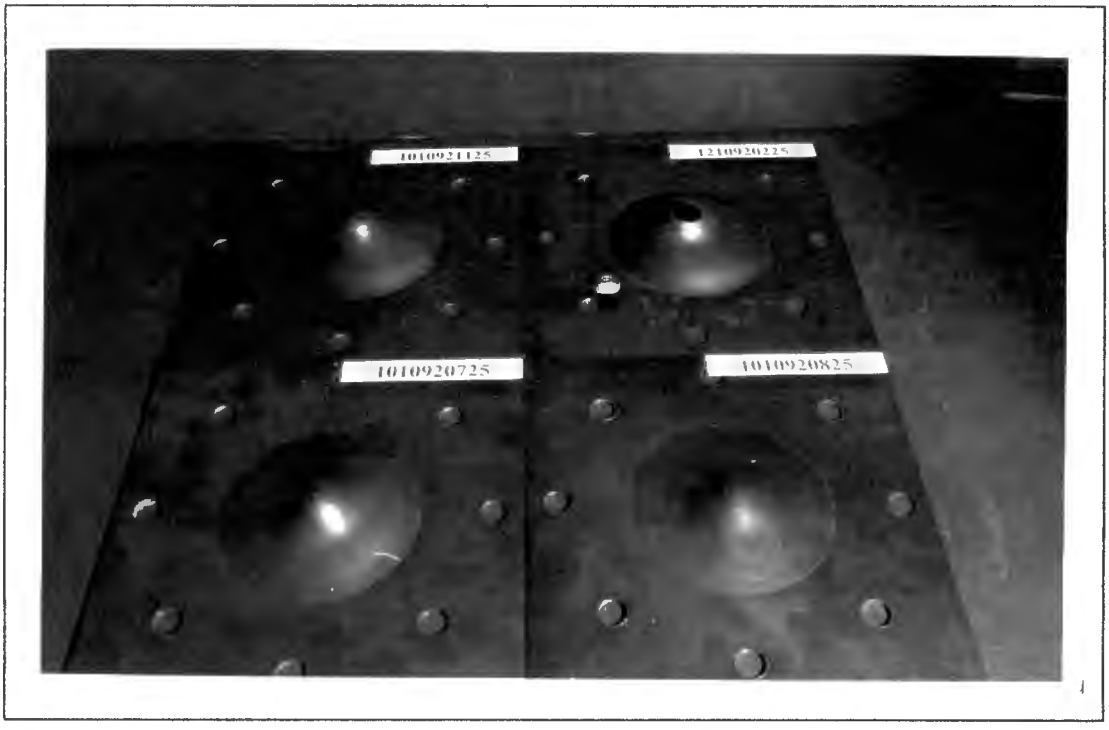

Figure 4.5 Deformed plates with a load diameter of 25mm.

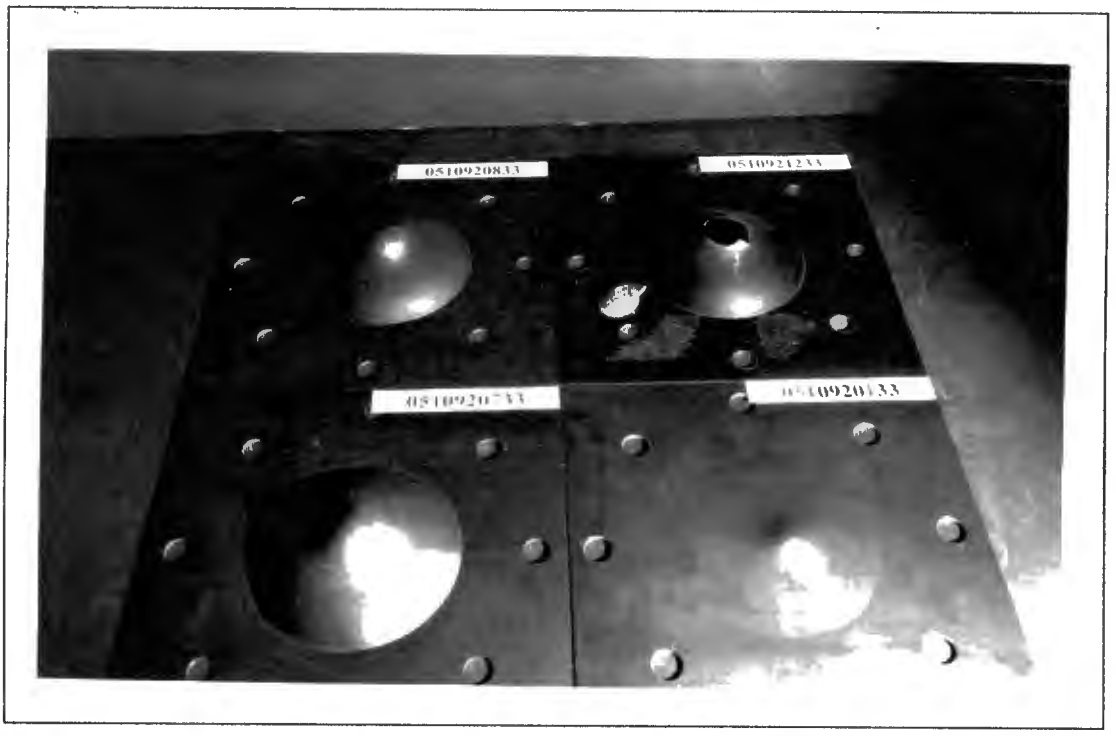

Figure 4.6 Deformed plates with a load diameter of 33mm.

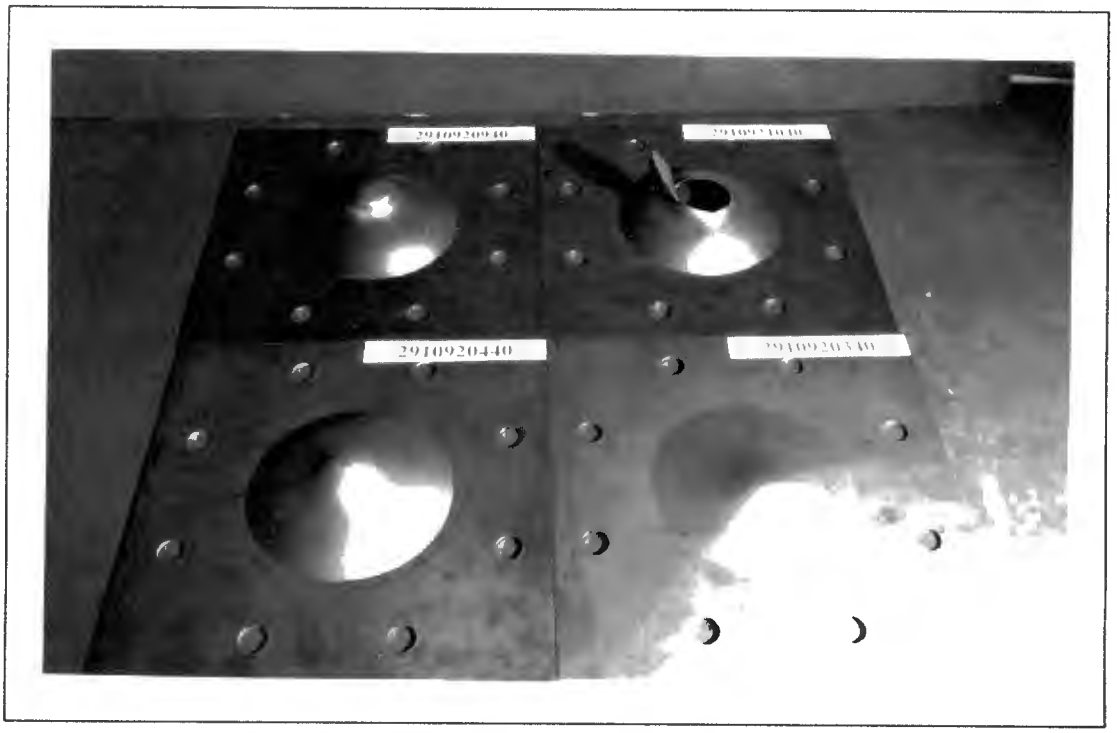

Figure 4.7 Deformed plates with a load diameter of 40mm.

4.2.1.2 SIDE VIEW OF DEFORMED PLATES CUT THROUGH THE CENTRE

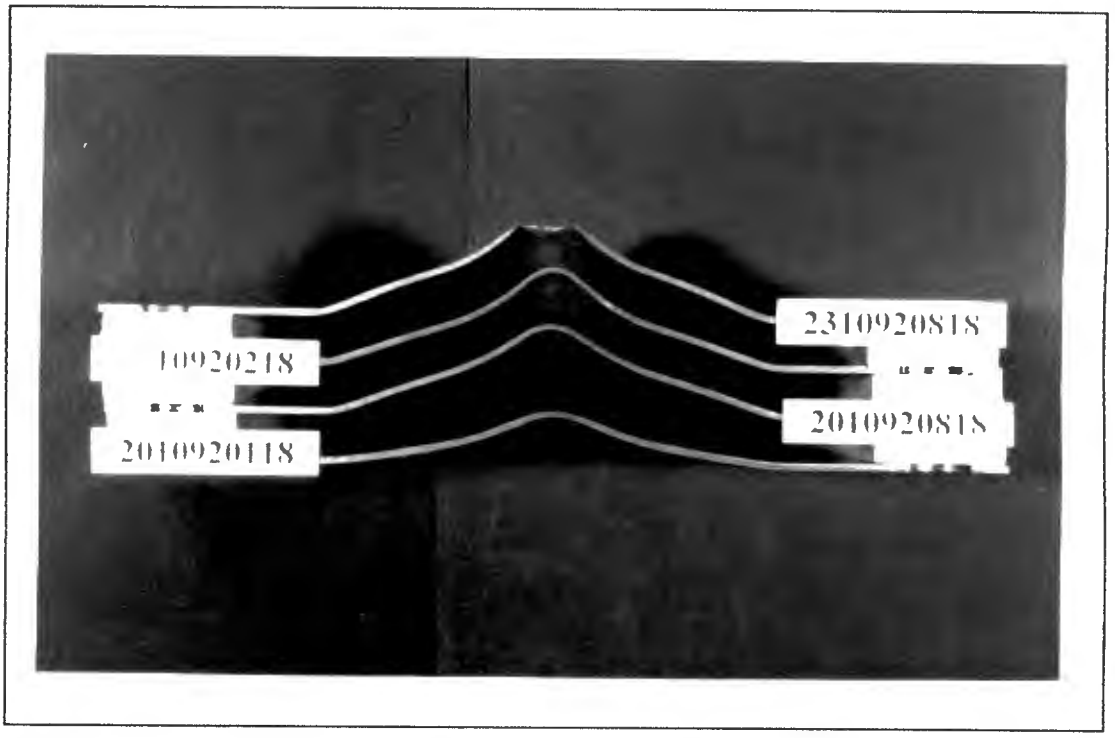

Figure 4.8 Side view of cut plates with a load diameter of 18.3mm.

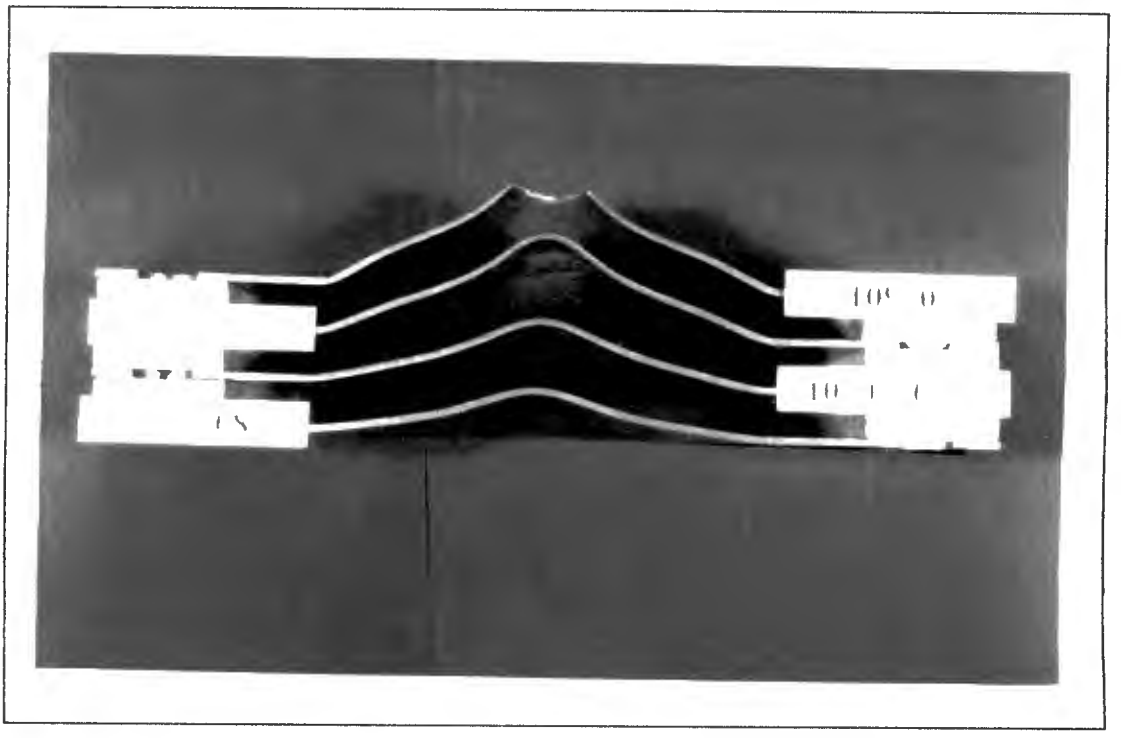

Figure 4.9 Side view of cut plates with a load diameter of 25mm.

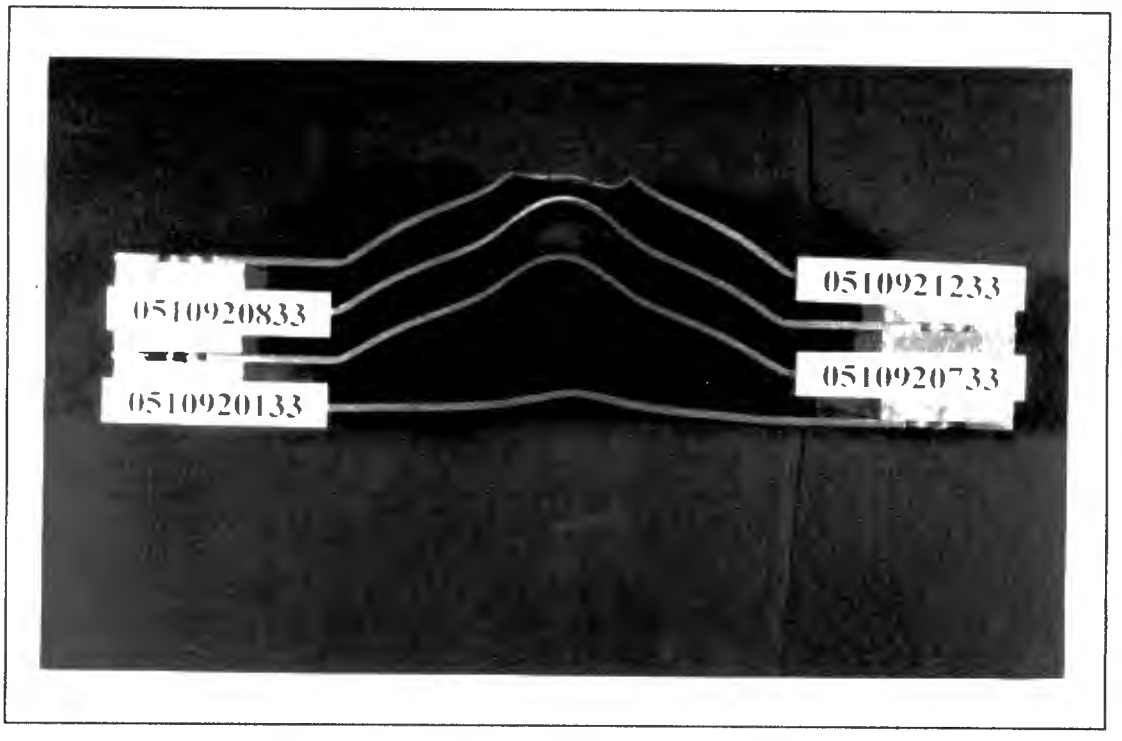

Figure 4.10 Side view of cut plates with a load diameter of 33mm.

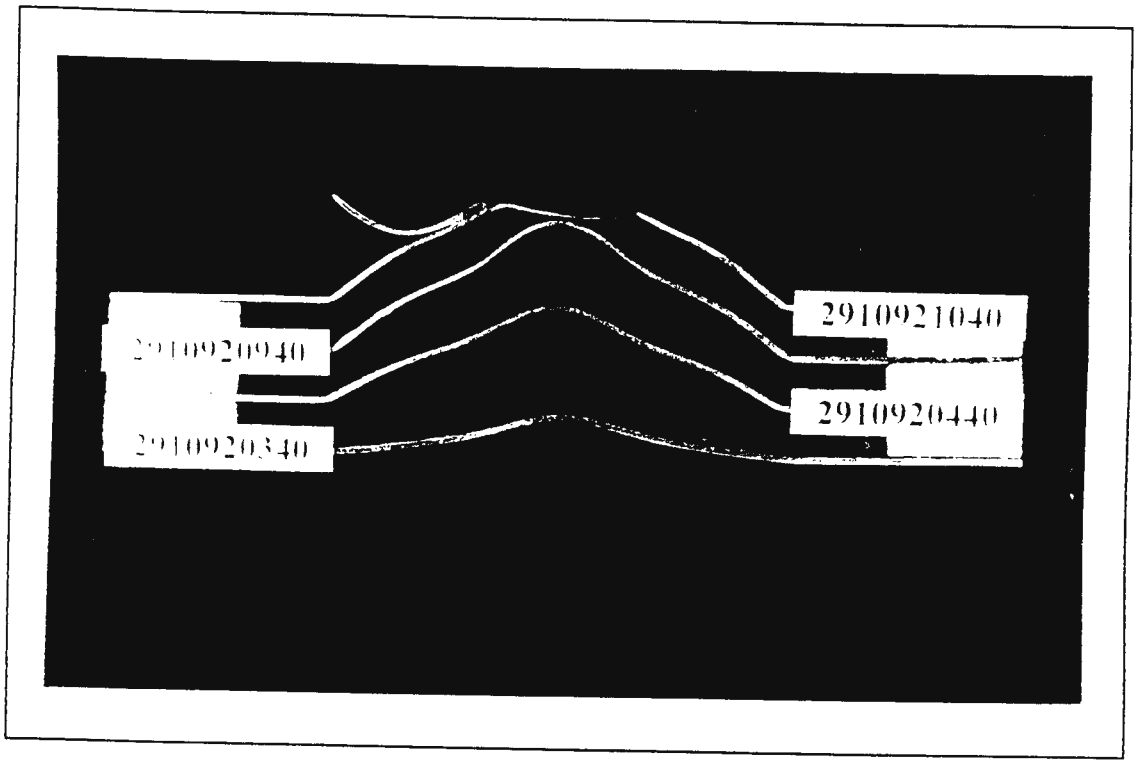

Figure 4.11 Side view of cut plates with a load diameter of 40mm.

4.2.2 PLATE NECKING

For the higher impulses it was noted that necking began to take place around the nipple for all the load diameters, and it is at this point of necking that a cap blew out. It was also noted that necking occurred at the plate boundary for the 40mm load diameter, less visible for the 33mm load diameter and not at all for the 25mm and 18.3mm load diameters. Along with necking at the boundary the formation of a step or shear lift was noted. Again this was seen for the 40mm load diameter and less so for the 33mm load diameter and not at all for the 25mm and 18.3mm load diameters. This shear lift is due to the clamping conditions at the boundary and has been investigated in detail by Thomas [9]. These above observations can be seen in Figure 4.12 to Figure 4.19.

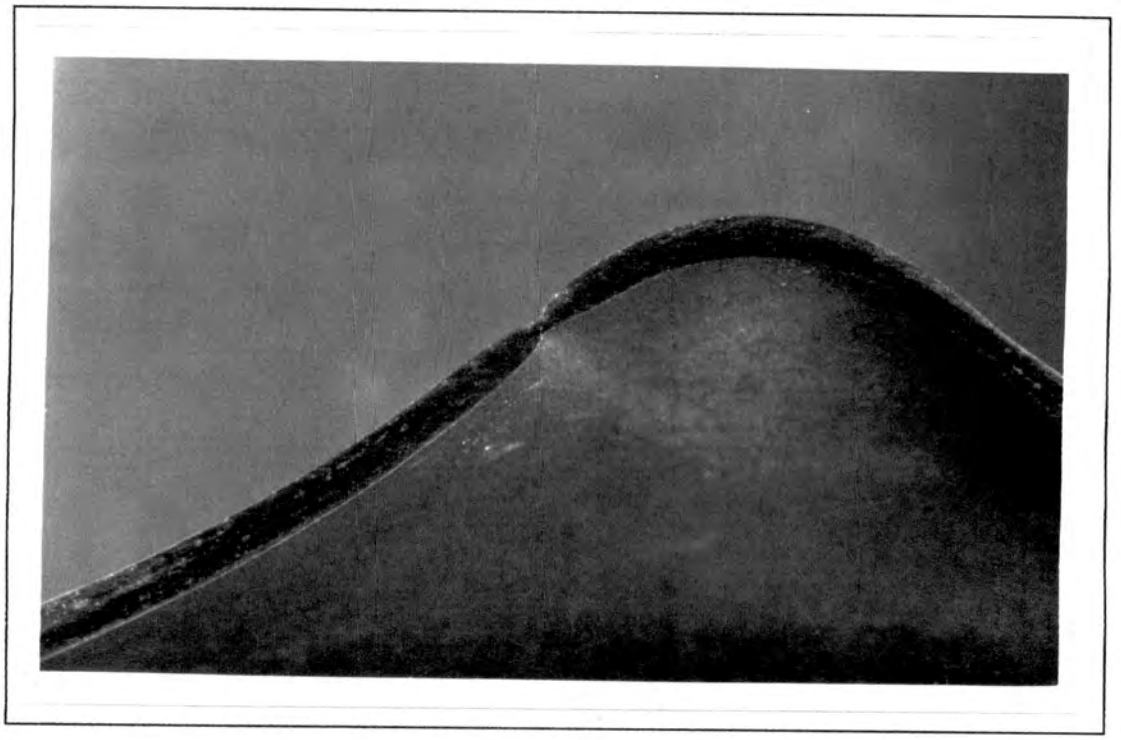

Figure 4.12 Magnification of the plate (Test No. 2310921018) around the nipple with a load diameter of 18.3mm, showing visible evidence of thinning.

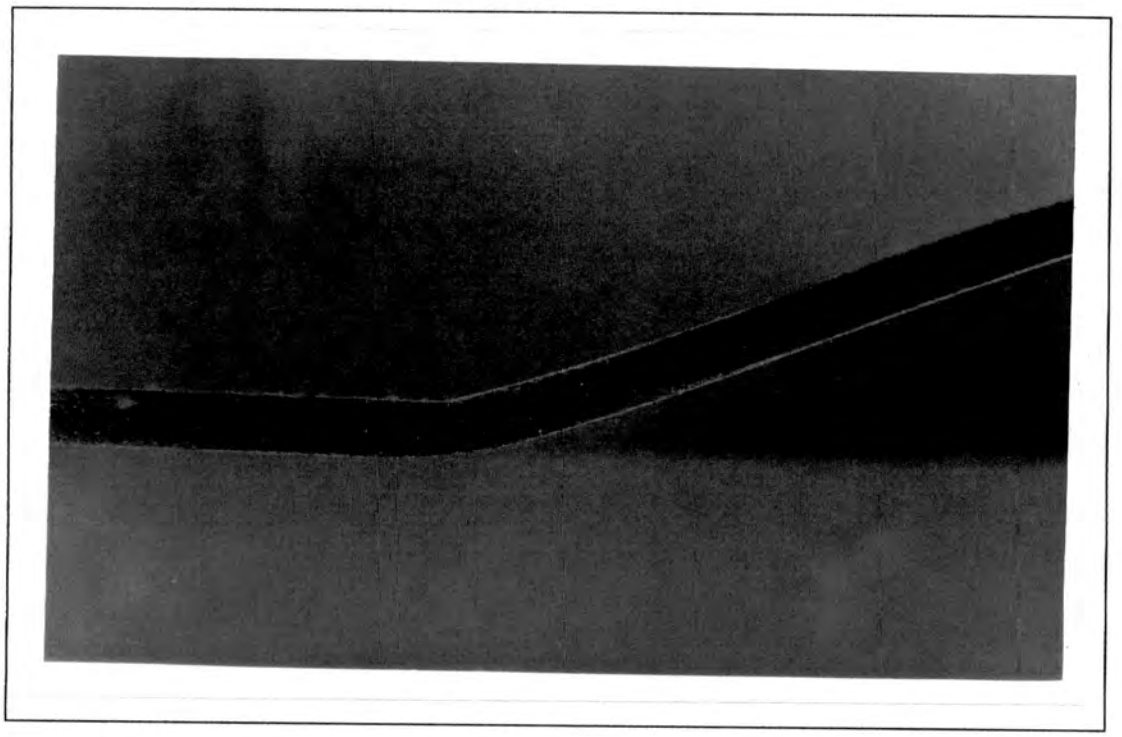

Figure 4.13 Magnification of the plate (Test No. 2310921018) at the plate boundary with a load diameter of 18.3mm, showing no visible evidence of thinning.

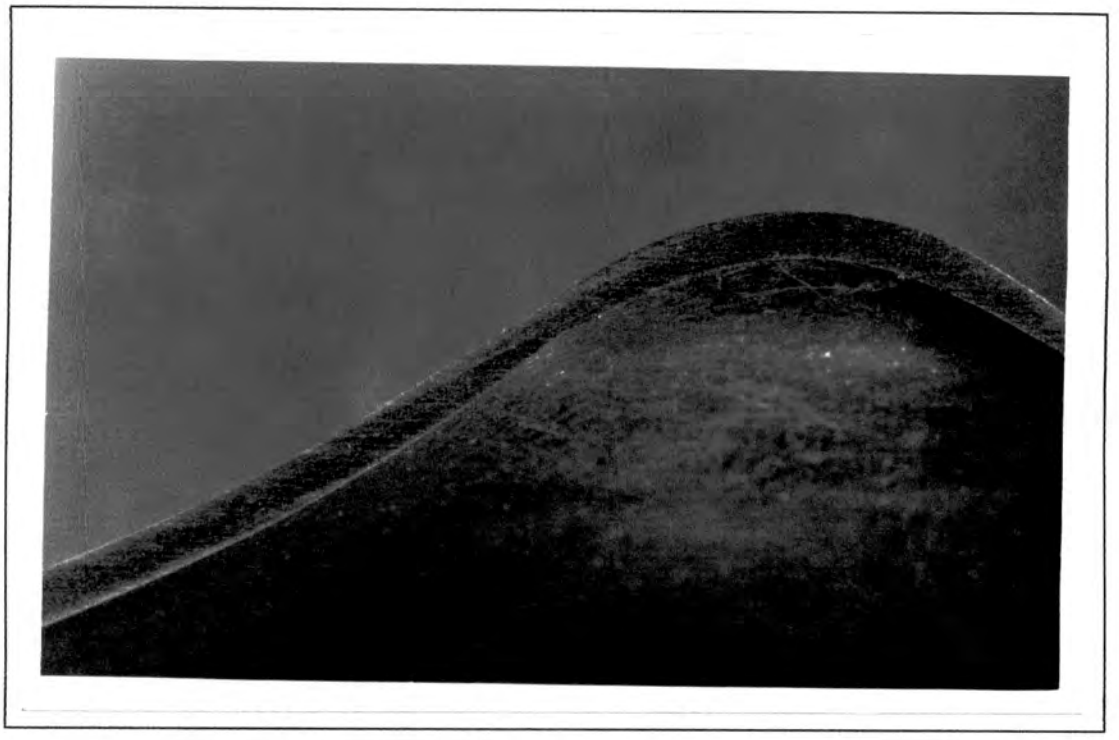

Figure 4.14 Magnification of the plate (Test No. 1010921125) around the nipple with a load diameter 25mm, showing visible evidence of thinning.

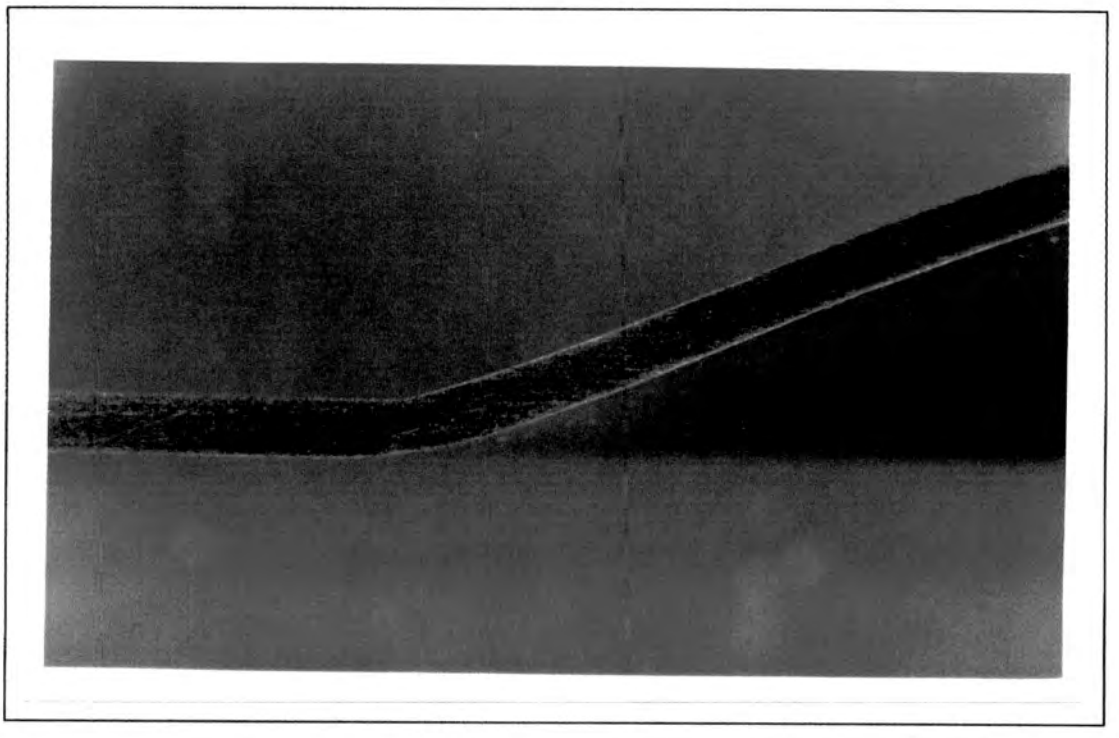

Figure 4.15 Magnification of the plate (Test No. 1010921125) at the plate boundary with a load diameter of 25mm, showing no visible evidence of thinning.

Figure 4.16 Magnification of the plate (Test No. 0516920833) around the nipple with a load diameter of 33mm, showing visible evidence of thinning.

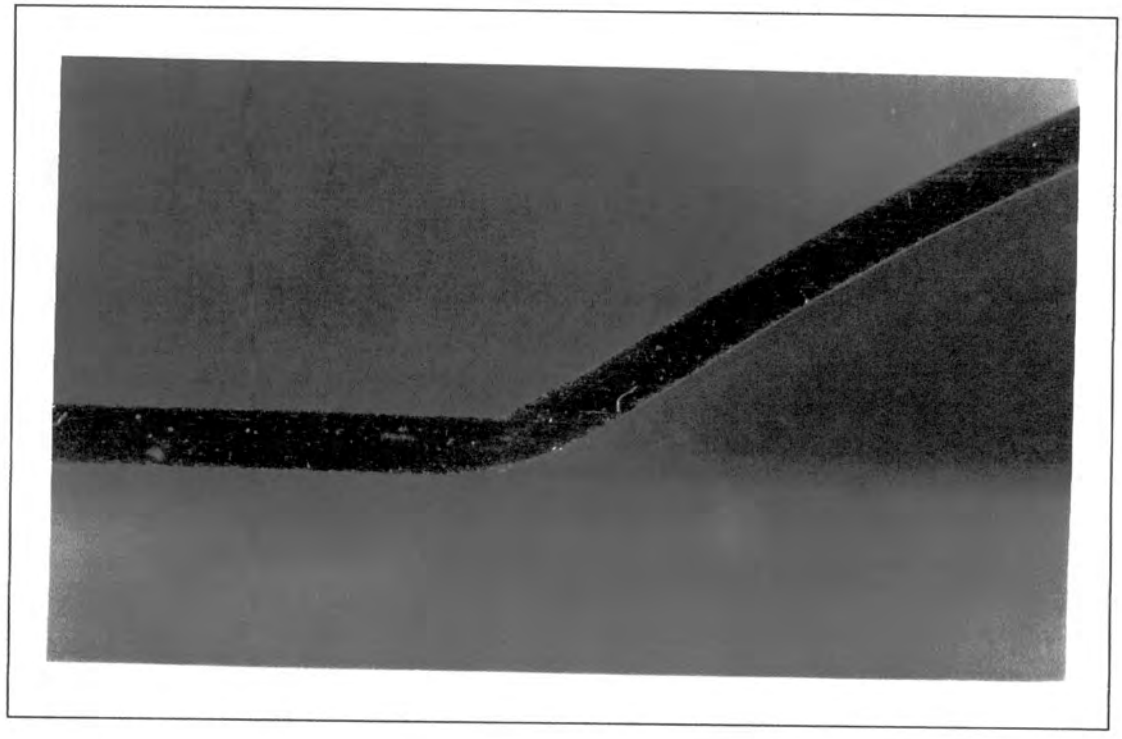

Figure 4.17 Magnification of the plate (Test No. 0516920833) at the plate diameter with a load diameter of 33mm, showing slight visible evidence of thinning.

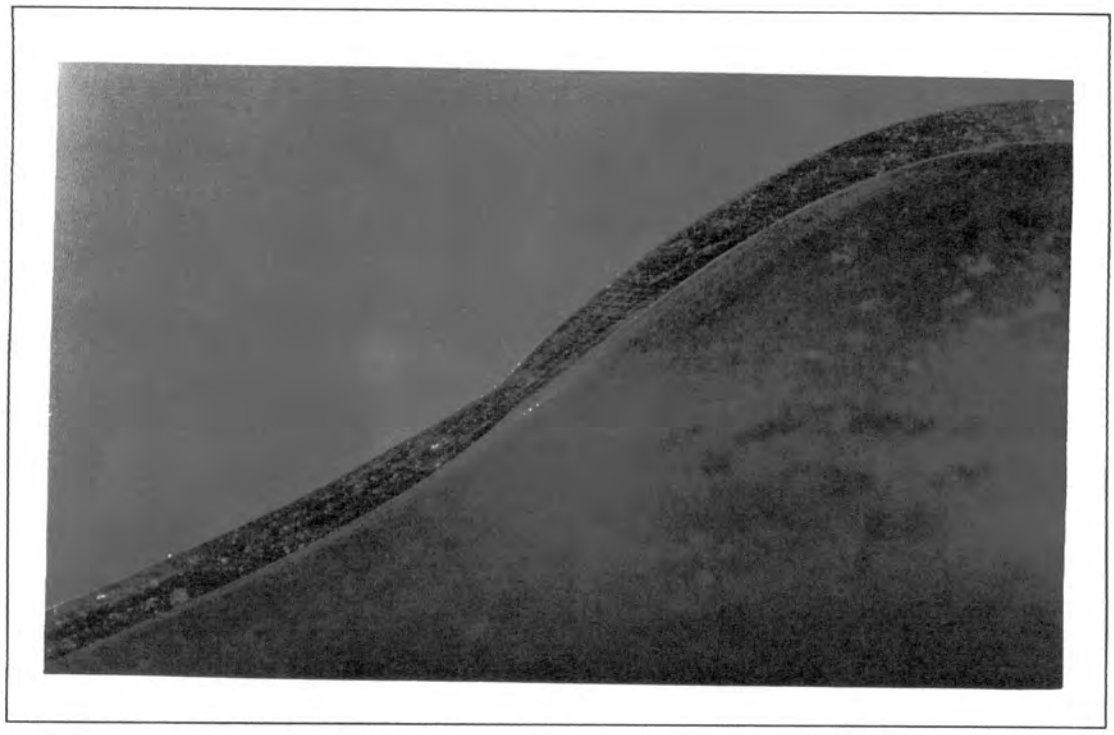

Figure 4.18 Magnification of the plate (Test No. 2910920940) around the nipple with a load diameter of 40mm, showing visible evidence of thinning.

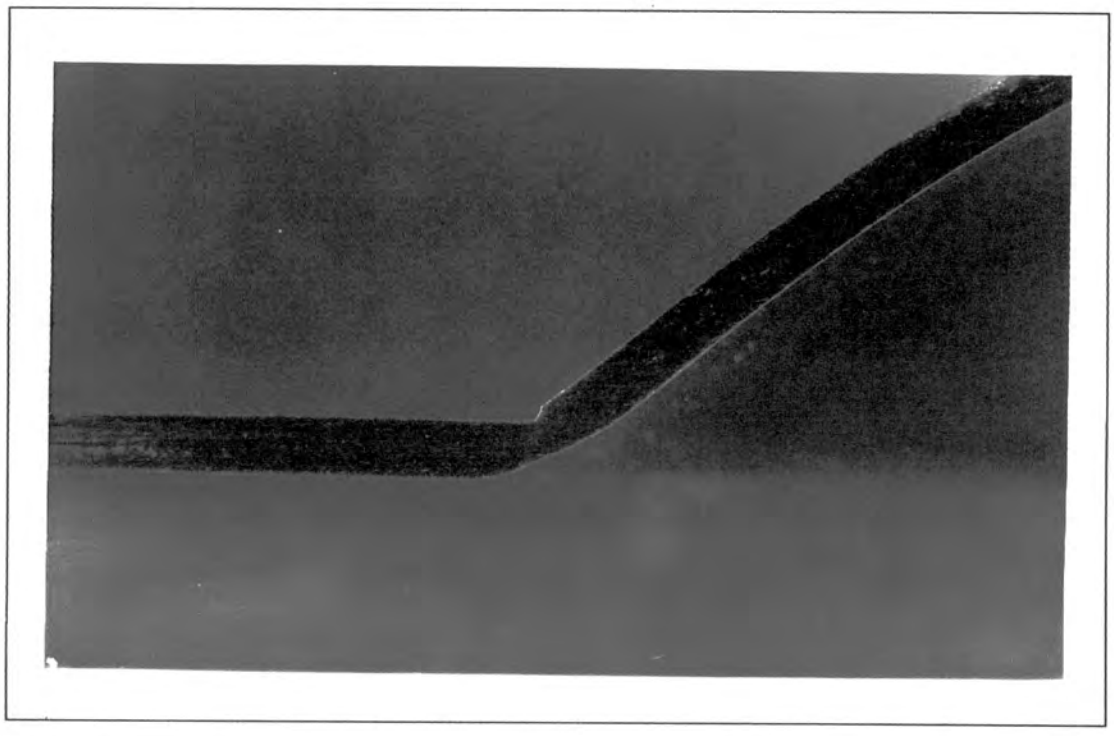

Figure 4.19 Magnification of the plate (Test No. 2910920940) at the plate boundary with a load diameter of 40mm, showing visible evidence of thinning.

4.3 EXPERIMENTAL RESULTS

The measurements taken from the test plates were the plate deflections and the cap diameter. The measurement methods used and results obtained are discussed in the next sections.

4.3.1 PLATE DEFLECTIONS

In order to measure the plate deflections, traces through the centre of the deformed plates were taken. From these traces the plate deflections were measured at 2.5mm intervals. These measurements for each of the load diameters are given in Appendix E.

4.3.2 CAP DIAMETER

As can be seen from the experimental observations, failure of the plates occurred when a cap blew out the centre of the plates. These caps although generally round in shape, exhibited random irregularities. Therefore in order to determine a cap diameter four diameter measurements for each cap were taken and an average of the four readings used. Also for each load diameter an average of all the cap diameters was taken. Both the cap and average cap diameters for each load diameter are shown in Appendix F.

The experimental mean cap to plate diameter ratios were plotted versus the load to plate diameter ratios, with a linear regression line (Eq. 4.2) through the data, as shown in Figure 4.20.

Eq. 4.2 $$\frac{\text{Cap}\phi}{\text{Plate}\phi} = 1.002 \cdot \frac{\text{Load}\phi}{\text{Plate}\phi} - 0.0514$$

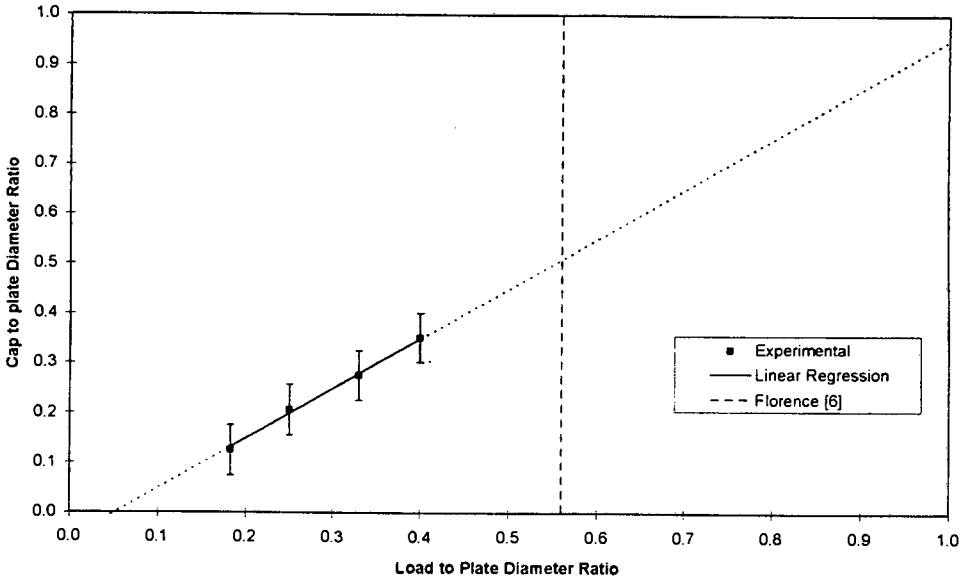

Figure 4.20 Mean cap to plate diameter ratios plotted versus the load to plate diameter ratios, with a linear regression line and predicted load to plate diameter ratio given by Florence [6], at which tearing at the plate boundary will start, plotted through the data.

Over the experimental data range, the correlation between the linear regression line and the data is good. However, substantial thinning of the plate at the plate boundary was observed for the larger load to plate diameter ratios, and hence it is reasonable to assume that at some load to plate diameter ratio smaller than one, tearing of the plate will cease at the cap diameter and start at the plate boundary. This load to plate diameter ratio was not experimentally determined and is not predicted by the linear regression line, although Florence [6], through his analysis, implied that this load to plate diameter ratio should be 0.56 as shown in Figure 4.20.

5. FINITE ELEMENT MODEL

As a comparison to the theoretical displacement model, the Abaqus explicit finite element code was used to model the deformation of thin metal plates subjected to localised impulsive loads. Farrow, Nurick and Mitchell [3] investigated the deformation of thin metal plates subjected to fully impulsive loading conditions using the Abaqus finite element code. A satisfactory correlation was obtained between their work and experimental data. The finite element model used in this document is the same in every respect as that used by Farrow, Nurick and Mitchell [3] except for the mesh used, the area over which the plate is loaded and only a pressure pulse with a triangular time history was investigated.

5.1 MODEL

The following parameters define the finite element model used to predict the deformation of thin metal plates subjected to localised loading conditions.

5.1.1 INTEGRATION SCHEME

Explicit integration was used due to it being suited to non linear dynamic problems such as thin plates subjected to impulsive loads.

5.1.2 ELEMENTS

SAX1 elements are axisymmetric, take into account thinning, finite strain behaviour and thin plate Kirchoff constraints are enforced at the reduced integration points. All these factors make the SAX1 elements ideal when modelling thin circular plates subjected to impulsive loads, and under going large deformations.

5.1.3 LOADING CONDITIONS

A uniform pressure pulse applied over the load area was used to model pressure applied to the plate by the explosive. No attempt was made to model the spread of this pressure pulse beyond the load diameter. The pressure time history was taken to be triangular in shape with the duration being approximately equal to the time for the explosive to burn completely. No other pressure time histories were considered. This model is developed below.

The time over which the pressure pulse is applied was assumed to be the time t_b for the explosive to burn completely and is given be Eq. 5.1.

Eq. 5.1 $$t_b = \frac{R_0}{V_b}$$

where R_0 is the load diameter and V_b is the explosive burn speed (7500 m/s).

The time history for the pressure pulse was taken to be triangular as shown in Figure 5.1.

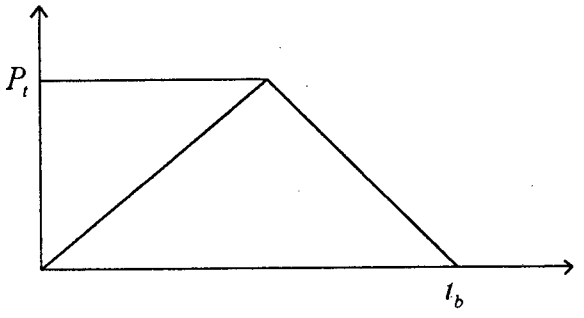

Figure 5.1 Pressure pulse time history.

P_r the peak pressure as shown in Figure 5.1 is defined as follows,

Eq. 5.2 $$P_r = \frac{2 \cdot I}{t_b \cdot A}$$

where A is the area over which the load is applied and I is the impulse applied to the plate.

5.1.4 PLATE MATERIAL MODELLING

The von Mises yield model with isotropic hardening was used to model the plate material, with strain rate effects included through the use of the Cowper-Symonds relationship.

The material properties required for the material model are, a quasistatic stress verses plastic strain curve, as shown in Figure 5.2, Young's modulus, density, Possion's ratio and static yield stress, all of which are given earlier in this document.

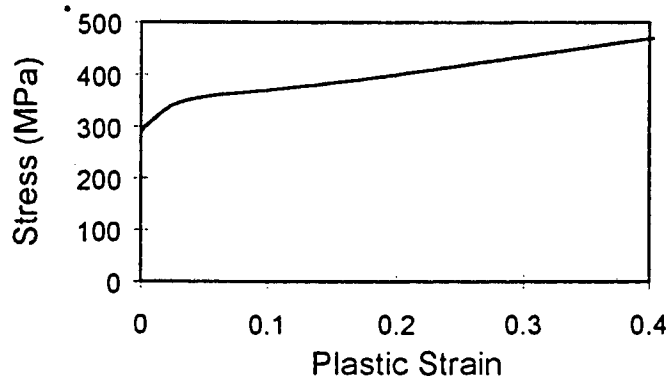

Figure 5.2 Stress plastic strain curve.

5.1.5 MESH

Farrow, Nurick and Mitchell [3] obtained satisfactory results using a 40 element mesh with boundary conditions specifying rigid clamping at the plate radius, with convergence of the solution taking place for a mesh of around 4 elements. However, with the introduction of localised loading conditions, more elements are required to obtain numerical stability of the solution. This is due to high localised plastic strains developing in the plate early on in the deformation process, as plastic hinges move towards the centre and plate radius. Around 400 elements were required to achieve numerical stability for an impulse of 1 Ns applied over a load diameter of 18.3mm.

A mesh of 400 elements evenly distributed across the plate with boundary conditions specifying ridged clamping at the plate radius is used in this analysis. No numerical convergence was checked using different meshes.

6. AFFECTS OF DISCRETISATION ON THE THEORETICAL MODEL

The number of discretised points and their distribution (mesh) affect the displacement and strain magnitudes predicted by the theoretical displacement and strain models. Therefore, it is important to investigate these affects and determine a suitable mesh to use when comparing predictions made by the theoretical displacement and strain models to experimental data.

Three meshes were used in this investigation with the number of discretised points spread evenly across their respective regions, as given in Table 6.1. Mesh 1 has its discretised points spread evenly from the plate centre to the plate radius. This results in meshes 1 and 2 for the load diameter of 40mm and plate diameter of 100mm coinciding, and meshes 2 and 3 for load to plate diameter ratio of 1/2 (as used by Bodner and Symonds [4]) coinciding.

	No. of Discretised Points		
Mesh	$0 \le r \le R_0$	$R_0 \le r \le R$	Total $(0 \le r \le R)$
1	-	-	40
2	16	24	40
3	20	20	40

Table 6.1 Meshes used in theoretical displacement and strain calculations.

6. AFFECTS OF DISCRETISATION ON THE THEORETICAL MODEL

The number of discretised points and their distribution (mesh) affect the displacement and strain magnitudes predicted by the theoretical displacement and strain models. Therefore, it is important to investigate these affects and determine a suitable mesh to use when comparing predictions made by the theoretical displacement and strain models to experimental data.

Three meshes were used in this investigation with the number of discretised points spread evenly across their respective regions, as given in Table 6.1. Mesh 1 has its discretised points spread evenly from the plate centre to the plate radius, this results in meshes 1 and 2 for the load diameter of 40mm and plate diameter of 100mm coinciding, and meshes 2 and 3 for load to plate diameter ratio of 1/2 (as used by Bodner and Symonds [4]) coinciding.

	No. of Discretised Points		
Mesh	$0 \le r \le R_0$	$R_0 \le r \le R$	Total $(0 \le r \le R)$
1	-	-	40
2	16	24	40
3	20	20	40

Table 6.1 Meshes used in theoretical displacement and strain calculations.

6.1 THEORETICAL DISPLACEMENT

The theoretical displacement is investigated in two ways, mid-point displacement $W_T(r = 0)$ and displacement profiles $W_T(r)$. The effects of the meshes given in Table 6.1 on both these displacements are discussed below.

6.1.1 MID-POINT DISPLACEMENT

For each shape function the theoretical mid-point displacement was calculated (over the experimental non-tearing impulse range) using the three meshes. This was repeated for each load to plate diameter ratio, including those used by Bodner and Symonds [4]. The results for the cubic shape function are shown in Figure 6.1 to Figure 6.6, while the results for the quadratic and linear shape functions are shown in Appendix G.

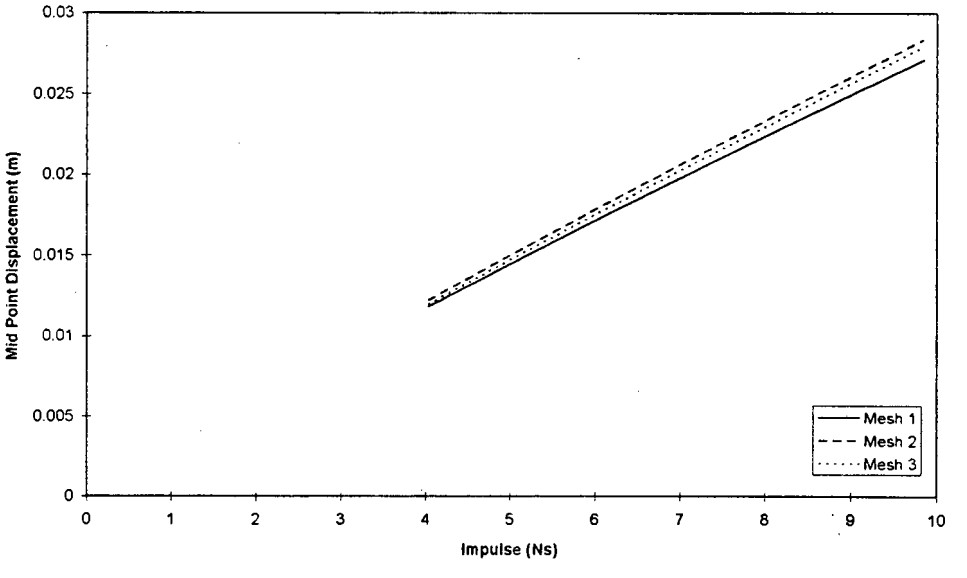

Figure 6.1 Theoretical mid-point displacement for the **cubic shape function** and **load, plate diameter** of **18.3mm** and **100mm** respectively, using the three meshes.

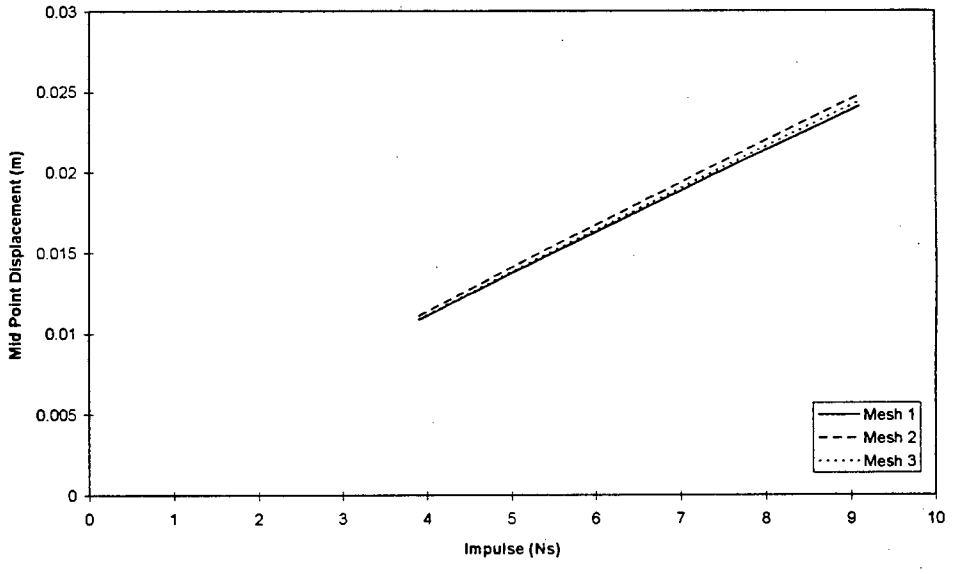

Figure 6.2 Theoretical mid-point displacement for the **cubic shape function** and **load, plate diameter** of **25mm** and **100mm** respectively, using the three meshes.

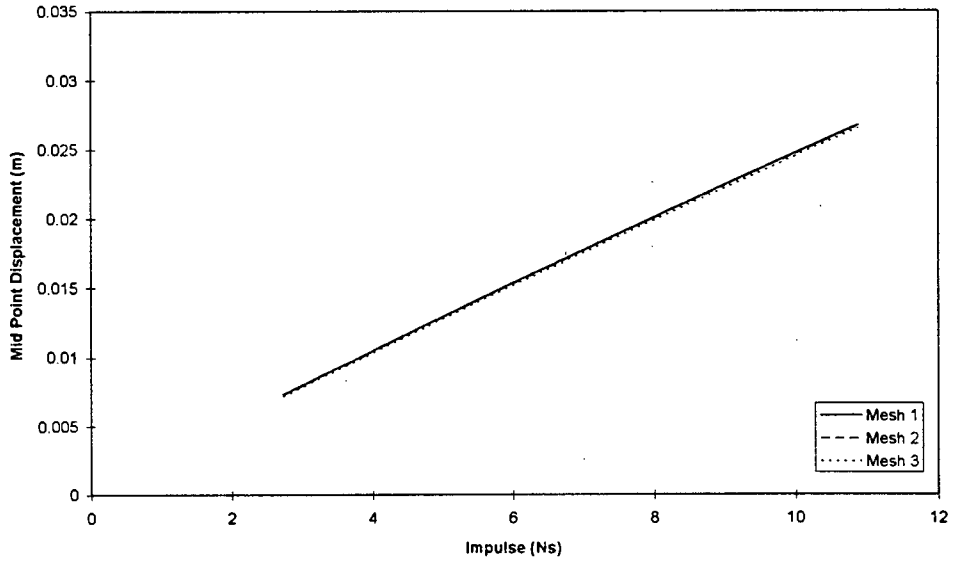

Figure 6.3 Theoretical mid-point displacement for the **cubic shape function** and **load, plate diameter** of **33mm** and **100mm** respectively, using the three meshes.

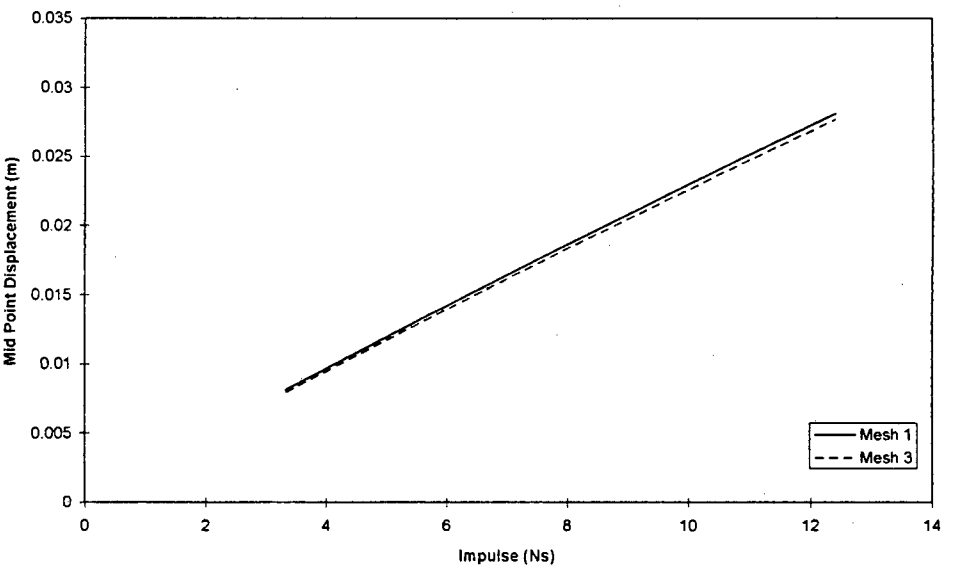

Figure 6.4 Theoretical mid-point displacement for the **cubic shape function** and **load, plate diameter** of **40mm** and **100mm** respectively, using the three meshes.

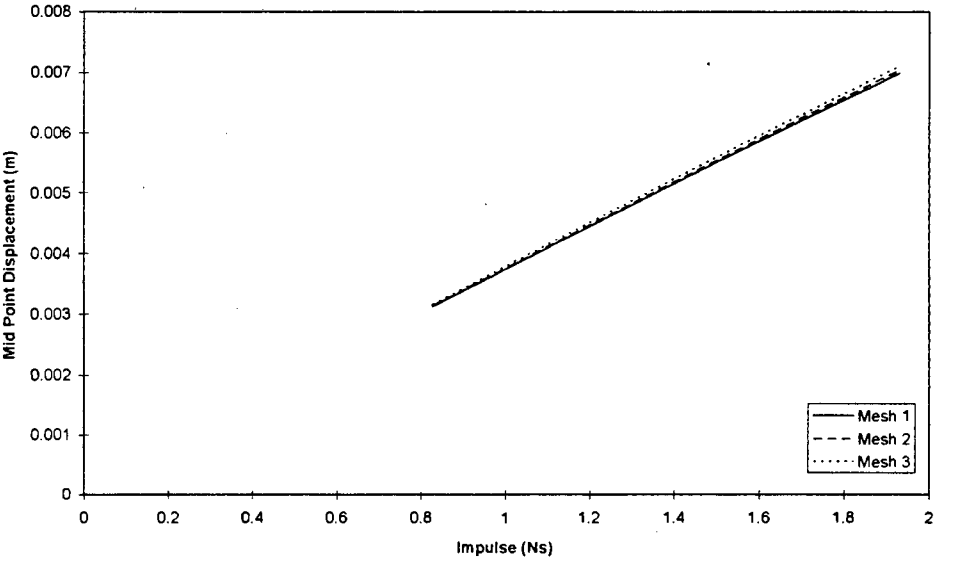

Figure 6.5 Theoretical mid-point displacement for the **cubic shape function** and **load to plate diameter ratio** of **1/3** (as used by Bodner and Symonds [4]), using the three meshes.

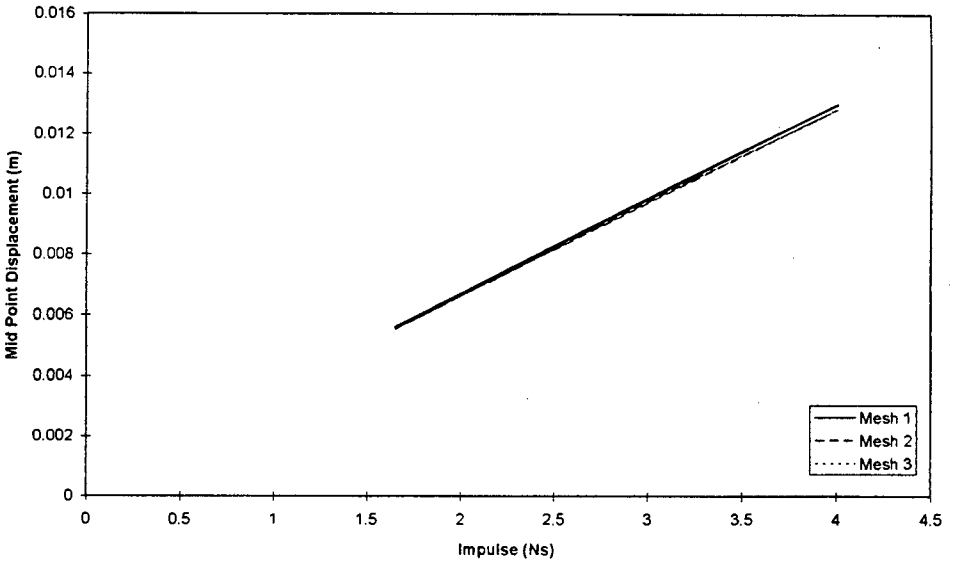

Figure 6.6 Theoretical mid-point displacement for the **cubic shape function** and **load to plate diameter ratio** of **1/2** (as used by Bodner and Symonds [4]), using the three meshes.

6.1.2 DISPLACEMENT PROFILES

For each shape function the theoretical displacement profiles were calculated using the three meshes and maximum impulse recorded prior to plate tearing. This was repeated for each load to plate diameter ratio including the ratios of 1/2 and 1/3 used by Bodner and Symonds [4]. The results for the cubic shape function are shown in Figure 6.7 to Figure 6.12, while the results for the quadratic and linear shape functions are shown in Appendix H.

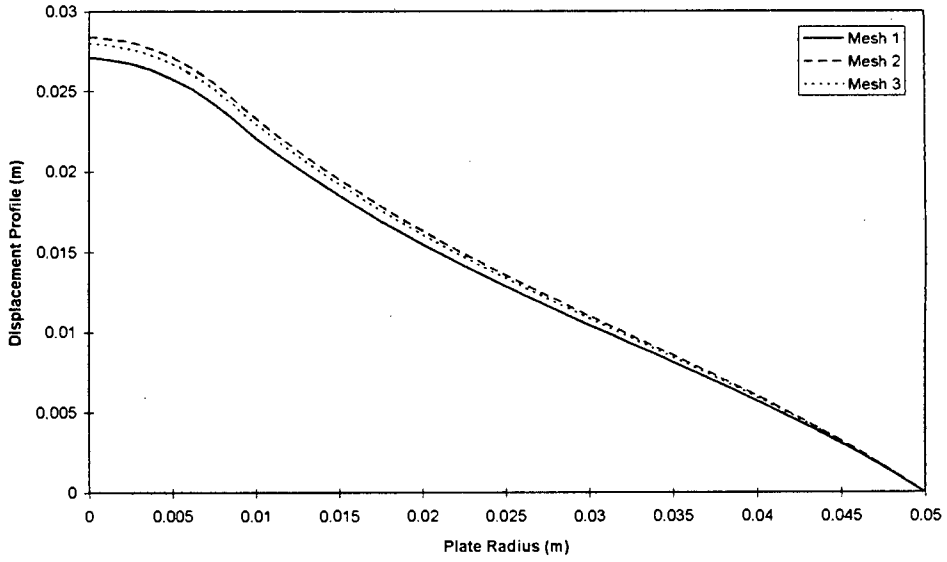

Figure 6.7 Theoretical displacement profile for the **cubic shape function, load, plate diameter** of **18.3mm** and **100mm** respectively and **impulse** of **9.85Ns,** using the three meshes.

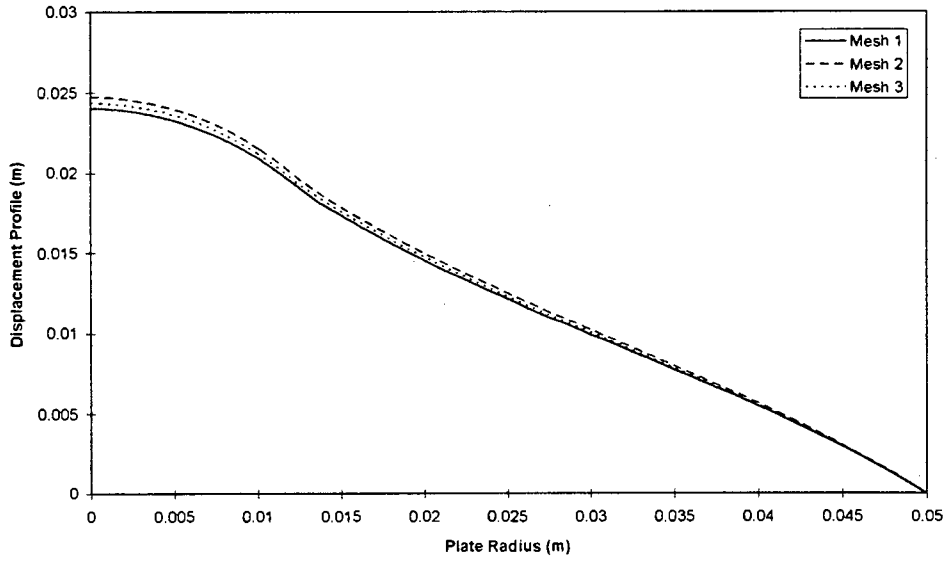

Figure 6.8 Theoretical displacement profile for the **cubic shape function, load, plate diameter** of **25mm** and **100mm** respectively and **impulse** of **9.10Ns,** using the three meshes.

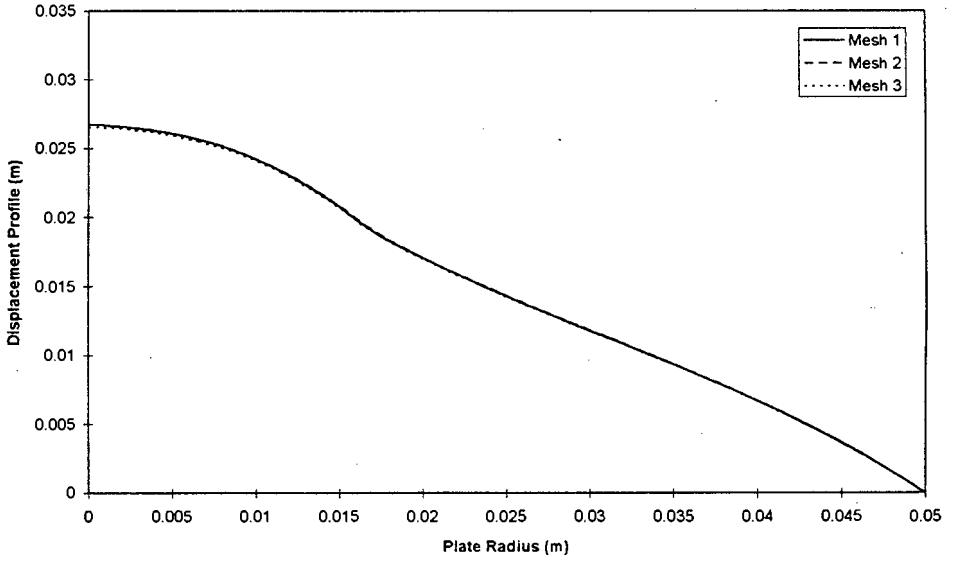

Figure 6.9 Theoretical displacement profile for the **cubic shape function, load, plate diameter** of **33mm** and **100mm** respectively and **impulse** of **10.88Ns,** using the three meshes.

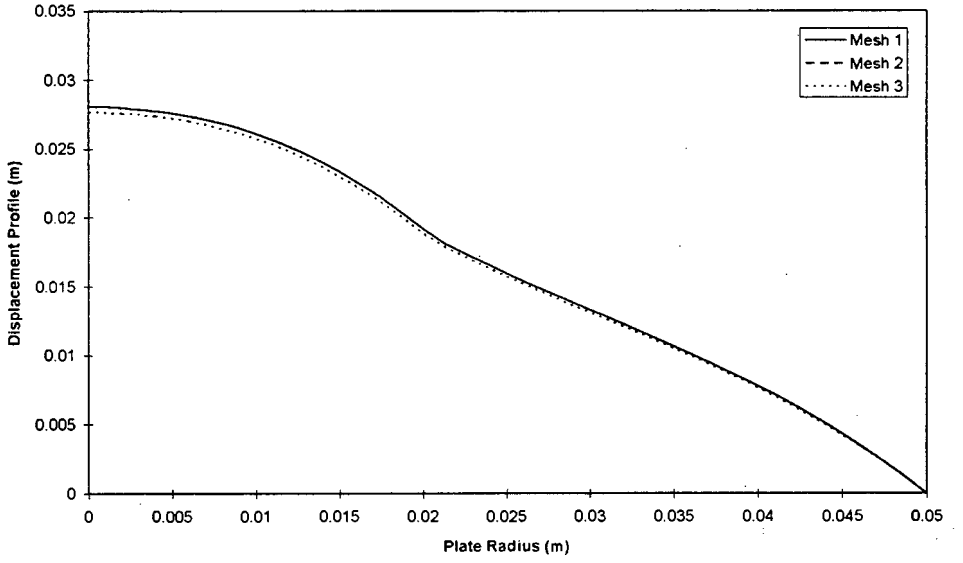

Figure 6.10 Theoretical displacement profile for the **cubic shape function, load, plate diameter** of **40mm** and **100mm** respectively and **impulse** of **12.41Ns,** using the three meshes.

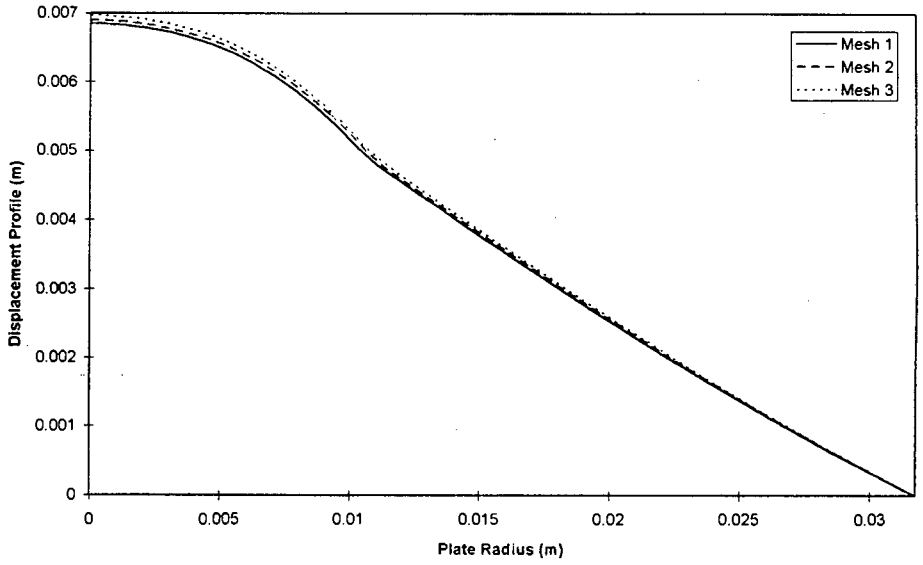

Figure 6.11 Theoretical displacement profile for the **cubic shape function, load** to **plate diameter** ratio of **1/3** (as used by Bodner and Symonds [4]) and **impulse** of **1.89Ns,** using the three meshes.

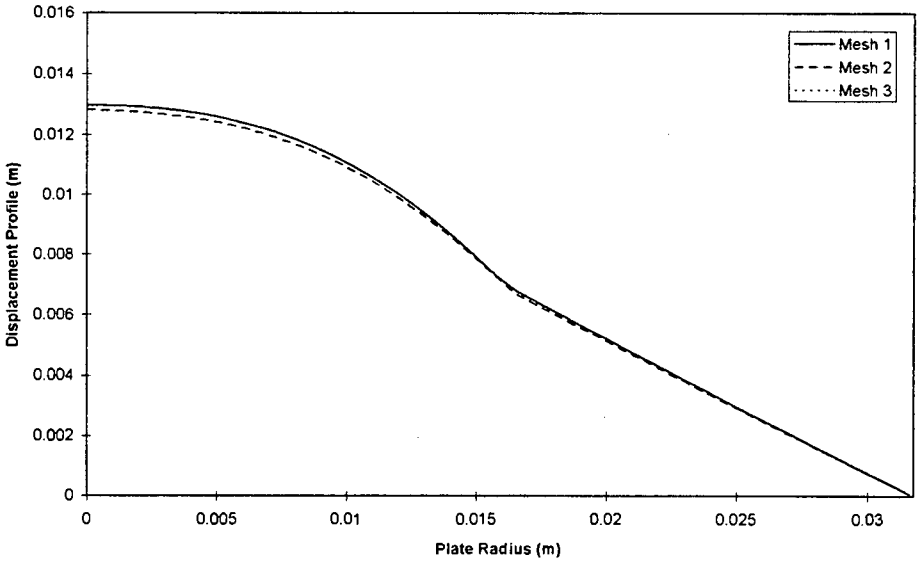

Figure 6.12 Theoretical displacement profile for the **cubic shape function, load** to **plate diameter** ratio of **1/2** (as used by Bodner and Symonds [4]) and **impulse** of **4.007Ns,** using the three meshes.

6.2 THEORETICAL STRAIN

The theoretical strain is calculated as an average between two consecutive discretised points, hence the number of discretised points and their distribution will effect this value. Therefore, the theoretical strains for each of the shape functions, the highest recorded impulse prior to plate tearing and load diameters reported in this document are compared using the three meshes. However, the effects of mesh on the theoretical strain for the load to plate diameter ratios used by Bodner and Symonds [4] are not investigated in this document since no related experimental data was reported. The results for the cubic shape function are given in Figure 6.13 to Figure 6.16, while the results for the quadratic and linear shape functions are given in Appendix I.

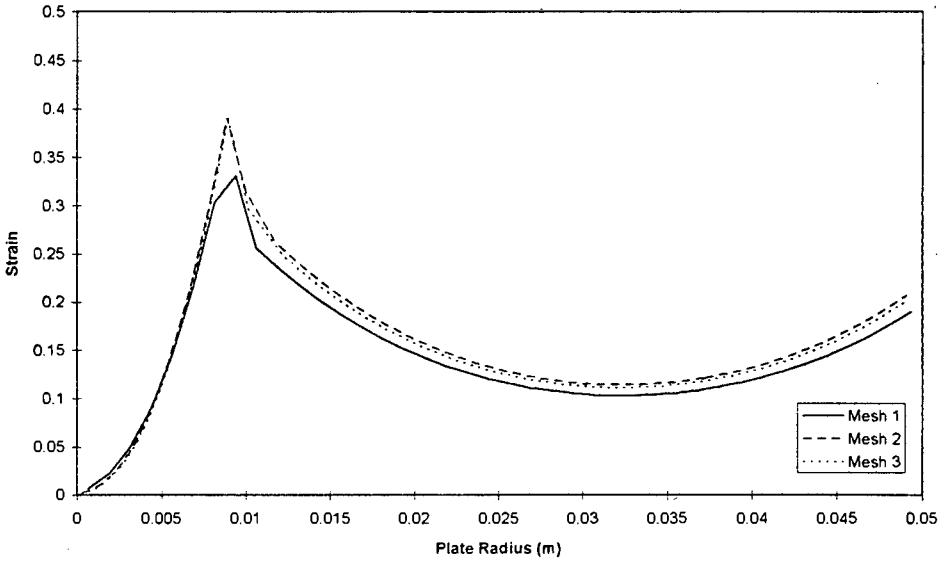

Figure 6.13 Theoretical strain distribution for the **cubic shape function, load, plate diameter** of **18.3mm** and **100mm** respectively and **impulse** of **9.85Ns,** using the three meshes.

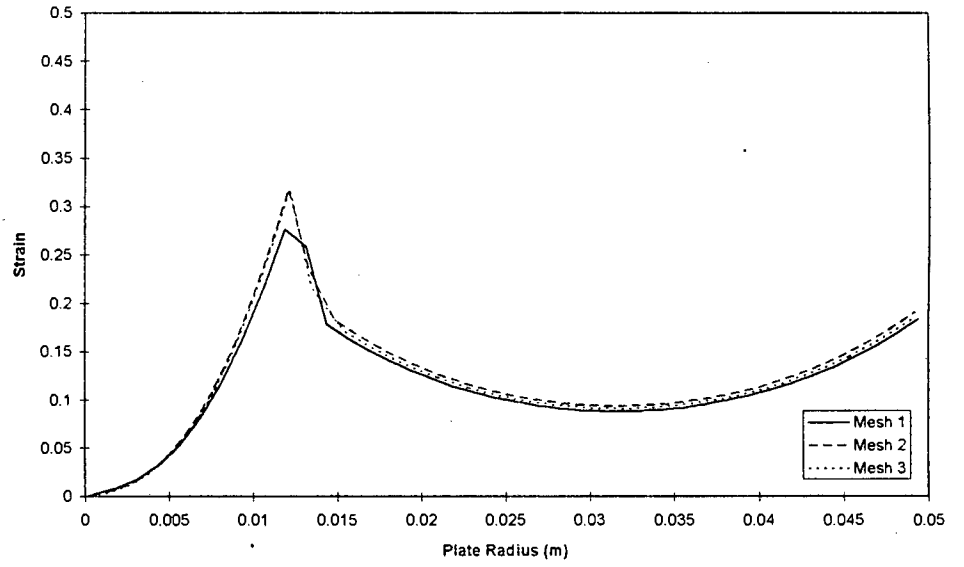

Figure 6.14 Theoretical strain distribution for the **cubic shape function, load, plate diameter** of **25mm** and **100mm** respectively and **impulse** of **9.10Ns,** using the three meshes.

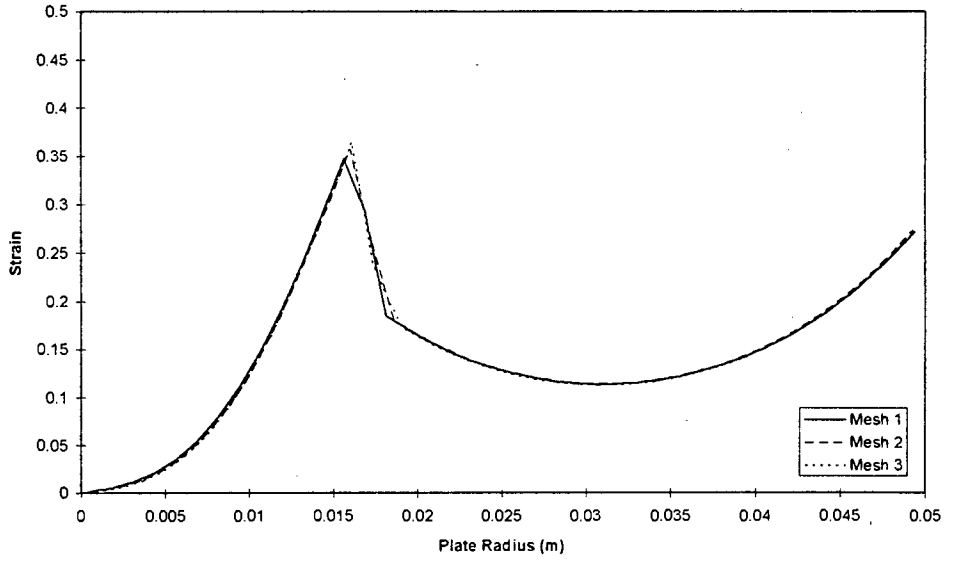

Figure 6.15 Theoretical strain distribution for the **cubic shape function, load, plate diameter** of **33mm** and **100mm** respectively and **impulse** of **10.88Ns,** using the three meshes.

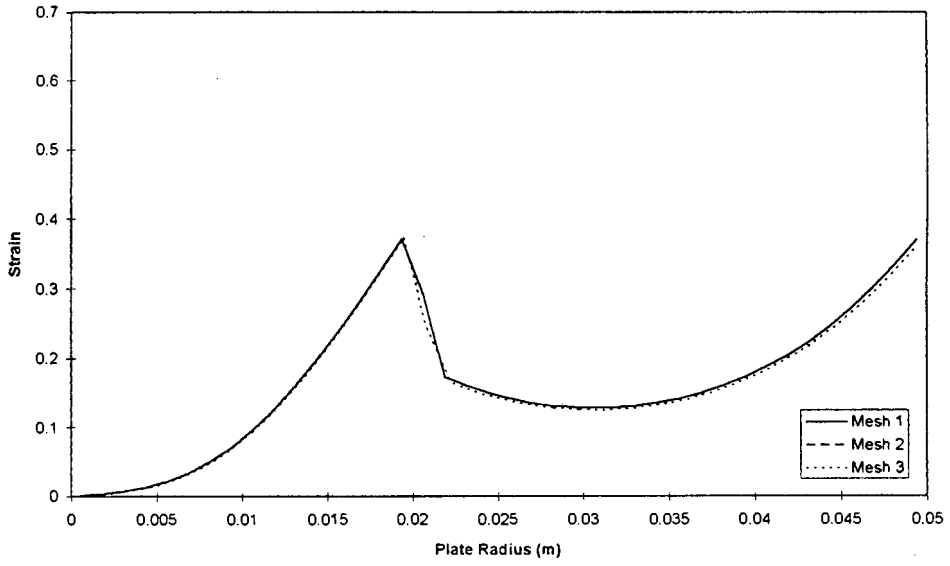

Figure 6.16 Theoretical strain distribution for the **cubic shape function, load, plate diameter** of **40mm** and **100mm** respectively and **impulse** of **12.41Ns,** using the three meshes.

6.3 DISCUSSION AND CONCLUSIONS

Analysing Figure 6.1 to Figure 6.12 and figures in Appendix G and H it can be seen that the theoretical mid-point displacements and plate displacement profiles are relatively insensitive to the mesh used. This can be attributed to the method by which the initial velocity amplitude V_0 is calculated. This method in short states that for the same impulse, the initial velocity amplitude calculated for a larger number of burn points is smaller in comparison to that calculated for a small number of burn points. This relationship between the number of burn points and the initial velocity amplitude is approximately proportional. The initial velocity amplitude determines the magnitude of the displacement fields, hence for a large initial velocity amplitude (small number of burn points) the displacement fields will have a large displacement when compared to displacement fields having a small initial velocity amplitude (large number of burn points). Hence when finding the total displacement by summing each displacement

field at each burn point, summing displacement fields with large displacements over few burn points, gives approximately the same result as summing displacement fields with small displacements over a large number of burn points.

Due to the method used to calculate the strain in the plate, the magnitude will be mesh dependent and convergence of the solution will depend on the number of discretised points and their distribution across the plate. As can be seen from Figure 6.13 to Figure 6.16 and figures shown in Appendix I the theoretical strain converges through meshes 1 to 3, resulting in very little change in values between meshes 2 and 3.

Considering the affect of the three meshes on the theoretical mid-point displacement, displacement profiles and strain, it was decided to use mesh 3 when making comparisons between the above mentioned theoretical predictions and experimentally determined data.

7. RESULTS

In the following section the predictions from models presented and developed in this document are compared to experimental results.

7.1 THEORETICAL DISPLACEMENT

In the following two sections the theoretical displacement model using the cubic, quadratic and linear shape functions are compared to experimental data for both the mid-point displacements and displacement profiles.

7.1.1 MID-POINT DISPLACEMENT

The experimental mid-point displacements obtained from data given in this document and data given by Bodner and Symonds [4] are compared to mid-point displacements given by the theoretical displacement model. These results are shown in Figure 7.1 to Figure 7.6.

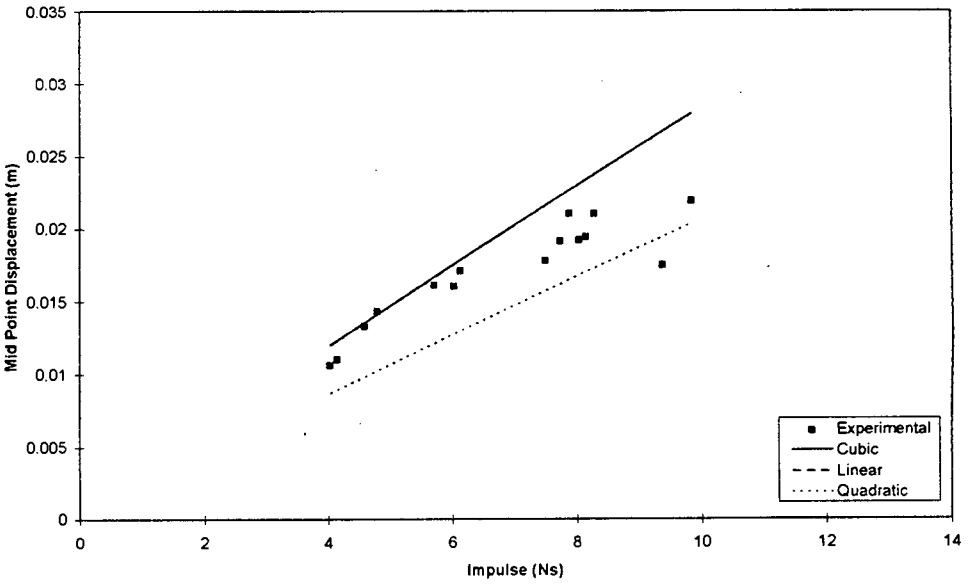

Figure 7.1 Comparison between experimental and theoretical mid-point displacements for the cubic, quadratic and linear shape functions, **plate diameter 100mm** and **load diameter 18.3mm.**

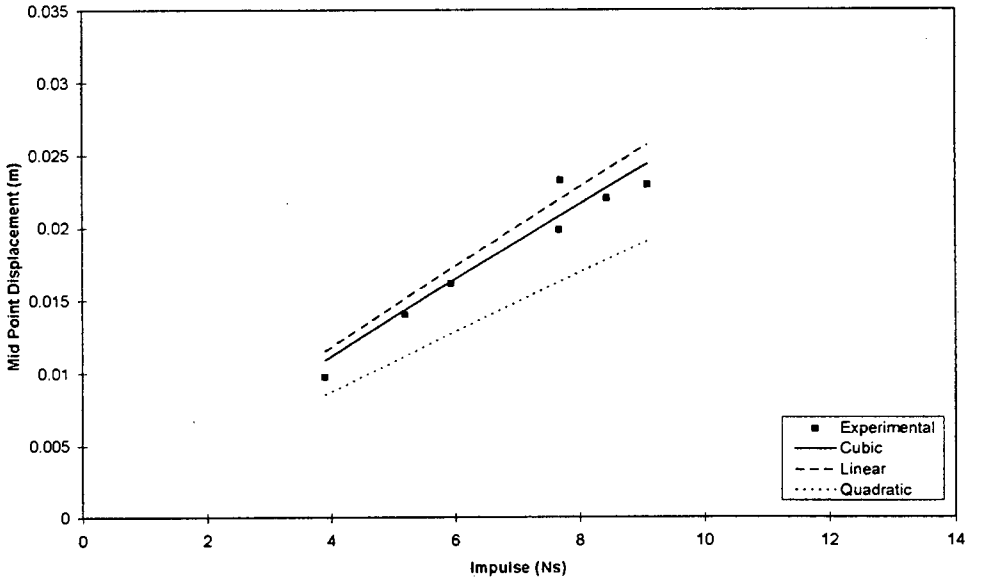

Figure 7.2 Comparison between experimental and theoretical mid-point displacements for the cubic, quadratic and linear shape functions, **plate diameter 100mm** and **load diameter 25mm.**

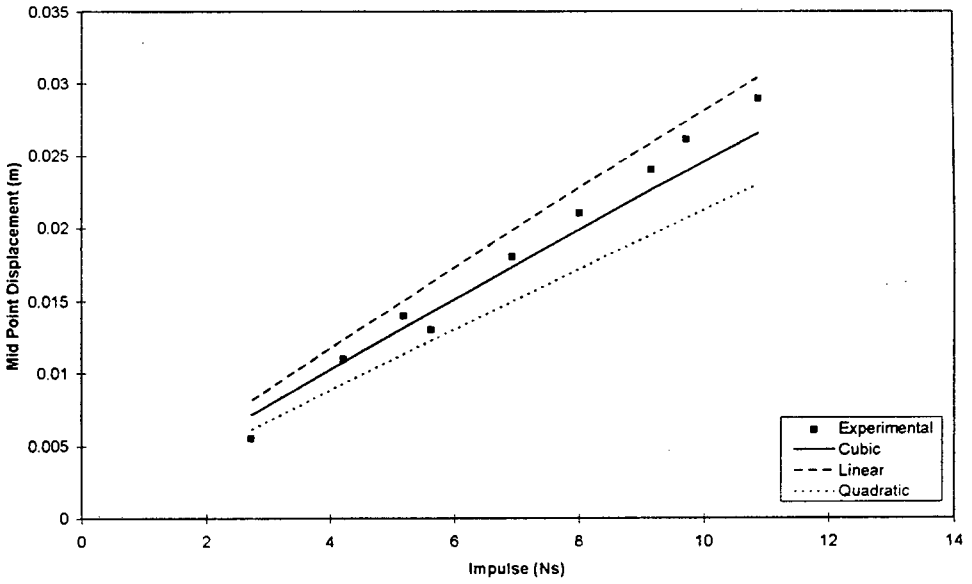

Figure 7.3 Comparison between experimental and theoretical mid-point displacements for the cubic, quadratic and linear shape functions, **plate diameter 100mm** and **load diameter 33mm.**

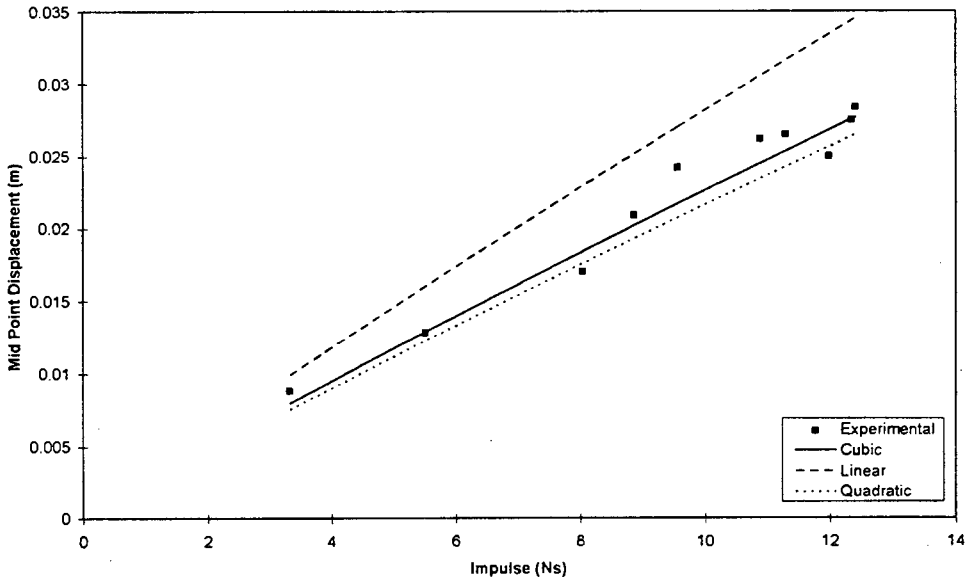

Figure 7.4 Comparison between experimental and theoretical mid-point displacements for the cubic, quadratic and linear shape functions, **plate diameter 100mm** and **load diameter 40mm.**

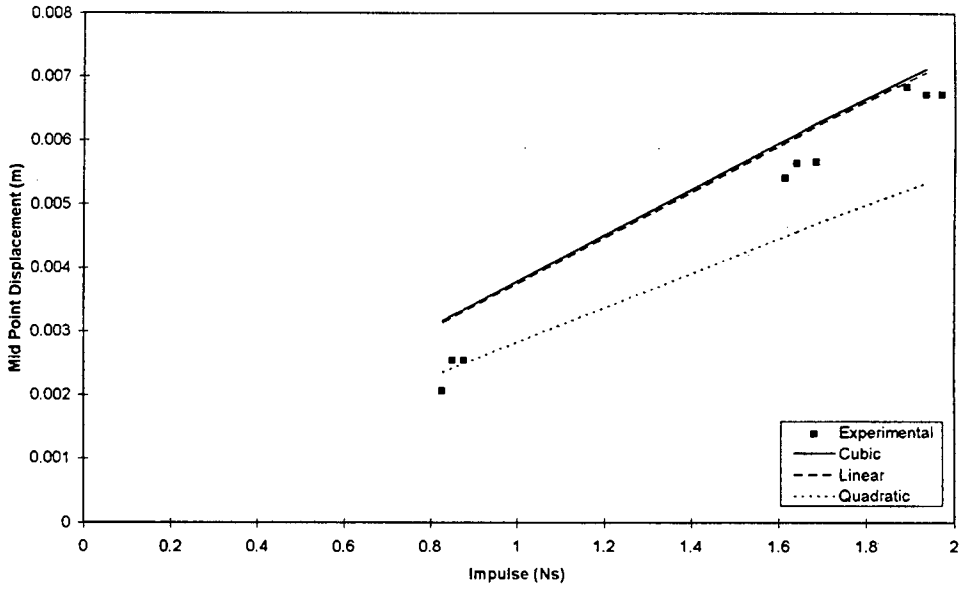

Figure 7.5 Comparison between experimental and theoretical mid-point displacements for the cubic, quadratic and linear shape functions and **load to plate diameter ratio** of **1/3** (as used by Bodner and Symonds [4]).

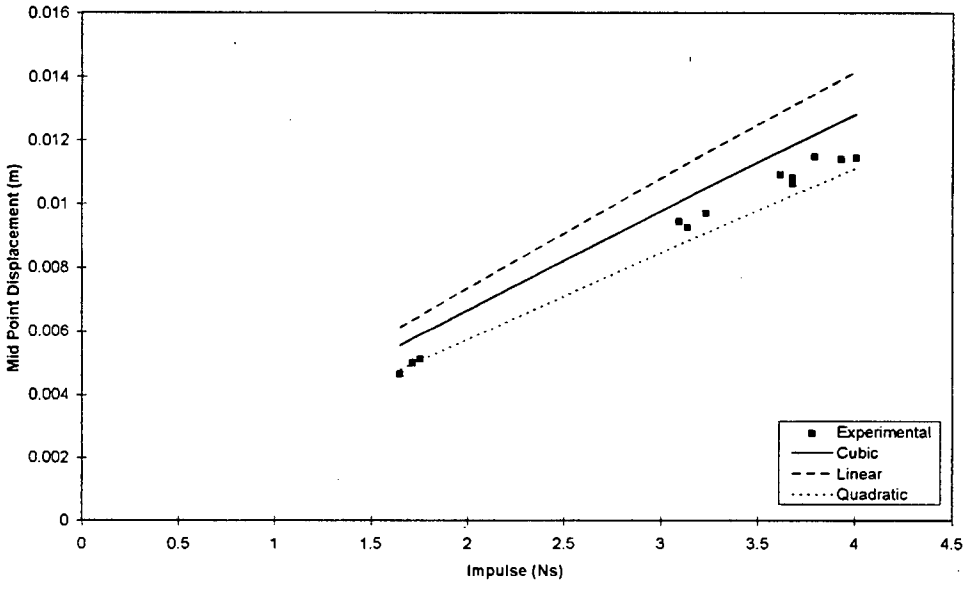

Figure 7.6 Comparison between experimental and theoretical mid-point displacements for the cubic, quadratic and linear shape functions and **load to plate diameter ratio** of **1/2** (as used by Bodner and Symonds [4]).

7.1.2 DISPLACEMENT PROFILES

The experimental displacement profiles obtained in this document and the only displacement profile for steel plates (Test No. 51) given by Bodner and Symonds [4], are compared to the theoretical displacement model using the cubic, quadratic and linear shape functions. The results are shown in Figure 7.7 to Figure 7.20 and in Appendix J.

7.1.2.1 18.3mm LOAD DIAMETER AND 100mm PLATE DIAMETER

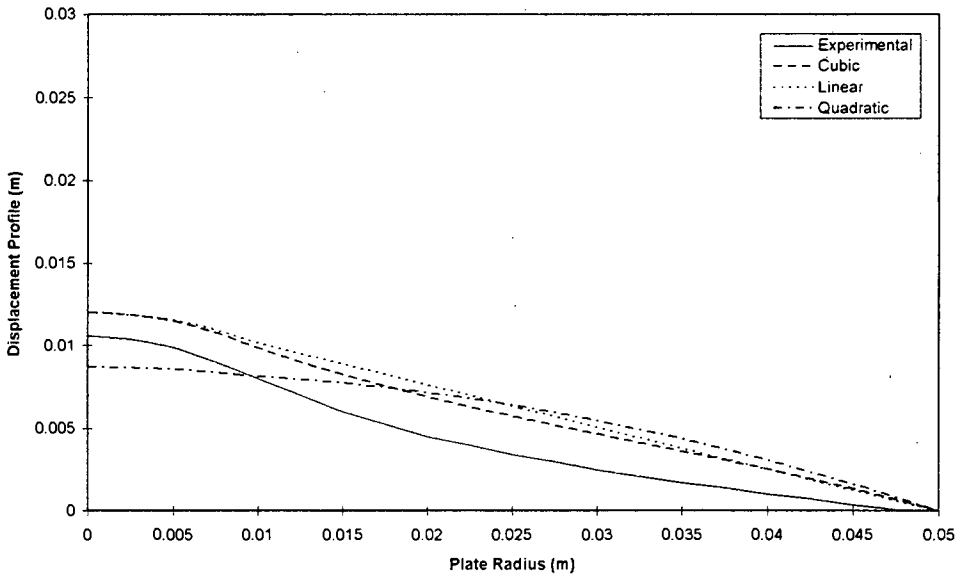

Figure 7.7 Comparison between experimental and theoretical displacement profiles for the cubic, quadratic and linear shape functions, **plate diameter 100mm, load diameter 18.3mm** and **impulse** of **4.03Ns.**

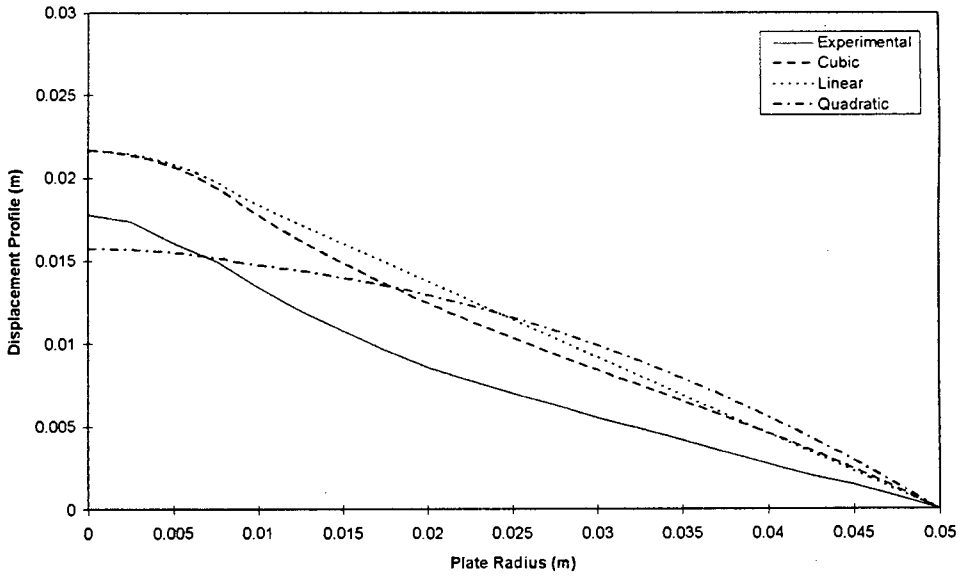

Figure 7.8 Comparison between experimental and theoretical displacement profiles for the cubic, quadratic and linear shape functions, **plate diameter 100mm, load diameter 18.3mm** and **impulse** of **7.51Ns**

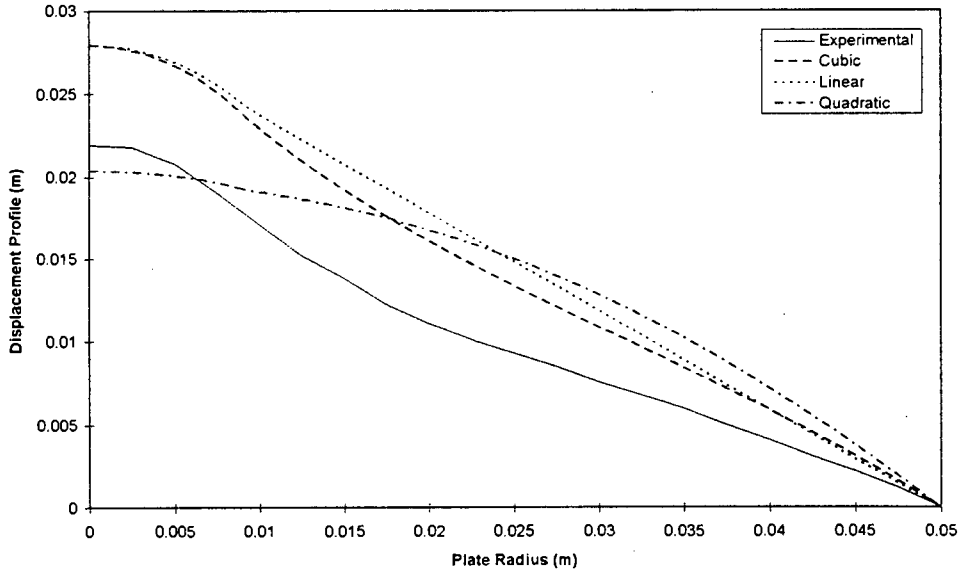

Figure 7.9 Comparison between experimental and theoretical displacement profiles for the cubic, quadratic and linear shape functions, **plate diameter 100mm, load diameter 18.3mm** and **impulse** of **9.85Ns.**

7.1.2.2 25mm LOAD DIAMETER AND 100mm PLATE DIAMETER

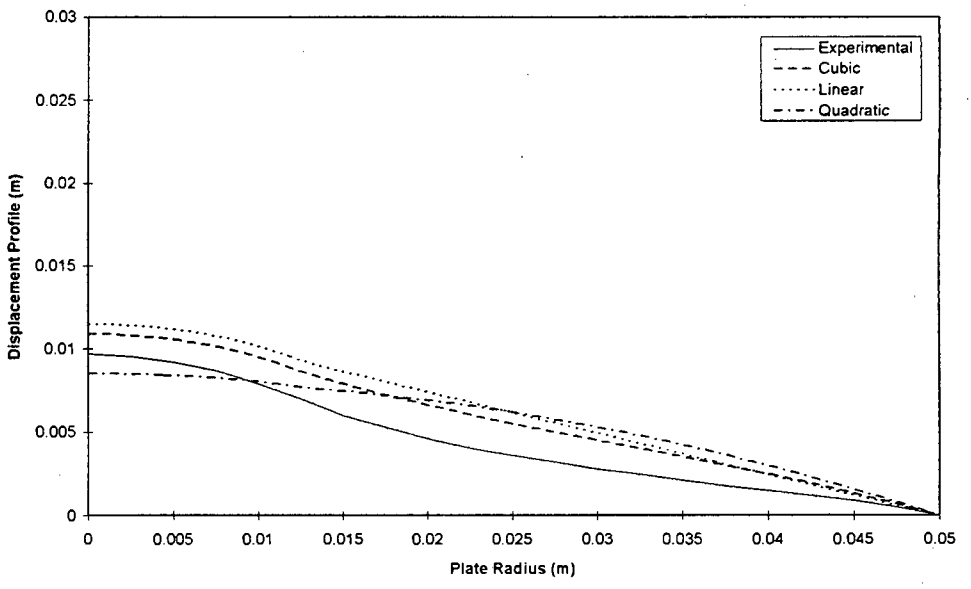

Figure 7.10 Comparison between experimental and theoretical displacement profiles for the cubic, quadratic and linear shape functions, **plate diameter 100mm, load diameter 25mm** and **impulse** of **3.9Ns.**

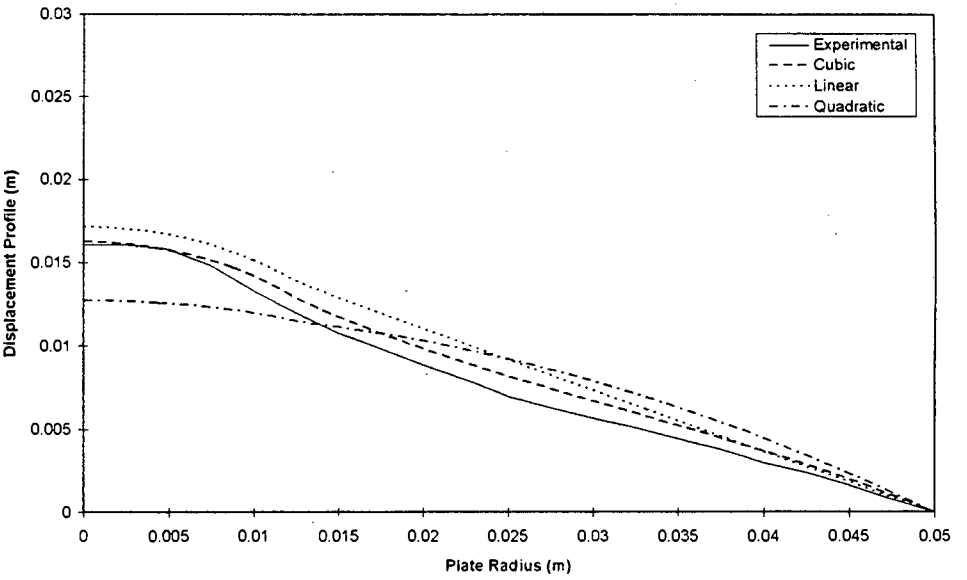

Figure 7.11 Comparison between experimental and theoretical displacement profiles for the cubic, quadratic and linear shape functions, **plate diameter 100mm, load diameter 25mm** and **impulse** of **5.94Ns.**

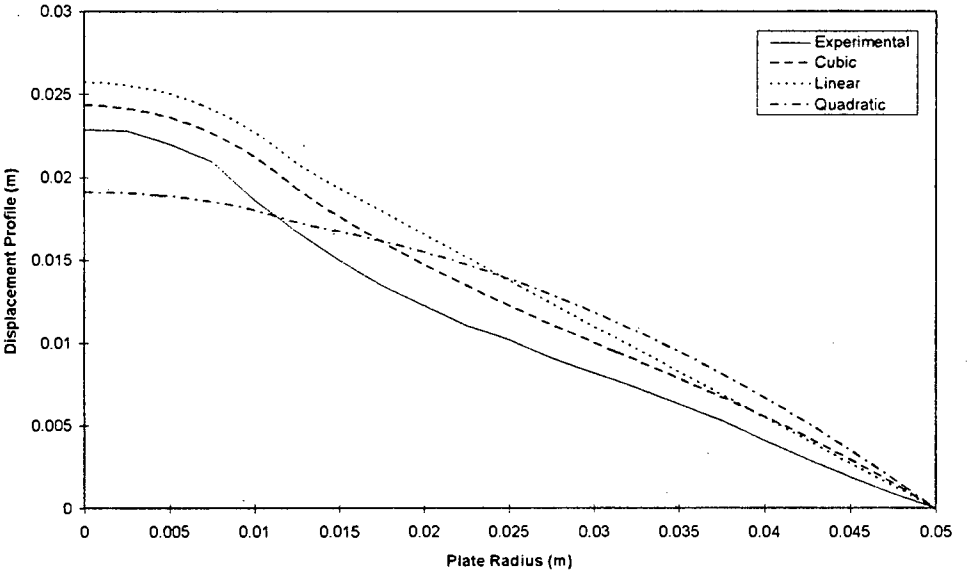

Figure 7.12 Comparison between experimental and theoretical displacement profiles for the cubic, quadratic and linear shape functions, **plate diameter 100mm, load diameter 25mm** and **impulse** of **9.10Ns.**

7.1.2.3 33mm LOAD DIAMETER AND 100mm PLATE DIAMETER

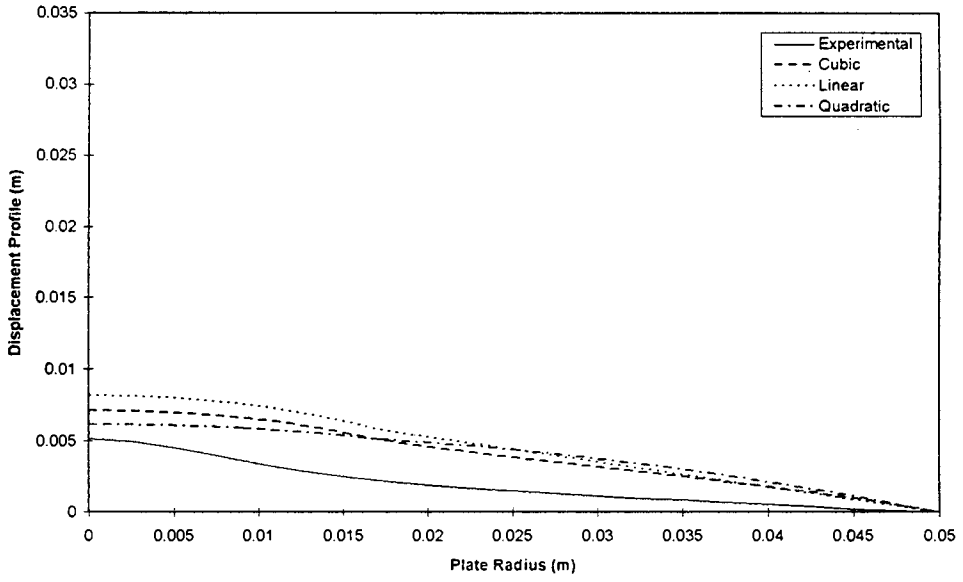

Figure 7.13 Comparison between experimental and theoretical displacement profiles for the cubic, quadratic and linear shape functions, **plate diameter 100mm, load diameter 33mm** and **impulse** of **2.73Ns.**

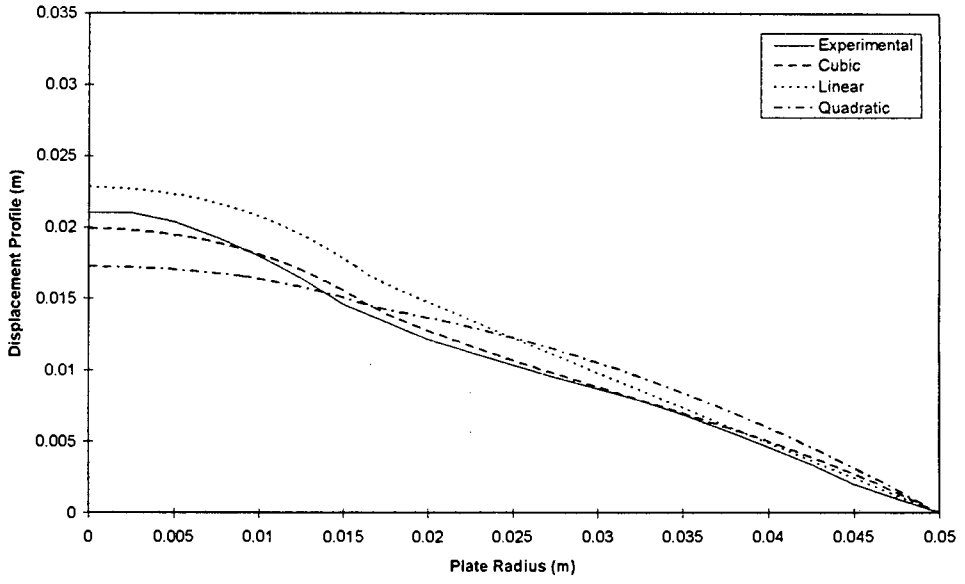

Figure 7.14 Comparison between experimental and theoretical displacement profiles for the cubic, quadratic and linear shape functions, **plate diameter 100mm, load diameter 33mm** and **impulse** of **8.02Ns.**

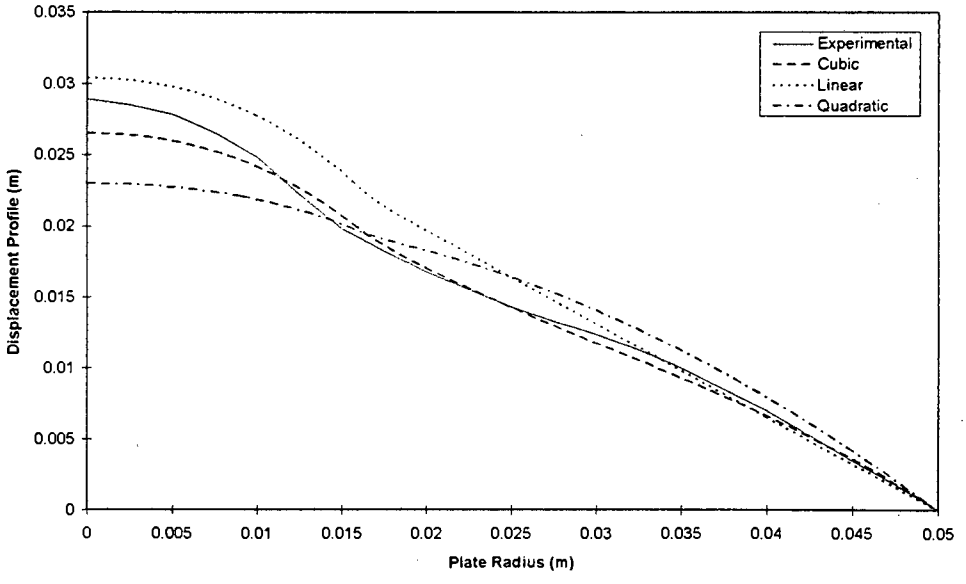

Figure 7.15 Comparison between experimental and theoretical displacement profiles for the cubic, quadratic and linear shape functions, **plate diameter 100mm, load diameter 33mm** and **impulse** of **10.88Ns.**

7.1.2.4 40mm LOAD DIAMETER AND 100mm PLATE DIAMETER

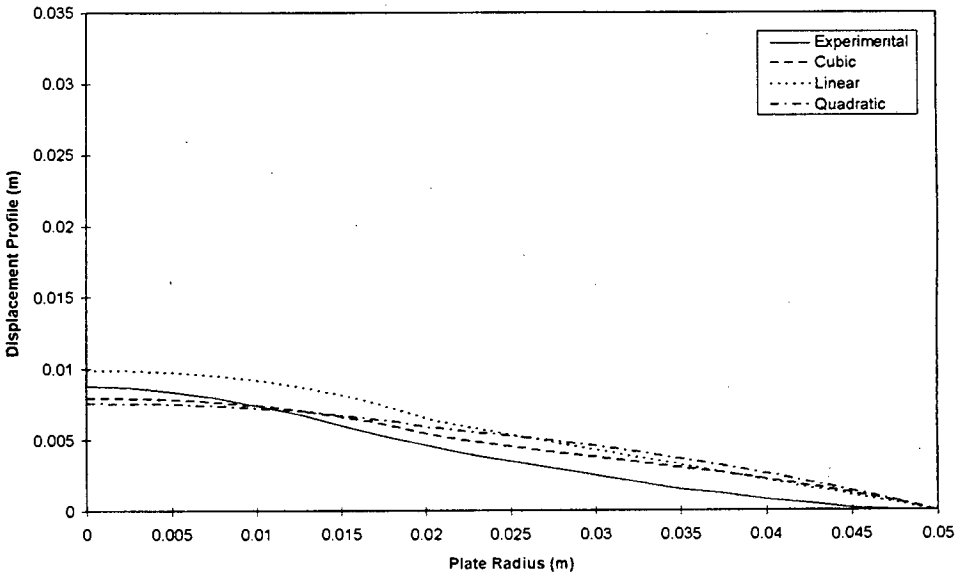

Figure 7.16 Comparison between experimental and theoretical displacement profiles for the cubic, quadratic and linear shape functions, **plate diameter 100mm, load diameter 40mm** and **impulse** of **3.33Ns.**

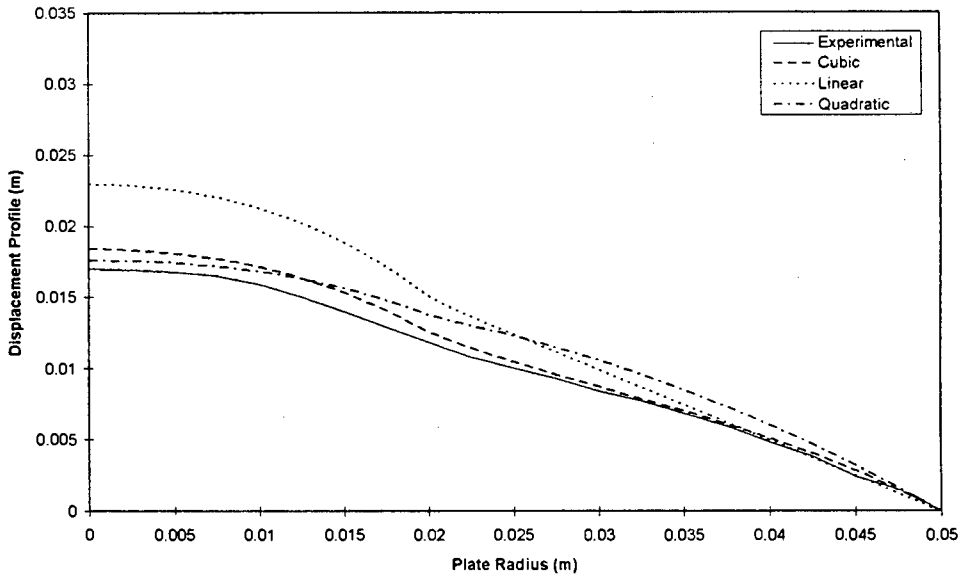

Figure 7.17 Comparison between experimental and theoretical displacement profiles for the cubic, quadratic and linear shape functions, **plate diameter 100mm, load diameter 40mm** and **impulse** of **8.04Ns.**

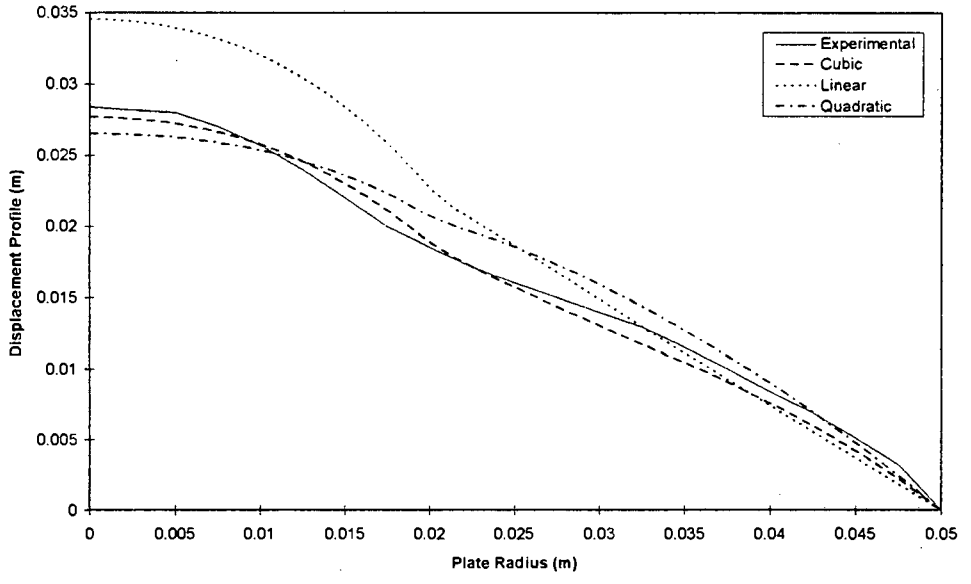

Figure 7.18 Comparison between experimental and theoretical displacement profiles for the cubic, quadratic and linear shape functions, **plate diameter 100mm, load diameter 40mm** and **impulse** of **12.41Ns.**

7.1.2.5 1/3 LOAD TO PLATE DIAMETER RATIO AS USED BY BODNER AND SYMONDS

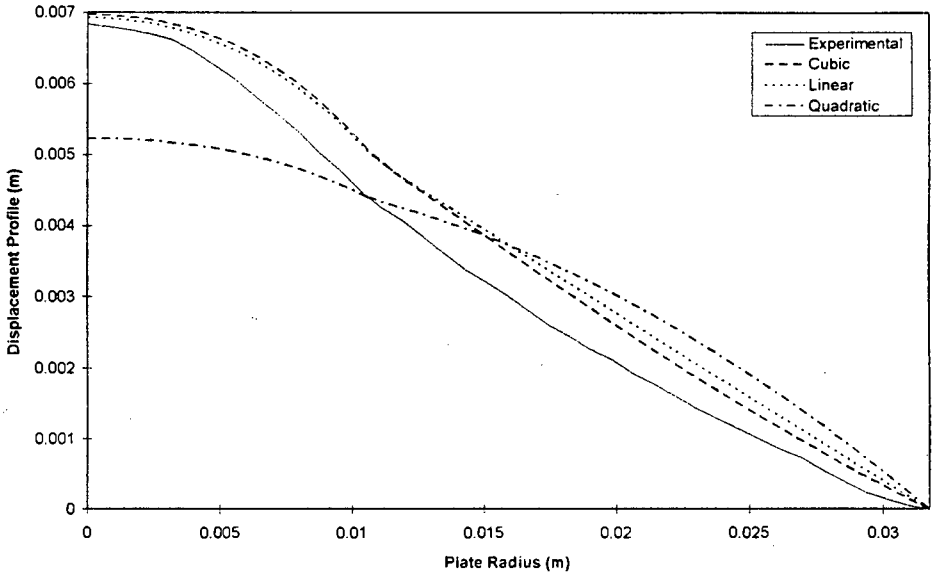

Figure 7.19 Comparison between experimental and theoretical displacement profiles for the cubic, quadratic and linear shape functions, **load to plate diameter ratio of 1/3** and **impulse** of **1.89Ns.**

7.1.2.6 1/2 LOAD TO PLATE DIAMETER RATIO AS USED BY BODNER AND SYMONDS

Although no experimental displacement profiles for steel plates with a load to plate diameter ratio of 1/2 are given by Bodner and Symonds [4], for completeness the theoretical displacement profile for the highest reported experimental impulse is given below.

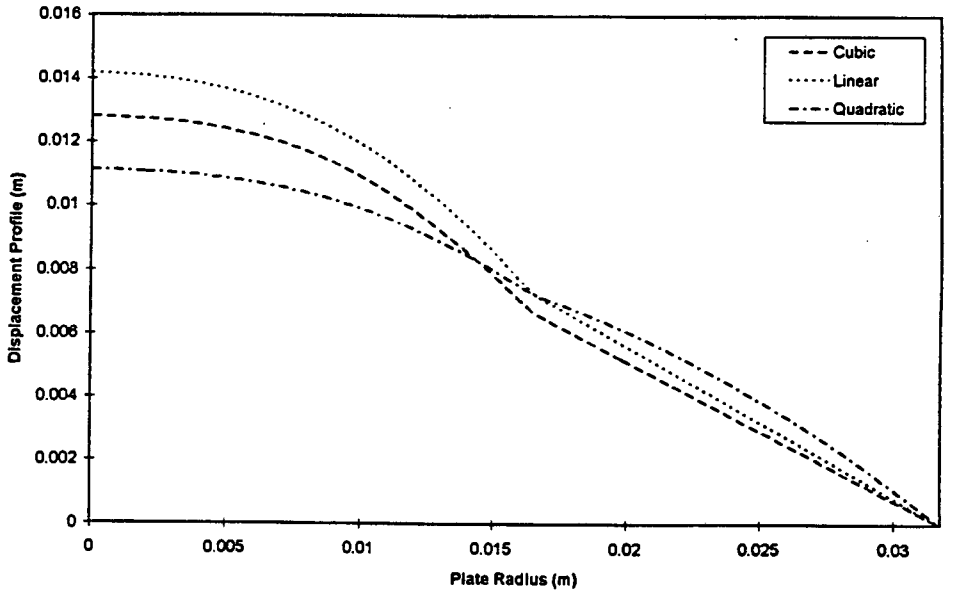

Figure 7.20 Comparison between experimental and theoretical displacement profiles for the cubic, quadratic and linear shape functions, **load to plate diameter ratio of 1/2** and **impulse** of **4.01Ns.**

7.2 THEORETICAL STRAIN

The experimental strain distribution through the plates was not determined. However uniaxial tensile strain at failure for the plate material was determined through uniaxial tensile tests. When for some impulse and load to plate diameter ratio a strain of equivalent magnitude to the uniaxial tensile strain occurs at a point in the plate, failure through tensile tearing will occur. It is an approximation to this impulse that is used in the theoretical strain model to calculate the theoretical strain distribution in the plate, and the maximum strain in this distribution and position of this maximum strain are compared to the uniaxial tensile strain and mean cap diameter respectively.

The impulse required to cause failure of the plates for each load diameter was not directly determined from experimentation. However, if the highest impulse recorded prior to plate failure and the lowest impulse recorded after plate failure, for

each load diameter, is plotted with a linear regression line (Eq. 7.1) through these points, the linear regression line will give an approximation to the impulse required to cause plate failure. This plot is shown in Figure 7.21.

Eq. 7.1 $\text{Impulse} = 144.27 \cdot (\text{Load Diameter}) + 6.1916$

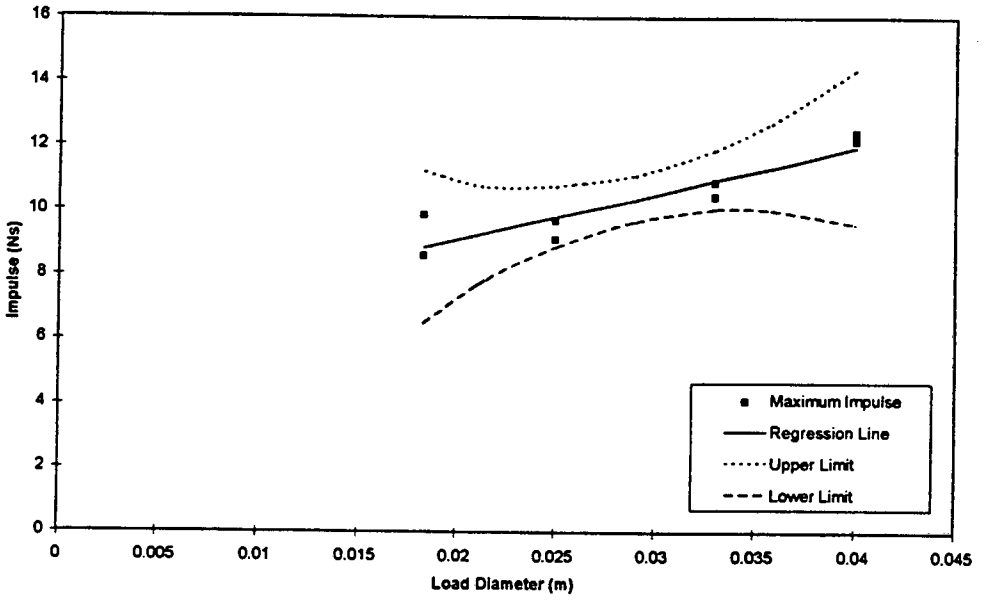

Figure 7.21 A plot of the maximum impulse prior to plate failure and minimum impulse after plate failure, with a linear regression line and 80% confidence limit shown.

The approximate impulses at plate failure, given by the linear regression line, for each load diameter are used to calculate the theoretical strain distributions in the plates, and the maximum strain in these distributions are compared to the uniaxial tensile strain for each shape function and load diameter. Furthermore, the diameters at which the maximum theoretical strains occur is assumed to be the point at which the plates will tear. These diameters are compared to the mean cap diameter for each shape function and load diameter. These comparisons are made in Figure 7.22 to Figure 7.25.

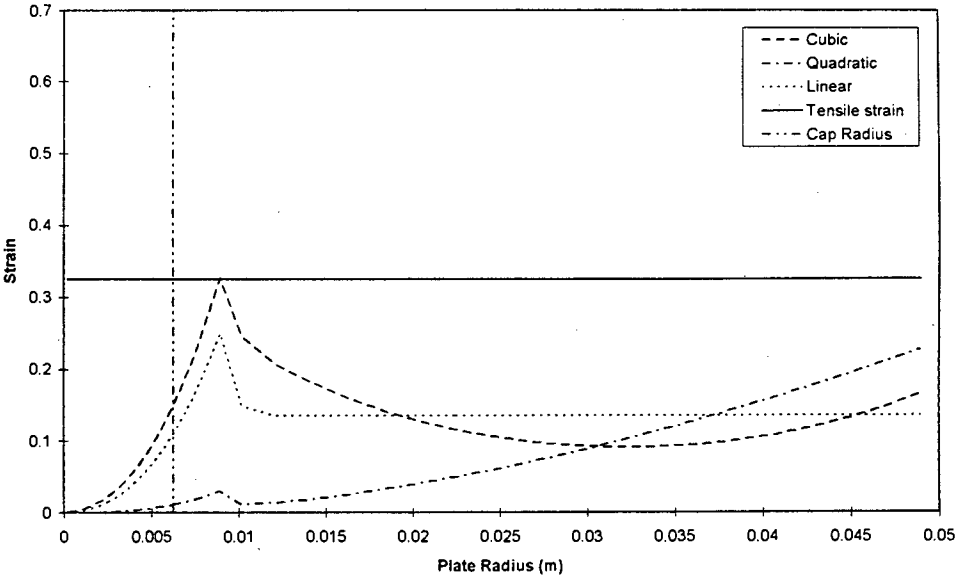

Figure 7.22 Theoretical strain distribution across the plate for each shape function, showing the uniaxial tensile strain and mean cap diameter, for a load diameter of 18.3mm.

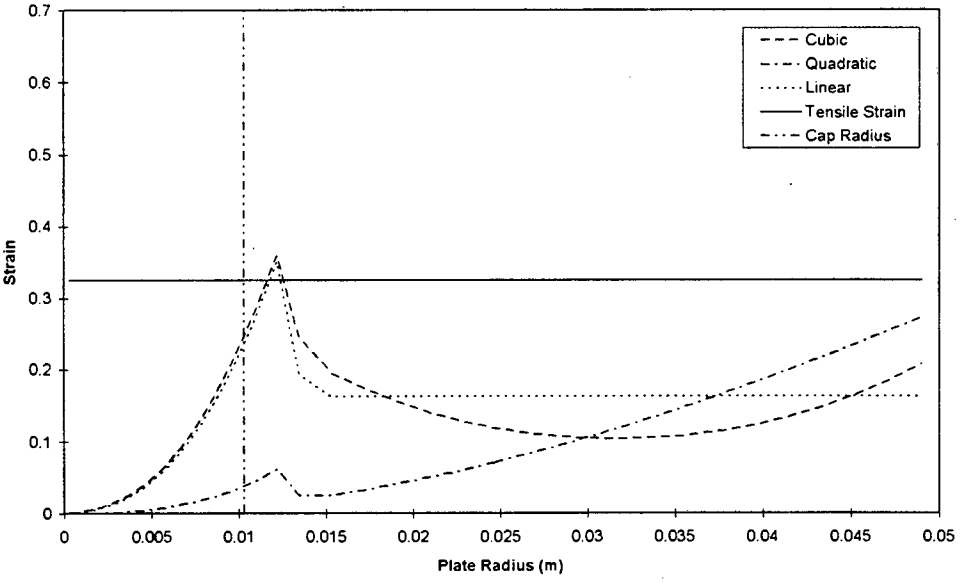

Figure 7.23 Theoretical strain distribution across the plate for each shape function, showing the uniaxial tensile strain and mean cap diameter, for a load diameter of 25mm.

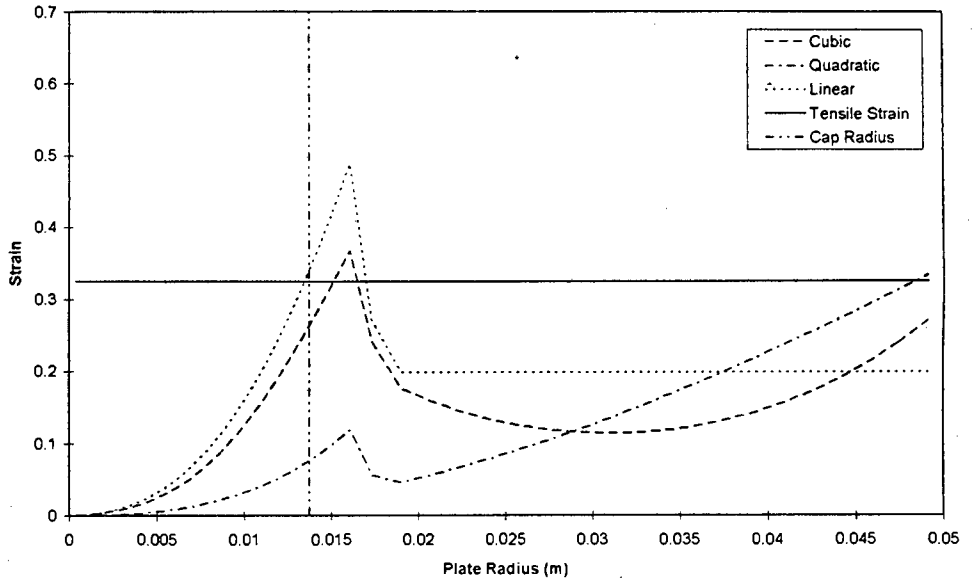

Figure 7.24 Theoretical strain distribution across the plate for each shape function, showing the uniaxial tensile strain and mean cap diameter, for a load diameter of 33mm.

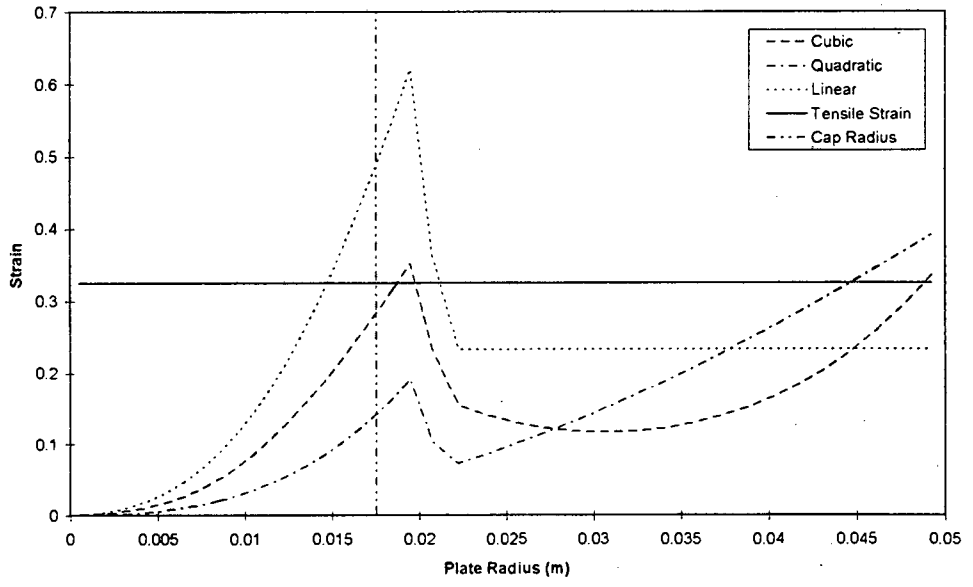

Figure 7.25 Theoretical strain distribution across the plate for each shape function, showing the uniaxial tensile strain and mean cap diameter, for a load diameter of 40mm.

7.3 FINITE ELEMENT DISPLACEMENT

For the smaller load diameters an impulse of 1Ns translates into a pressure over the load area in the order of 6 GPa. These high pressures resulted in numerical instabilities forming in the finite element solution and therefore, stable solutions using the finite element model were only obtained for low impulses. For the 18.3mm and 25mm load diameters these impulses were lower than the experimental impulses, and hence the finite element model predictions could not be compared to experimental data. However, as can be seen in Figure 7.26 to Figure 7.29, the finite element model is compared to the theoretical displacement model for displacement profiles only.

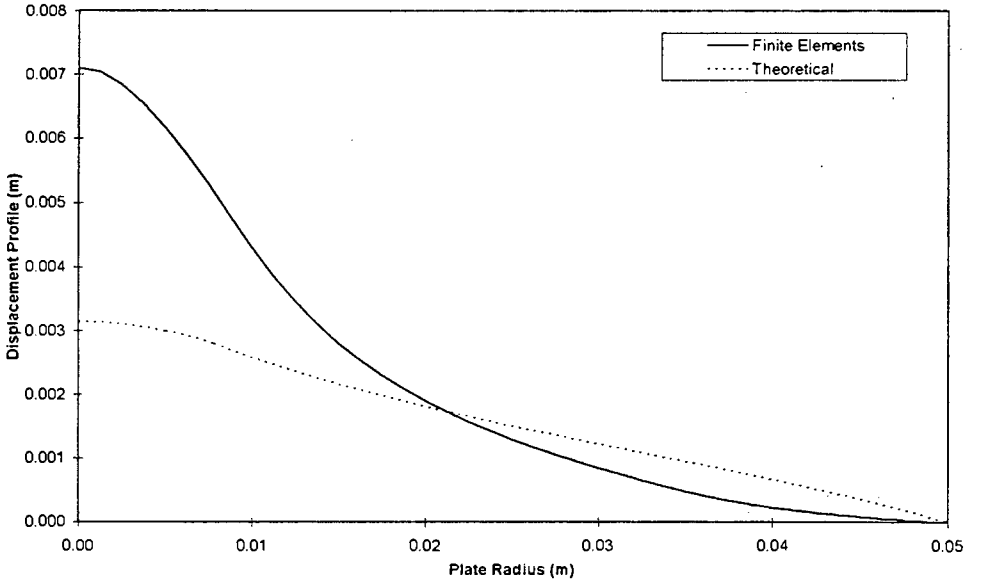

Figure 7.26 Comparison between the finite element and theoretical models using the cubic shape function for a load diameter of 18.3mm and impulse of 1Ns.

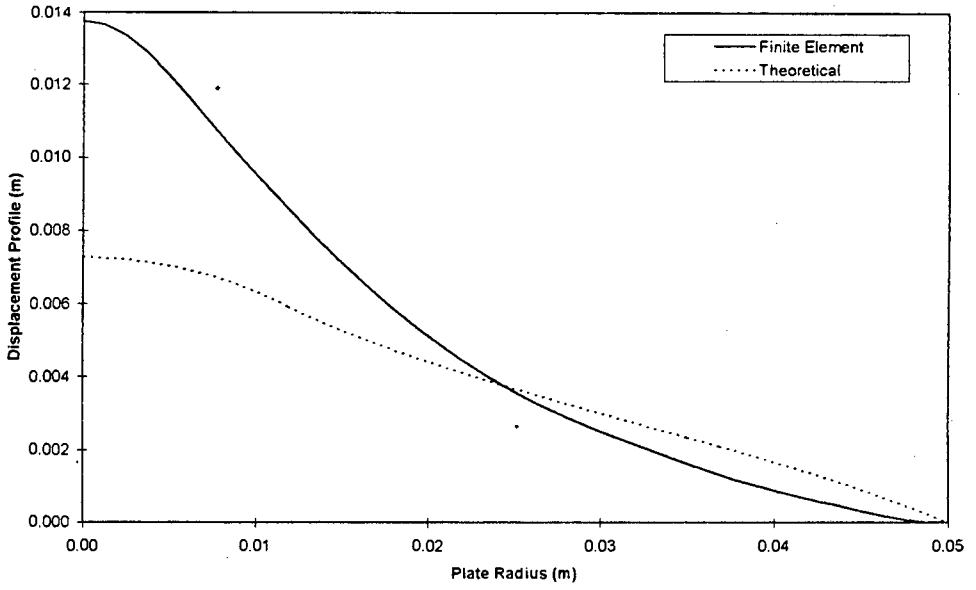

Figure 7.27 Comparison between the finite element and theoretical models using the cubic shape function for a load diameter of 25mm and impulse of 2.55 Ns.

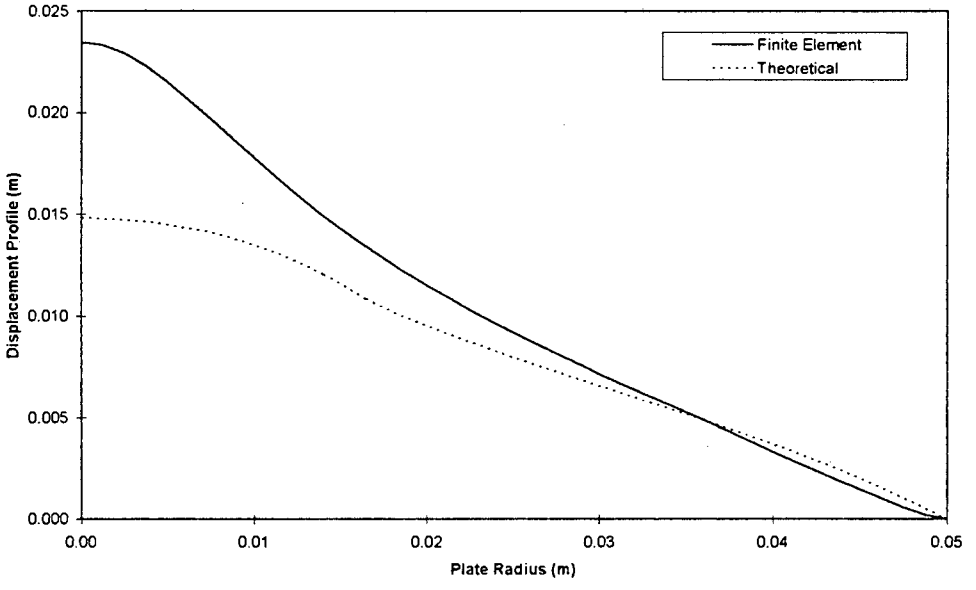

Figure 7.28 Comparison between the finite element and theoretical models using the cubic shape function for a load diameter of 33mm and impulse of 5.86 Ns.

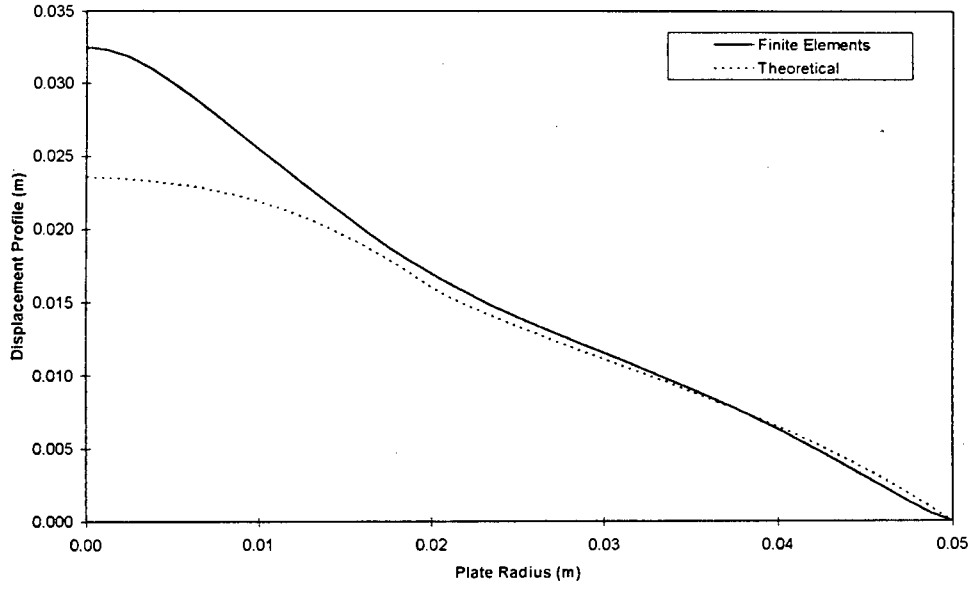

Figure 7.29 Comparison between the finite element and theoretical models using the cubic shape function for a load diameter of 40mm and impulse of 10.44 Ns.

8. DISCUSSION AND CONCLUSIONS

This document presents a theoretical model for predicting the mid-point displacements, displacement profiles of and strain in thin circular metal plates subjected to localised impulsive loads. The model developed is compared to experimental data with deformations up to and including plate tearing, as well as a finite element model.

The experimental data presented in this document was generated by the author as an undergraduate project. The experimental procedure described makes use of a ballistic pendulum to calculate the impulse applied to the plates by the explosive. This experimental technique has been used extensively and has proven to give consistent and reproducible results. The impulsive loads are applied to the plates by plastic explosive evenly spread and located centrally over the load diameter. Plate deflections for all load diameters gave favourable symmetry about the centre of the plates. Mid-point deflections and plate displacement profiles were measured from traces taken through the centre of the plates. Due to random irregularities at the cap diameters, several diameter readings were taken for each cap and a mean was used. A mean of all the cap diameters was used for each load diameter. A plot of the mean cap to plate diameter ratios versus the load to plate diameter ratios showed that over the experimental data range a linear regression line correlated well with the data.

The effects of 3 meshes on the theoretical displacement and strain models were investigated. Both the theoretical mid-point displacements and displacement profiles were found to be relatively mesh independent due to the method by which the initial velocity amplitude was calculated. However, the theoretical strain model was found to be more mesh dependent although satisfactory convergence of the solution was seen to occur for mesh 3. Considering these observations it was decided that mesh 3, consisting of both 20 discretised points evenly distributed from the centre of the plate to the load diameter and from the load diameter to plate diameter, would be

used when comparing the predictions made by the theoretical displacement and strain models with experimental data.

The theoretical displacement model using the three shape functions was compared to experimental data for both the mid-point displacements and displacement profiles. For the mid-point displacements the theoretical model using the linear shape function gave good predictions for the smaller load to plate diameter ratios, while the quadratic shape function gave better predictions for the larger load to plate diameter ratios. The cubic shape function however, gave more consistent predictions to the mid-point displacements across the experimental load to plate diameter ratio range, including those used by Bodner and Symonds [4]. For the theoretical plate displacement profiles the cubic shape function also gave better predictions to the experimental plate displacement profiles compared to those given by the quadratic and linear shape functions, for the load to plate diameter ratios investigated. Generally the theoretical displacement model using the cubic shape function gave good correlation with experimental data.

The maximum experimental impulse recorded prior to plate tearing and the minimum experimental impulse recorded after plate tearing for each load to plate diameter ratio was plotted with a regression line through the data. This line was taken to give a good approximation for the impulse required to cause the onset of plate tearing. Using these impulses, the theoretical strain model for each of the three shape functions was used to predict the strain in the plates for each load to plate diameter ratio. The magnitudes of the theoretical strains for each shape function and load to plate diameter ratios were compared to the quasistatic uniaxial tensile strain, and the position of their maximum compared to the respective mean cap diameters. The maximum magnitude of the theoretical strain using the cubic shape function gave good correlation with the uniaxial tensile strain in comparison to results given by the linear and quadratic shape functions, for all the load to plate diameter ratios. The positions of the maximum theoretical strains using the cubic and linear shape functions occurred at a diameter close to the cap diameter. However using the quadratic shape

function the maximum occurred at the plate diameter, for all the load to plate diameter ratios. It was also noted that the theoretical strain at the plate diameter for the cubic shape function increased with load diameter. This is consistent with the observations made, where thinning at the plate boundary was noted for the larger load diameters but not for the smaller load diameters. Generally a good correlation between the experimental data and the predictions made using the theoretical strain model and cubic shape function was obtained.

The finite element model proposed did not give satisfactory results. Loading the plates over the load area only, for relatively small impulses, resulted in high pressures that caused numerical instabilities in the finite element solution. The deflections around the centre of the plate obtained using the finite element model were higher than those predicted by the theoretical displacement model using the cubic shape function. This would indicate that the pressure applied by the explosive to the plate spreads beyond the load diameter.

9. RECOMMENDATIONS

The theoretical displacement and strain models presented in this document are only compared to experimentation covering localised impulsive loads for relatively small load to plate diameter ratios. Together with this the models do not take into account bending or plate thinning. Although the spread of the explosive pressure beyond the load diameter was modelled in the theoretical displacement model, no attempt was made to model this spread in the finite element model. Finally the load to plate diameter ratio at which tearing of the plate ceases at the cap diameter and starts at the plate boundary was not determined. All these topics of investigation were beyond the scope of this document and hence the following recommendations are made with reference to future work.

1. Comparisons between the theoretical displacement model and experimental work should be extended to cover a larger range of load to plate diameter ratios. This may entail developing new shape functions.

2. The theoretical displacement model should be extended to take into account bending effects and plate thinning.

3. The effect of the explosive pressure spreading beyond the load diameter should be incorporated into the finite element model. One method that could be used to incorporate this pressure spread is to adapt the velocity profiles used in the theoretical displacement model to pressure profiles.

4. The load to plate diameter ratio at which tearing at the cap diameter ceases and tearing at the plate boundary begins should be experimentally determined.

REFERENCES

1. G.N. Nurick and, J.B. Martin "*Deformation of Thin Plates Subjected to Impulsive Loading - A Review: Part I: Theoretical Considerations*" Int. J Impact Engng. Vol. 8. No 2. pp 159-170, 1989.

2. G.N. Nurick and, J.B. Martin "*Deformation of Thin Plates Subjected to Impulsive Loading - A Review: Part II: Experimental Studies*" Int. J Impact Engng. Vol 8. No 2. pp 171-186, 1989.

3. G.H. Farrow, G.N. Nurick and G.P. Mitchell, "*Modelling of impulsively loaded circular plates using the ABAQUS finite element code,*" Proceedings of the 13th Symposium on Finite Elements in South Africa, Vol. 1, 186-197, 18-20 January 1995

4. S.R. Bodner and P.S. Symonds, *"Experiments on Viscoplastic Response of Circular Plate to Impulsive Loads,"* J. Mech. Phys. Solids. Vol. 27 pp 91-113, 1989.

5. P.S. Symonds and T. Wierzbicki, *"Membrane Mode Solutions for Impulsively Loaded Circular Plates,"* J. Appl. Mech. March 1979, Vol. 46, pp 58-64.

6. A.L. Florence, *"Clamped Circular Rigid-Plastic Plates Under Central Blast Loading,"* Int. J. Solids Structures, 1966, Vol. 2, pp 319-335.

7. Dongquan Lui and W.J. Stronge, *"Shear and bending response of a Ridged-Plastic Plate to Partially Distributed Blast-Type Loading"* Euromech, 2nd European Solid Mechanics Conference, Genoa, September 12-16, 1994.

8. R.G. Teeling-Smith and G.N. Nurick, "*The Deformation and Tearing of Thin Circular Plates Subjected to Impulsive Loads*," Int. J. Impact Engng, Vol. 11, No 1, 77-91, 1991.

9. B.M. Thomas, "*The Effects of Boundary Conditions on the Failure of Thin Plates Subjected to Impulsive Loading.*" MSc Thesis, University of Cape Town, 1995

10. A. McClintock, Q. Zhou and T. Wierzbicki, "*Necking in Plane Strain Under Bending with Constant Tension,*" J. Mech. Phys. Solids Vol. 41, No. 8, 1327-1343, 1993.

11. T.A. Duffey (1989), "*Dynamic Rupture of Shells*" Structural Failure (T. Wierzbicki and N. Jones), 161-191

APPENDIX A

CUBIC SHAPE FUNCTION GROUP

For ϕ_R

$$A_R(R_b) = 1 - B_R(R_b)\cdot R_b - C_R(R_b)\cdot R_b^{\,2} - D_R(R_b)\cdot R_b^{\,3}$$

$$B_R(R_b) = \theta_{1R}(R_b) - 2\cdot C_R(R_b)\cdot R_b - 3\cdot D_R(R_b)\cdot R_b^{\,2}$$

$$C_R(R_b) = \frac{\theta_{2R}(R_b) - \theta_{1R}(R_b) - 3\cdot D_R(R_b)\cdot (R^2 - R_b^{\,2})}{2\cdot (R - R_b)}$$

$$D_R(R_b) = \frac{-\left(1+\theta_{1R}(R_b)\cdot (R-R_b) - R_b\cdot \left(\theta_{2R}(R_b) - \theta_{1R}(R_b)\right) + 1/2\cdot \left(\theta_{2R}(R_b) - \theta_{1R}(R_b)\right)\cdot (R+R_b)\right)}{3\cdot R_b\cdot \left(R^2 - R_b^2\right) - 3\cdot R_b^{\,2}\cdot (R-R_b) - 3/2\cdot \left(R^2 - R_b^2\right)\cdot (R+R_b) + \left(R^3 - R_b^3\right)}$$

For ϕ_L

$$A_L(R_b) = 1 - B_L(R_b)\cdot R_b - C_L(R_b)\cdot R_b^{\,2} - D_L(R_b)\cdot R_b^{\,3}$$

$$B_L(R_b) = \theta_{1L}(R_b) - 2\cdot C_L(R_b)\cdot R_b - 3\cdot D_L(R_b)\cdot R_b^{\,2}$$

$$C_L(R_b) = \frac{\theta_{2L}(R_b) - \theta_{1L}(R_b) - 3\cdot D_L(R_b)\cdot \left(R^2 - R_b^{\,2}\right)}{2\cdot \left(-R - R_b\right)}$$

$$D_L(R_b) = \frac{-\left(1+\theta_{1L}(R_b)\cdot (-R-R_b) - R_b\cdot \left(\theta_{2L}(R_b) - \theta_{1L}(R_b)\right) + 1/2\cdot \left(\theta_{2L}(R_b) - \theta_{1L}(R_b)\right)\cdot (-R+R_b)\right)}{3\cdot R_b\cdot \left(R^2 - R_b^2\right) - 3\cdot R_b^{\,2}\cdot (-R-R_b) - 3/2\cdot \left(R^2 - R_b^2\right)\cdot (-R+R_b) + \left(-R^3 - R_b^3\right)}$$

For ϕ_{RL}

$$A_{RL}(R_b) = 1 + B_{RL}(R_b) \cdot R_b - C_{RL}(R_b) \cdot R_b^{\,2} + D_{RL}(R_b) \cdot R_b^{\,3}$$

$$B_{RL}(R_b) = \theta_{1RL}(R_b) + 2 \cdot C_{RL}(R_b) \cdot R_b - 3 \cdot D_{RL}(R_b) \cdot R_b^{\,2}$$

$$C_{RL}(R_b) = \frac{\theta_{2RL}(R_b) - \theta_{1RL}(R_b) - 3 \cdot D_{RL}(R_b) \cdot \left(R^2 - R_b^{\,2}\right)}{2 \cdot (R + R_b)}$$

$$D_{RL}(R_b) = \frac{-\left(1 + \theta_{1RL}(R_b) \cdot (R + R_b) + R_b \cdot \left(\theta_{2RL}(R_b) - \theta_{1RL}(R_b)\right) + 1/2 \cdot \left(\theta_{2RL}(R_b) - \theta_{1RL}(R_b)\right) \cdot (R - R_b)\right)}{-3 \cdot R_b \cdot \left(R^2 - R_b^2\right) - 3 \cdot R_b^2 \cdot (R + R_b) - 3/2 \cdot \left(R^2 - R_b^2\right) \cdot (R - R_b) + \left(R^3 + R_b^3\right)}$$

QUADRATIC SHAPE FUNCTION GROUP

For ϕ_R

$$A_R(R_b) = 1 + C_R(R_b) \cdot R_b^{\,2}$$

$$B_R(R_b) = -2 \cdot C_R(R_b) \cdot R_b$$

$$C_R(R_b) = \frac{-1}{R_b^{\,2} - 2 \cdot R_b \cdot R + R^2}$$

$$D_R(R_b) = 0$$

For ϕ_L

$$A_L(R_b) = 1 + C_L(R_b) \cdot R_b^{\,2}$$

$$B_L(R_b) = -2 \cdot C_L(R_b) \cdot R_b$$

$$C_L(R_b) = \frac{-1}{R_b^{\,2} + 2 \cdot R_b \cdot R + R^2}$$

$$D_L(R_b) = 0$$

For ϕ_{RL}

$$A_{RL}(R_b) = 1 + C_{RL}(R_b) \cdot R_b^{\,2}$$

$$B_{RL}(R_b) = 2 \cdot C_{RL}(R_b) \cdot R_b$$

$$C_{RL}(R_b) = \frac{-1}{R_b^{\,2} + 2 \cdot R_b \cdot R + R^2}$$

$$D_{RL}(R_b) = 0$$

LINEAR SHAPE FUNCTION GROUP

For ϕ_R

$$A_R(R_b) = -B_R(R_b) \cdot R$$

$$B_R(R_b) = \frac{1}{R_b - R}$$

$$C_R(R_b) = 0$$

$$D_R(R_b) = 0$$

For ϕ_L

$$A_L(R_b) = B_L(R_b) \cdot R$$

$$B_L(R_b) = \frac{1}{R_b + R}$$

$$C_L(R_b) = 0$$

$$D_L(R_b) = 0$$

For ϕ_{RL}

$$A_{RL}(R_b) = -B_{RL}(R_b) \cdot R$$

$$B_{RL}(R_b) = \frac{-1}{R_b + R}$$

$$C_{RL}(R_b) = 0$$

$$D_{RL}(R_b) = 0$$

APPENDIX B

Total Displacement For $r = 0$,

$$W_T(0) = \frac{\left(W_L(0,0) + W_{RL}(0,0)\right) + \left(W_R(0,0) + W_{RL}(0,0)\right)}{2} + \left(W_L(0,r1) + W_{RL}(0,r1)\right) + \left(W_L(0,r2) + W_{RL}(0,r2)\right) + \left(W_L(0,R_0) + W_{RL}(0,R_0)\right)$$

Total Displacement For $r = r1$,

$$W_T(r1) = \left(W_R(r1,0) + W_{RL}(r1,0)\right) + \frac{\left(W_L(r1,r1) + W_{RL}(r1,r1)\right) + \left(W_R(r1,r1) + W_{RL}(r1,r1)\right)}{2} + \left(W_L(r1,r2) + W_{RL}(r1,r2)\right) + \left(W_L(r1,R_0) + W_{RL}(r1,R_0)\right)$$

Total Displacement For $r = r2$,

$$W_T(r2) = \left(W_R(r2,0) + W_{RL}(r2,0)\right) + \left(W_R(r2,r1) + W_{RL}(r2,r1)\right) + \frac{\left(W_L(r2,r2) + W_{RL}(r2,r2)\right) + \left(W_R(r2,r2) + W_{RL}(r2,r2)\right)}{2} + \left(W_L(r2,R_0) + W_{RL}(r2,R_0)\right)$$

Total Displacement For $r = R_0$,

$$W_T(R_0) = \left(W_R(R_0,0) + W_{RL}(R_0,0)\right) + \left(W_R(R_0,r1) + W_{RL}(R_0,r1)\right) + \left(W_R(R_0,r2) + W_{RL}(R_0,r2)\right) + \frac{\left(W_L(R_0,R_0) + W_{RL}(R_0,R_0)\right) + \left(W_R(R_0,R_0) + W_{RL}(R_0,R_0)\right)}{2}$$

Total Displacement For $r = r3$,

$$W_T(r3) = \left(W_R(r3,0) + W_{RL}(r3,0)\right) + \left(W_R(r3,r1) + W_{RL}(r3,r1)\right) + \left(W_R(r3,r2) + W_{RL}(r3,r2)\right) + \left(W_R(r3,R_0) + W_{RL}(r3,R_0)\right)$$

Total Displacement For $r = R$,

$$W_T(R) = 0$$

The total displacements at *0*, *r1*, *r2*, R_0, *r3* and *R*, given by the above equations, are illustrated in Figure B.1.

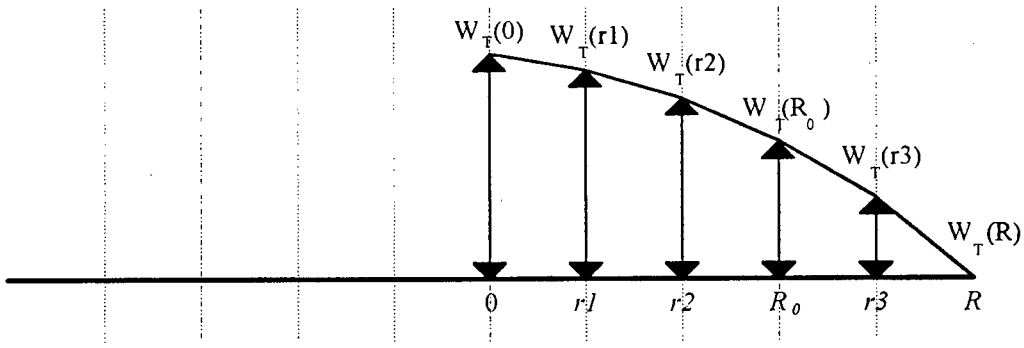

Figure B.1 Total displacements.

APPENDIX C

The linearized equations of motion of the pendulum assuming viscous damping are,

Eq. C.1 $$\ddot{X} + 2 \cdot \beta \cdot \dot{X} + W_n^2 \cdot X = 0$$

where

$$\beta = \frac{C}{2 \cdot M},\ \omega_n = \frac{2 \cdot \pi}{T} \text{ and } \omega_d = \left(\omega_n^2 - \beta^2\right)^{1/2}$$

and C is the damping coefficient, M is the total mass of the pendulum including the test rig, I-beam and balancing mass, and T is the natural period of the pendulum.

The solution of Eq. C.1 is given by

Eq. C.2 $$X = \frac{e^{-\beta \cdot t} \cdot \dot{x}_0 \cdot \sin \omega_d \cdot t}{\omega_d}$$

where $\dot{x}_0$ is the initial velocity of the pendulum.

Let x_1 be the horizontal displacement at $t = \frac{T}{4}$ and $-x_2$ be the horizontal displacement at $t = \frac{3 \cdot T}{4}$.

Substituting into Eq. C.2 gives

Eq. C.3 $$x_1 = \frac{\dot{x}_0 \cdot T}{2 \cdot \pi} \cdot e^{-1/4 \cdot \beta \cdot T}$$

Eq. C.4 $$x_1 = \frac{\dot{x}_0 \cdot T}{2 \cdot \pi} \cdot e^{-3/4 \cdot \beta \cdot T}$$

Hence

Eq. C.5 $$\frac{x_1}{x_2} = e^{1/2 \cdot \beta \cdot T}$$

which gives

Eq. C.6 $$\beta = \frac{2}{T} \cdot \ln \frac{x_1}{x_2}$$

and

Eq. C.7 $$\dot{x}_0 = \frac{2 \cdot \pi}{T} \cdot x_1 \cdot e^{1/4 \cdot \beta \cdot T}$$

The impulse can therefore be found from

Eq. C.8 $$I = M \cdot \dot{x}_0$$

The period T was determined from averaging several measured pendulum oscillations. The damping constant β is found from Eq. C.6 where x_1 and x_2 are found from measurements taken from several pendulum motions in which the pendulum was drawn back and released.

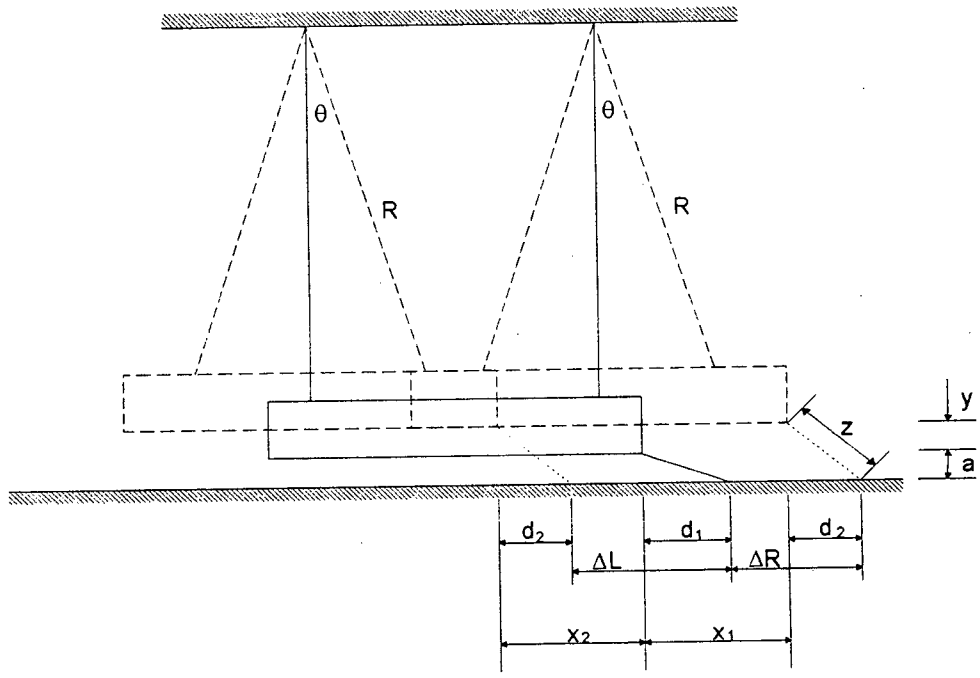

Figure C.1 Ballistic pendulum geometry.

It is noted from the pendulum geometry (Figure C.1) that the distance moved by the pendulum x_1 and that moved by the pendulum ΔR is not the same, and this must be accounted for. Considering Figure C.1 it is noted that when the pendulum is stationary the horizontal distance from the end of the pendulum to the pen is given by

Eq. C.9 $$d_1 = \left(Z^2 - a^2\right)^{1/2}$$

while at peak oscillation this distance decreases and is given by

Eq. C.10 $$d_2 = \left(Z^2 - (a+y)^2\right)^{1/2}$$

The small oscillations of the pendulum during testing ensured that θ is very small and therefore the assumption can be made that

$$x_1 = R \cdot \theta \text{ and } y = \frac{R \cdot \theta^2}{2}$$

Therefore

Eq. C.11 $$y = \frac{x_1^{\,2}}{2 \cdot R}$$

and

Eq. C.12 $$d_2 = \left(Z^2 - \left(a + \frac{x_1^{\,2}}{2 \cdot R} \right)^2 \right)^{1/2}$$

From Figure C.1

$$x_1 = \Delta R + d_1 - d_2$$

and

$$x_2 = \Delta L - d_1 + d_2$$

Substituting for d_1 and d_2 gives

Eq. C.13 $$x_1 = \Delta R + \left(Z^2 - a^2 \right)^{1/2} - \left(Z^2 - \left(a + \frac{x_1^{\,2}}{2 \cdot R} \right)^2 \right)^{1/2}$$

and

Eq. C.14 $$x_2 = \Delta L - \left(Z^2 - a^2 \right)^{1/2} + \left(Z^2 - \left(a + \frac{x_1^{\,2}}{2 \cdot R} \right)^2 \right)^{1/2}$$

ΔL, ΔR, Z, a and R are measured and therefore x_1 and x_2 can be calculated.

APPENDIX D

Test No.	Strain Rate 1/s	σ_0 MPa	% Strain at Failure
1	7.05e-4	202.6	33.2
2	7.05e-4	201.8	32.4
3	7.06e-3	200.6	33.1
4	7.06e-3	198.5	32.9
5	3.53e-2	176.7	32.3
6	3.53e-2	184.4	31.9
7	1.41e-2	186.8	31.5
8	1.4e-2	191.7	33.26
	Average	193.5	32.5

Table D.1 Uniaxial tensile test data.

APPENDIX E

LOAD DIAMETER 18.3mm.

Test No.	2010920118	2010920218	2010920318	2010920418	2010920518	2010920618	2010920718
Impulse (Ns)	4.03	4.14	4.59	4.79	5.71	6.03	6.13
Radius (m)	Displacements (m)						
0	0.0106	0.011	0.0133	0.0143	0.0161	0.016	0.0171
0.0025	0.0105	0.0106	0.0131	0.014	0.016	0.0159	0.017
0.005	0.0099	0.01	0.0123	0.0131	0.0149	0.0153	0.0159
0.0075	0.009	0.0092	0.0111	0.0121	0.0131	0.014	0.0145
0.01	0.008	0.0081	0.01	0.0109	0.0118	0.0125	0.0129
0.0125	0.007	0.0071	0.0089	0.0096	0.0105	0.011	0.0114
0.015	0.006	0.0061	0.0077	0.0087	0.0094	0.01	0.0099
0.0175	0.0051	0.0055	0.0067	0.0075	0.0083	0.0089	0.009
0.02	0.0045	0.0048	0.0058	0.0069	0.0073	0.008	0.0079
0.0225	0.004	0.004	0.005	0.0059	0.0066	0.007	0.0071
0.025	0.0034	0.0036	0.0045	0.0051	0.006	0.0061	0.0064
0.0275	0.003	0.0031	0.004	0.0047	0.0051	0.0055	0.0059
0.03	0.0025	0.0029	0.0033	0.004	0.0048	0.0049	0.0051
0.0325	0.0021	0.0024	0.003	0.0037	0.0041	0.0041	0.0048
0.035	0.0017	0.002	0.0025	0.003	0.0037	0.0036	0.004
0.0375	0.0015	0.0016	0.002	0.0024	0.0029	0.0029	0.0033
0.04	0.0011	0.0011	0.0014	0.0019	0.0022	0.0021	0.0029
0.0425	0.0009	0.0009	0.001	0.0013	0.0019	0.0016	0.0021
0.045	0.0005	0.0005	0.0007	0.0009	0.0011	0.0011	0.0014
0.0475	0.0001	0.0002	0.0003	0.0004	0.0009	0.0004	0.0009
0.05	0	0	0	0	0	0	0

2010920818	2010920918	2310920118	2310920218	2310920418	2310920518	2310920918	2310921018
7.74	7.51	8.16	7.89	8.29	8.04	9.38	9.85
0.0191	0.0178	0.0194	0.021	0.0202	0.0192	0.0175	0.0219
0.019	0.0175	0.0191	0.0207	0.02	0.0189	0.0169	0.0218
0.018	0.0161	0.018	0.0194	0.0189	0.0175	0.0156	0.021
0.0169	0.015	0.0161	0.0176	0.017	0.0159	0.0145	0.019
0.0149	0.0132	0.014	0.0153	0.015	0.014	0.0131	0.0171
0.0132	0.012	0.0126	0.0133	0.0132	0.0129	0.012	0.0152
0.012	0.0108	0.0111	0.012	0.012	0.0118	0.011	0.0139
0.0108	0.0097	0.0101	0.0107	0.011	0.0106	0.01	0.0122
0.0099	0.0086	0.0093	0.0095	0.01	0.0096	0.0094	0.0111
0.0088	0.008	0.0082	0.0086	0.009	0.009	0.009	0.0101
0.008	0.007	0.0076	0.008	0.0083	0.0084	0.0084	0.0093
0.0071	0.0063	0.0068	0.007	0.0078	0.0076	0.0078	0.0085
0.0063	0.0058	0.006	0.0063	0.0069	0.007	0.007	0.0078
0.0056	0.005	0.0053	0.0056	0.006	0.0061	0.0063	0.007
0.0048	0.0042	0.0044	0.0048	0.0052	0.0054	0.0057	0.006
0.0039	0.0033	0.0039	0.0039	0.0043	0.0045	0.0047	0.005
0.0029	0.0026	0.0029	0.003	0.0036	0.0037	0.0039	0.0041
0.002	0.002	0.002	0.002	0.0029	0.0028	0.003	0.0031
0.0011	0.0013	0.0011	0.0012	0.0019	0.0019	0.0019	0.002
0.0004	0.0008	0.0008	0.0007	0.0011	0.0013	0.001	0.0012
0	0	0	0	0	0	0	0

Table E.1 Experimental plate deflection data for a load diameter of 18.3mm.

LOAD DIAMETER 25mm.

Test No.	10109220625	1010920725	1010920825	1010920925	1010921025	1010921125	1010921225
Impulse (Ns)	5.94	5.19	3.9	7.68	7.7	8.45	9.1
Radius (m)	Displacements (m)						
0	0.0161	0.014	0.0097	0.0198	0.0232	0.022	0.0229
0.0025	0.0161	0.014	0.0097	0.0194	0.0231	0.022	0.0228
0.005	0.0158	0.0136	0.0092	0.0184	0.0221	0.0212	0.022
0.0075	0.0148	0.0129	0.0087	0.017	0.021	0.02	0.0209
0.01	0.0133	0.0118	0.0079	0.0154	0.0189	0.0179	0.0186
0.0125	0.012	0.0106	0.007	0.0139	0.0169	0.0162	0.0167
0.015	0.0108	0.0094	0.006	0.0124	0.015	0.0145	0.015
0.0175	0.01	0.0083	0.0053	0.0113	0.0139	0.013	0.0135
0.02	0.0089	0.0074	0.0046	0.0104	0.0128	0.0118	0.0123
0.0225	0.008	0.0066	0.004	0.0094	0.0117	0.0105	0.0111
0.025	0.007	0.0059	0.0036	0.0086	0.0107	0.0098	0.0102
0.0275	0.0063	0.0051	0.003	0.0079	0.0098	0.0088	0.0091
0.03	0.00569	0.0045	0.0028	0.007	0.0089	0.0078	0.0082
0.0325	0.005	0.004	0.0025	0.0063	0.008	0.007	0.0073
0.035	0.0045	0.0033	0.002	0.0054	0.007	0.0062	0.0064
0.0375	0.0038	0.0029	0.0018	0.0046	0.006	0.0052	0.0053
0.04	0.003	0.0021	0.0015	0.0038	0.0051	0.0042	0.0041
0.0425	0.002	0.0017	0.0011	0.0028	0.004	0.0035	0.003
0.045	0.00163	0.0011	0.0009	0.0019	0.003	0.0022	0.0019
0.0475	0.0008	0.0006	0.0007	0.001	0.0019	0.0012	0.0009
0.05	0	0	0	0	0	0	0

6.608 7.790
0,01984 0,02434

Table E.2 Experimental plate deflection data for a load diameter of 25mm.

LOAD DIAMETER 33mm.

Test No.	0510920133	0510920233	0510920333	0510920433	0510920533	0510920633
Impulse (Ns)	2.73	4.21	5.18	5.63	6.94	8.02
Radius (m)	Displacements (m)					
0	0.0055	0.011	0.014	0.013	0.018	0.021
0.0025	0.005	0.0108	0.0138	0.0129	0.018	0.021
0.005	0.0045	0.0102	0.0131	0.012	0.0175	0.0204
0.0075	0.004	0.0097	0.0123	0.0113	0.0168	0.0193
0.01	0.0033	0.0088	0.0111	0.0102	0.0155	0.018
0.0125	0.0029	0.0079	0.0102	0.0094	0.0142	0.0164
0.015	0.0025	0.007	0.0092	0.0086	0.013	0.0146
0.0175	0.002	0.0063	0.0083	0.008	0.0119	0.0134
0.02	0.0019	0.0056	0.0076	0.0072	0.0108	0.0122
0.0225	0.0016	0.0049	0.0068	0.0065	0.0099	0.0113
0.025	0.0015	0.0043	0.006	0.006	0.009	0.0104
0.0275	0.0012	0.004	0.0054	0.0053	0.0081	0.0095
0.03	0.001	0.0035	0.0049	0.0049	0.0073	0.0087
0.0325	0.0009	0.003	0.0042	0.004	0.0066	0.0079
0.035	0.00085	0.0028	0.0039	0.0036	0.0057	0.0069
0.0375	0.0007	0.0021	0.0032	0.003	0.0047	0.0058
0.04	0.0005	0.0019	0.0029	0.0026	0.0038	0.0046
0.0425	0.0003	0.0014	0.0021	0.0019	0.0026	0.0034
0.045	0.0002	0.001	0.0016	0.0011	0.0018	0.002
0.0475	0.0001	0.0008	0.0008	0.0007	0.0009	0.001
0.05	0	0	0	0	0	0

0510920733	0510920833	0510920933
9.18	9.73	10.88
0.024	0.0261	0.0289
0.0239	0.026	0.0285
0.0229	0.0253	0.0278
0.022	0.024	0.0265
0.0201	0.022	0.0248
0.0185	0.02	0.0222
0.0166	0.0179	0.0198
0.015	0.0162	0.0182
0.0139	0.015	0.0168
0.0128	0.0139	0.0155
0.0119	0.0129	0.0143
0.011	0.0118	0.0133
0.01	0.0107	0.0124
0.009	0.0095	0.0113
0.0079	0.0082	0.01
0.0068	0.007	0.0085
0.0054	0.0057	0.007
0.0041	0.0042	0.0053
0.0027	0.0027	0.0035
0.0013	0.001	0.0018
0	0	0

Table E.3 Experimental plate deflection data for a load diameter of 33mm.

LOAD DIAMETER 40mm.

Test No.	2910920140	2910920240	2910920340	2910920440	2910920540	2910920640
Impulse (Ns)	8.04	5.51	3.33	8.87	9.57	10.89
Radius (m)	Displacements (m)					
0	0.017	0.0128	0.0088	0.0209	0.0242	0.0262
0.0025	0.0169	0.0128	0.0086	0.0206	0.024	0.026
0.005	0.0168	0.0126	0.0084	0.0202	0.0233	0.0256
0.0075	0.0165	0.0121	0.008	0.0195	0.0222	0.0248
0.01	0.0159	0.0113	0.0074	0.0185	0.0207	0.0232
0.0125	0.015	0.0106	0.0068	0.0171	0.019	0.0218
0.015	0.014	0.0096	0.006	0.0159	0.0177	0.0199
0.0175	0.0129	0.0088	0.0053	0.0145	0.0162	0.018
0.02	0.0118	0.0079	0.0047	0.0135	0.015	0.0169
0.0225	0.0108	0.007	0.004	0.0124	0.014	0.0158
0.025	0.01	0.0062	0.0035	0.0116	0.0132	0.0149
0.0275	0.0093	0.0054	0.003	0.0107	0.0122	0.0138
0.03	0.0084	0.005	0.0025	0.01	0.0114	0.0129
0.0325	0.0077	0.0042	0.002	0.009	0.0103	0.0118
0.035	0.0068	0.0038	0.0015	0.008	0.0092	0.0103
0.0375	0.0059	0.0029	0.0013	0.0068	0.008	0.009
0.04	0.0048	0.002	0.0009	0.0058	0.0068	0.0074
0.0425	0.0038	0.0013	0.0005	0.0043	0.0052	0.0058
0.045	0.0024	0.0006	0.0002	0.0031	0.0036	0.0037
0.0475	0.0015	0.0001	0.00005	0.0018	0.002	0.0021
0.05	0	0	0	0	0	0

2910920740	2910920840	2910920940	2910921440
11.29	12.35	12.41	11.98
0.0265	0.0275	0.0284	0.025
0.02625	0.0275	0.0282	0.025
0.0258	0.0272	0.028	0.0246
0.025	0.0269	0.027	0.0239
0.0235	0.026	0.0257	0.0224
0.022	0.0244	0.024	0.0212
0.02	0.0228	0.022	0.0198
0.0186	0.021	0.02	0.0181
0.0172	0.0192	0.0185	0.017
0.016	0.0177	0.0171	0.0159
0.015	0.0166	0.016	0.015
0.014	0.0152	0.015	0.014
0.013	0.014	0.014	0.0132
0.012	0.0129	0.013	0.0122
0.0109	0.0115	0.0116	0.0109
0.0094	0.01	0.01	0.0091
0.0078	0.0081	0.0084	0.0075
0.0061	0.0063	0.0069	0.0059
0.0043	0.0043	0.0051	0.0037
0.0025	0.0023	0.0032	0.0019
0	0	0	0

Table E.4 Experimental plate deflection data for a load diameter of 40mm.

APPENDIX F

LOAD DIAMETER 18.3mm.

Test No.	Impulse (Ns)	Cap Diameter (mm)
2310920318	8.57	12.4
2310920618	8.81	12.4
2310920718	9.22	12
2310920818	9.41	13
Mean Cap Diameter		12.5

Table F.1 Experimental cap diameter data for a load diameter of 18.3mm.

LOAD DIAMETER 25mm.

Test No.	Impulse (Ns)	Cap Diameter (mm)
1010921325	9.76	19.8
1210920125	9.68	19.1
1210920225	11.20	19.4
1210920325	11.67	21.5
1210920425	13.87	21
1210920525	14.34	22
1210920625	13.93	21.9
1210920725	10.75	20.4
1210920825	11.52	19.9
Mean Cap Diameter		20.6

Table F.2 Experimental cap diameter data for a load diameter of 25mm.

LOAD DIAMETER 33mm.

Test No.	Impulse (Ns)	Cap Diameter (mm)
0510921033	11.40	26.5
0510921133	11.37	26.5
0510921233	10.43	27.3
0610920133	13.00	27.2
0610920233	14.96	28.3
0610920333	16.03	28.1
0610920433	13.67	28.4
Mean Cap Diameter		27.5

Table F.3 Experimental cap diameter data for a load diameter of 33mm.

LOAD DIAMETER 40mm.

Test No.	Impulse (Ns)	Cap Diameter (mm)
2910921140	14.01	32.3
2910921240	14.34	36.1
2910921340	14.94	36.8
Mean Cap Diameter		35.1

Table F.4 Experimental cap diameter data for a load diameter of 40mm.

APPENDIX G

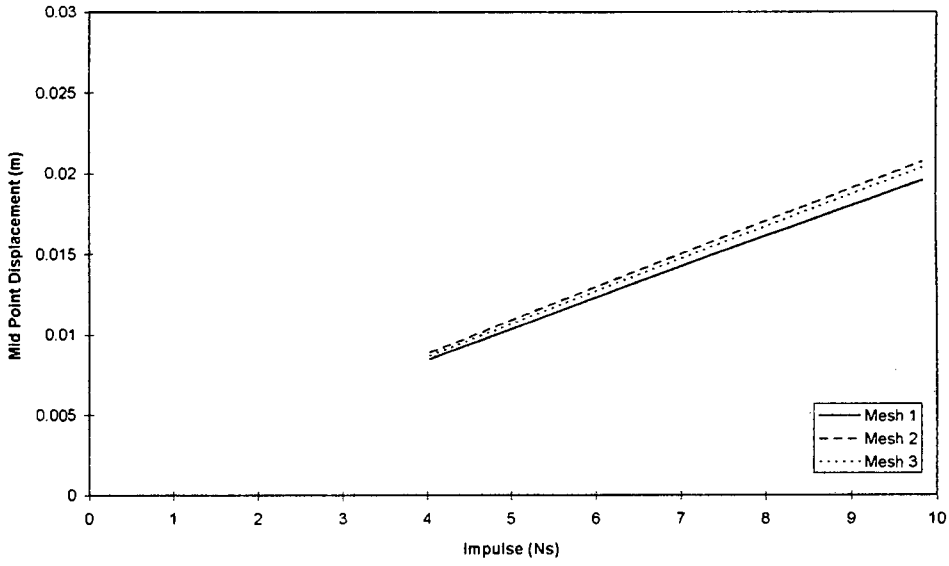

Figure G.1 Theoretical mid-point displacement for the **quadratic shape function** and **load, plate diameter** of **18.3mm** and **100mm** respectively, using the three meshes.

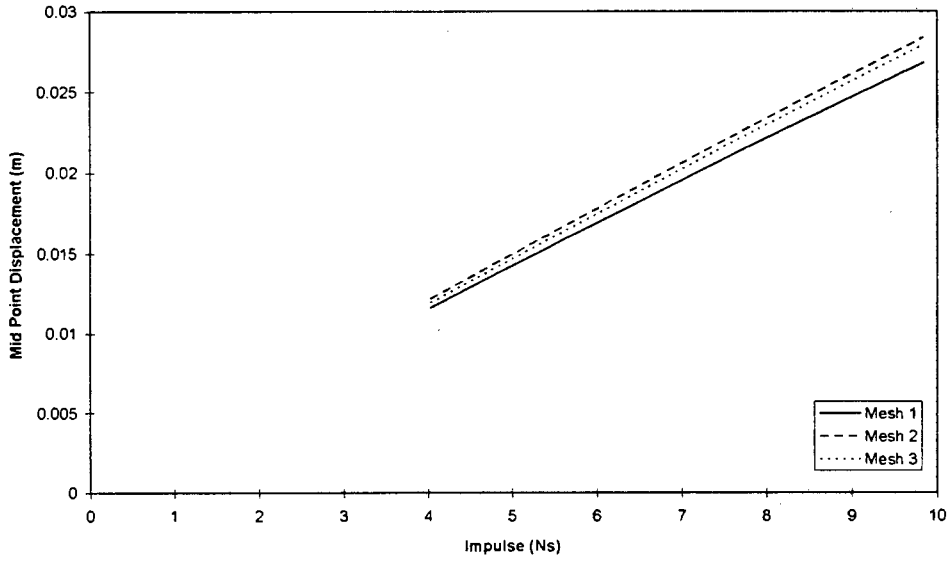

Figure G.2 Theoretical mid-point displacement for the **Linear shape function** and **load, plate diameter** of **18.3mm** and **100mm** respectively, using the three meshes.

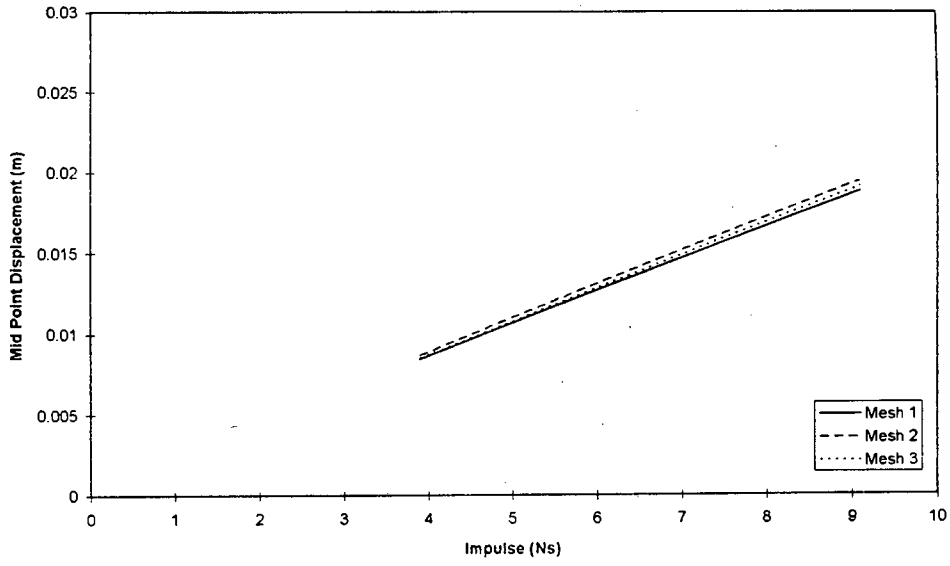

Figure G.3 Theoretical mid-point displacement for the **quadratic shape function** and **load, plate diameter** of **25mm** and **100mm** respectively, using the three meshes.

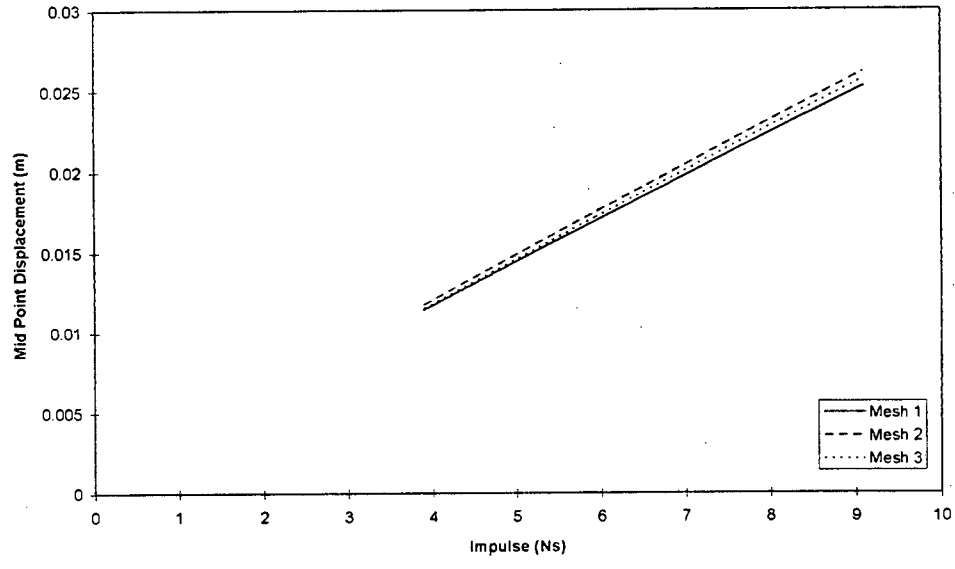

Figure G.4 Theoretical mid-point displacement for the **linear shape function** and **load, plate diameter** of **25mm** and **100mm** respectively, using the three meshes.

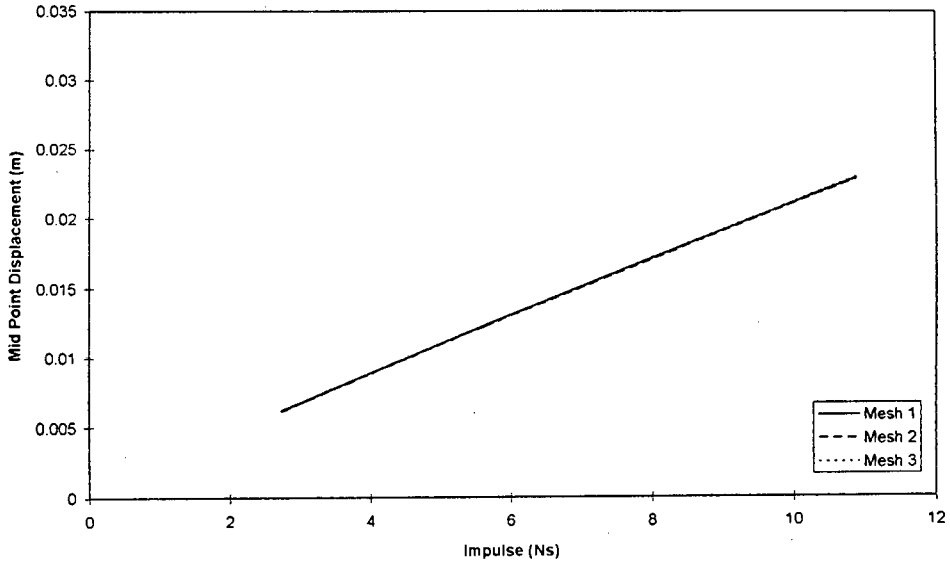

Figure G.5 Theoretical mid-point displacement for the **quadratic shape function** and **load, plate diameter** of **33mm** and **100mm** respectively, using the three meshes.

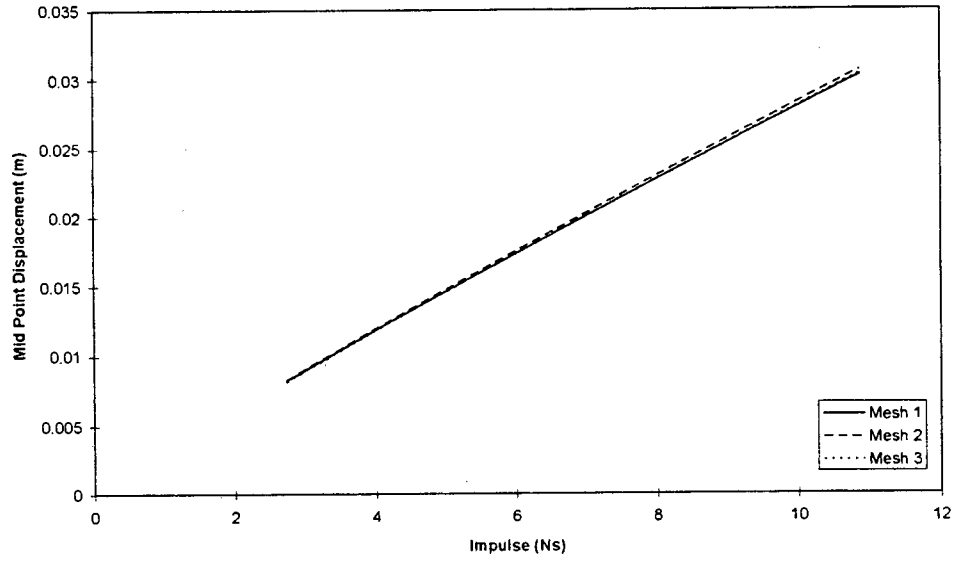

Figure G.6 Theoretical mid-point displacement for the **linear shape function** and **load, plate diameter** of **33mm** and **100mm** respectively, using the three meshes.

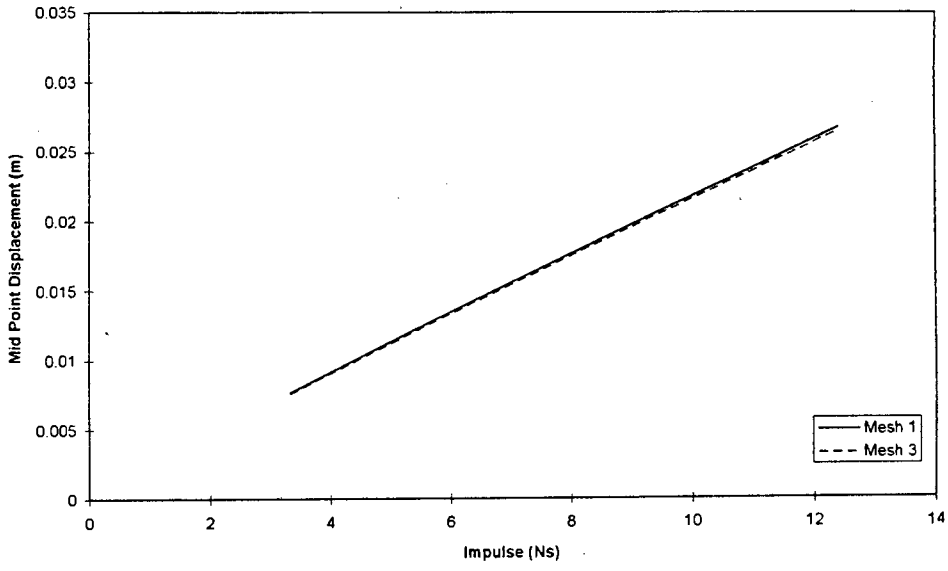

Figure G.7 Theoretical mid-point displacement for the **quadratic shape function** and **load, plate diameter** of **40mm** and **100mm** respectively, using the three meshes.

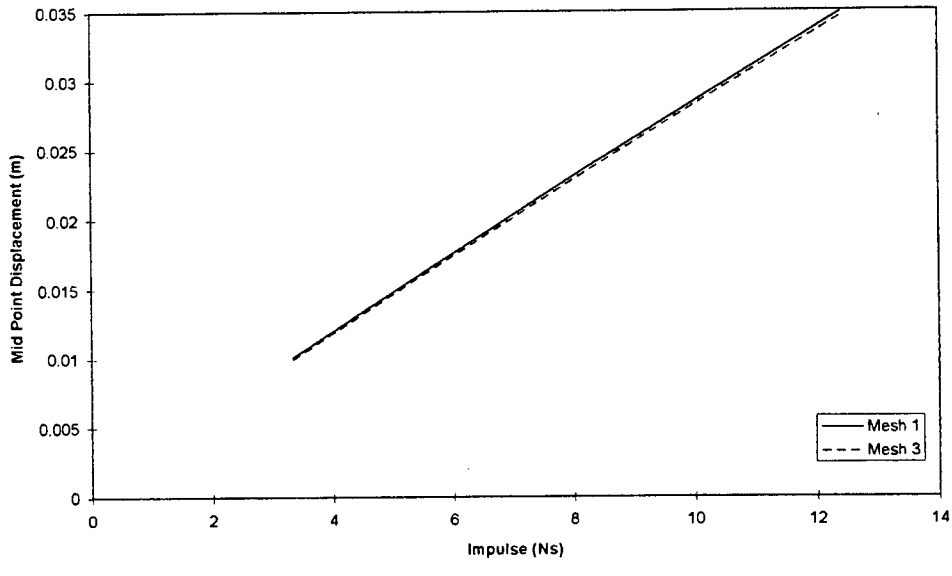

Figure G.8 Theoretical mid-point displacement for the **linear shape function** and **load, plate diameter** of **40mm** and **100mm** respectively, using the three meshes.

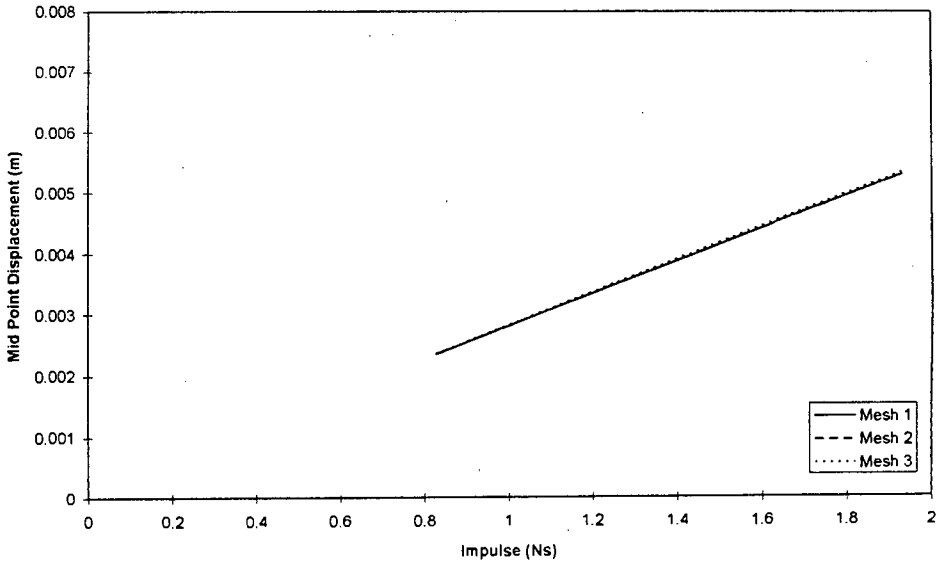

Figure G.9 Theoretical mid-point displacement for the **quadratic shape function** and **load to plate diameter ratio** of **1/3** (as used by Bodner and Symonds [4]), using the three meshes.

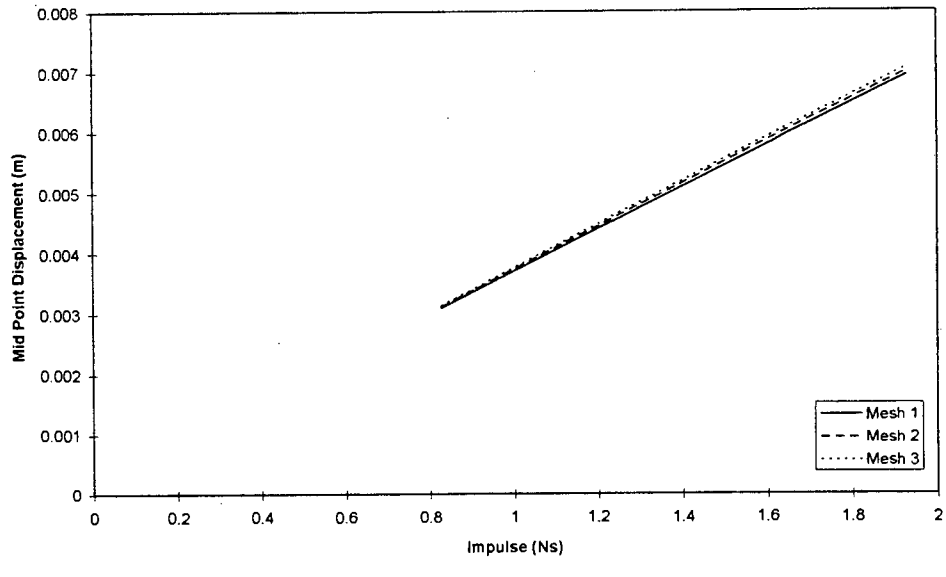

Figure G.10 Theoretical mid-point displacement for the **linear shape function** and **load to plate diameter ratio** of **1/3** (as used by Bodner and Symonds [4]), using the three meshes.

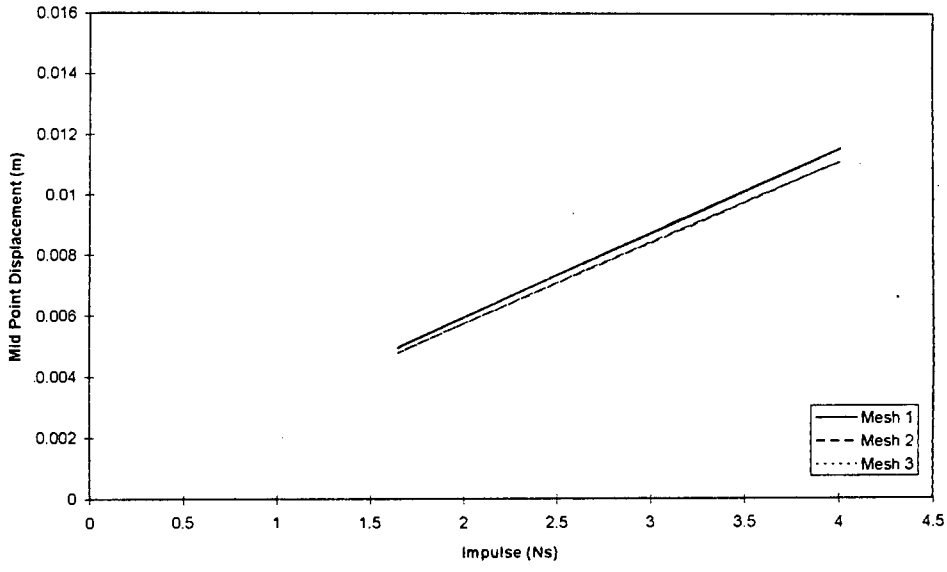

Figure G.11 Theoretical mid-point displacement for the **quadratic shape function** and **load to plate diameter ratio** of **1/2** (as used by Bodner and Symonds [4]), using the three meshes.

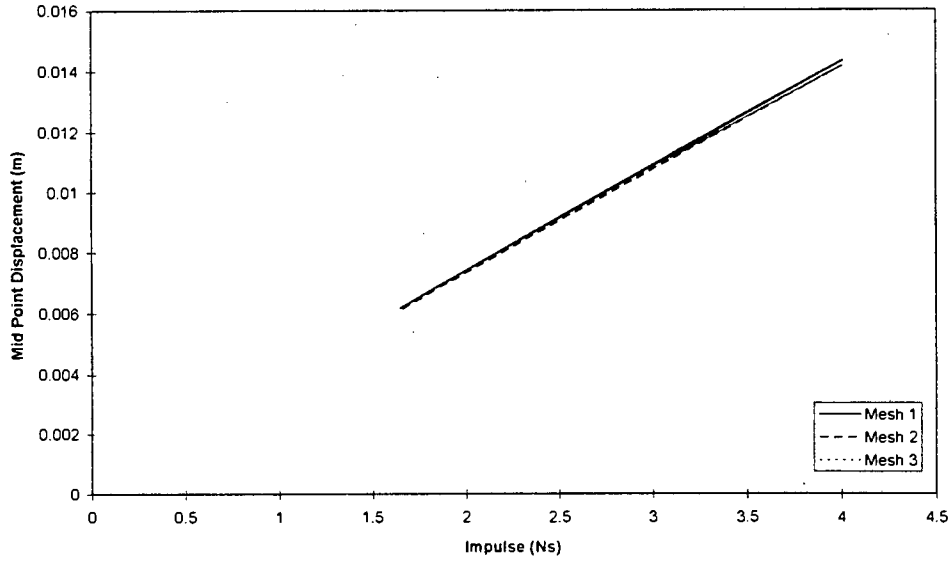

Figure G.12 Theoretical mid-point displacement for the **linear shape function** and **load to plate diameter ratio** of **1/2** (as used by Bodner and Symonds [4]), using the three meshes.

APPENDIX H

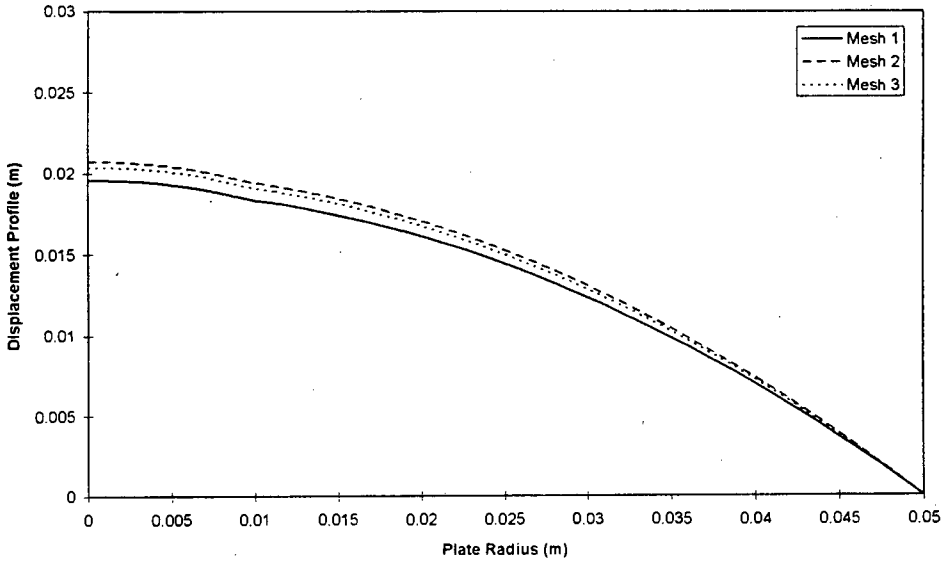

Figure H.1 Theoretical displacement profile for the **quadratic shape function, load, plate diameter** of **18.3mm** and **100mm** respectively and **impulse** of **9.85Ns,** using the three meshes.

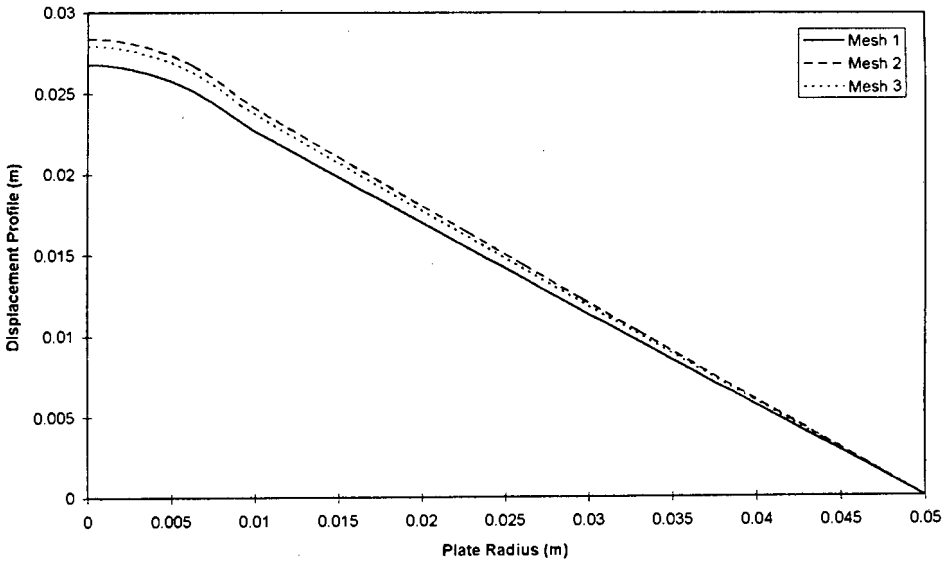

Figure H.2 Theoretical displacement profile for the **linear shape function, load, plate diameter** of **18.3mm** and **100mm** respectively and **impulse** of **9.85Ns,** using the three meshes.

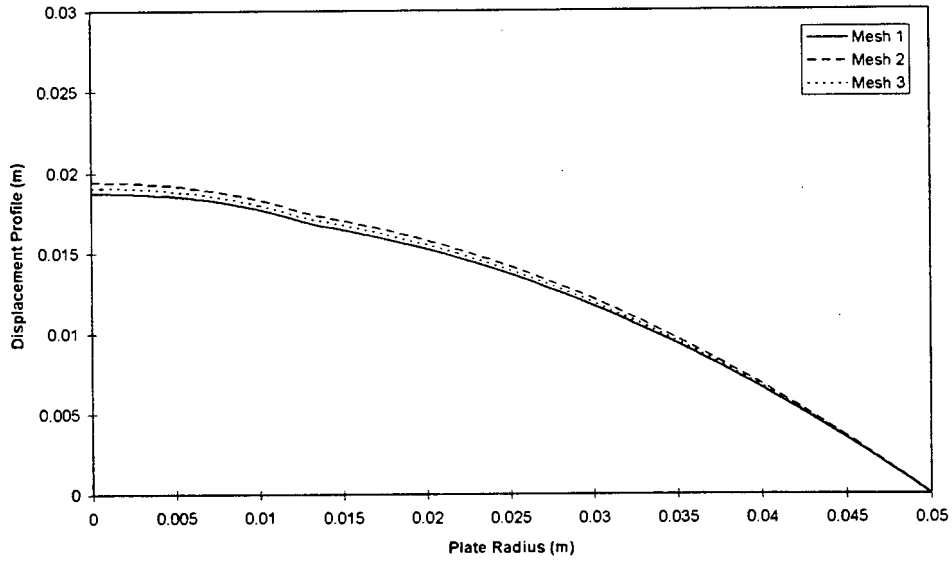

Figure H.3 Theoretical displacement profile for the **quadratic shape function, load, plate diameter** of **25mm** and **100mm** respectively and **impulse** of **9.10Ns,** using the three meshes.

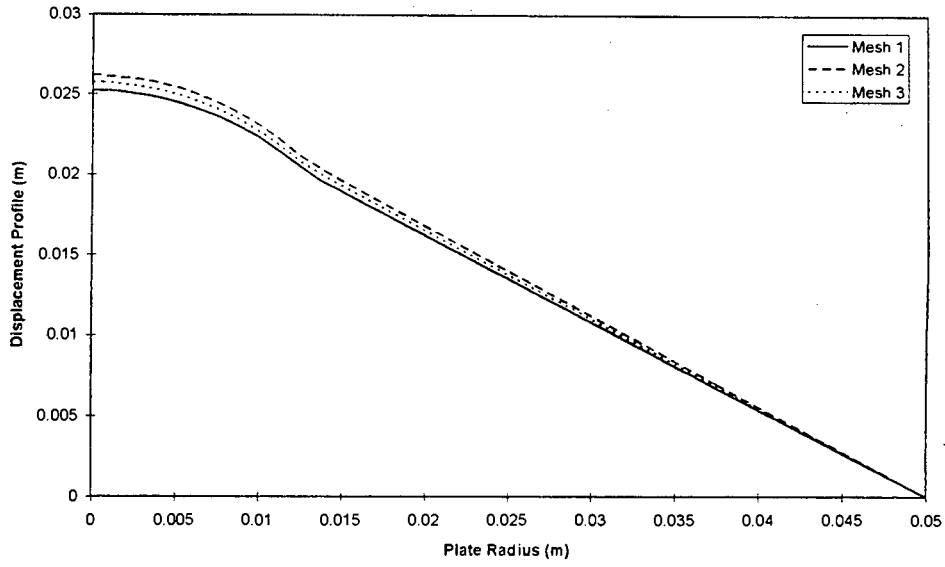

Figure H.4 Theoretical displacement profile for the **linear shape function, load, plate diameter** of **25mm** and **100mm** respectively and **impulse** of **9.10Ns,** using the three meshes.

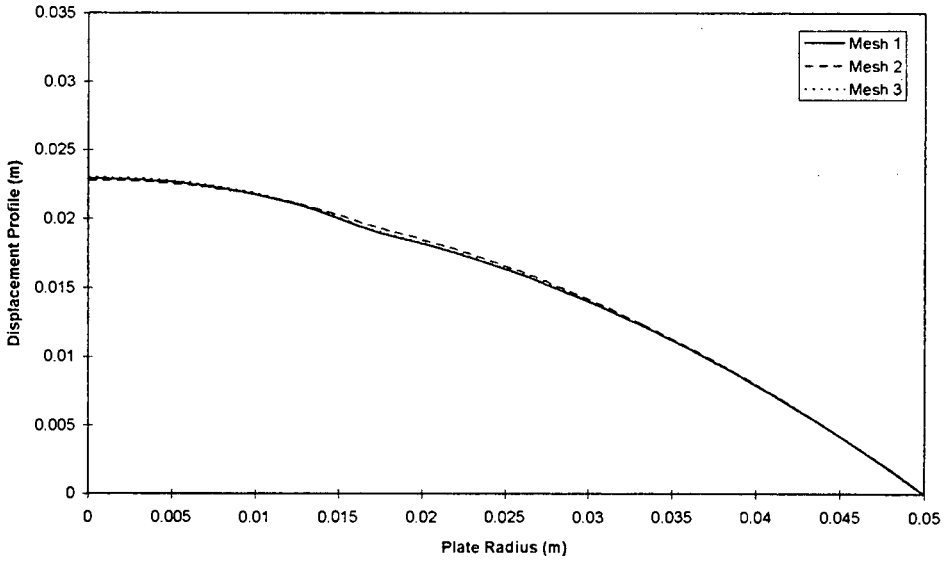

Figure H.5 Theoretical displacement profile for the **quadratic shape function, load, plate diameter** of **33mm** and **100mm** respectively and **impulse** of **10.88Ns,** using the three meshes.

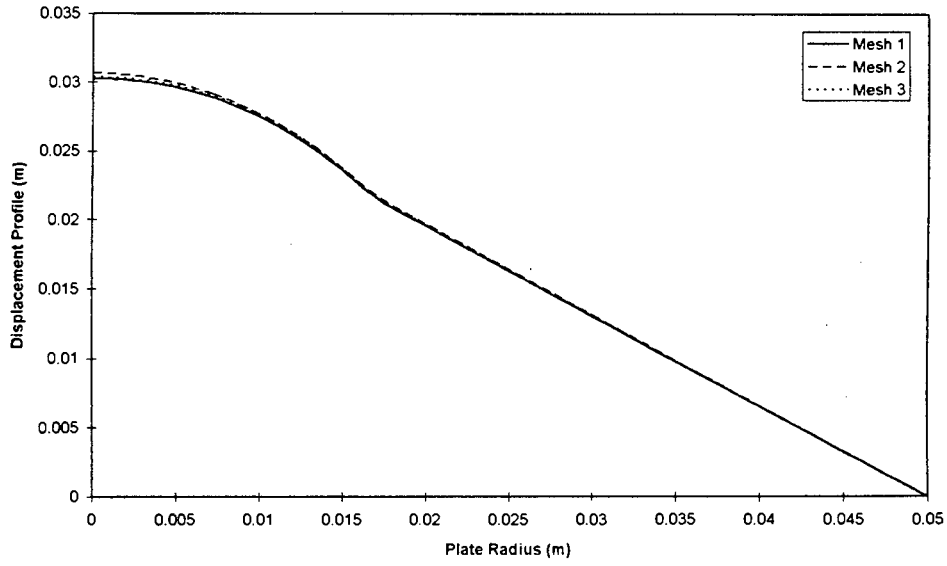

Figure H.6 Theoretical displacement profile for the **linear shape function, load, plate diameter** of **33mm** and **100mm** respectively and **impulse** of **10.88Ns,** using the three meshes.

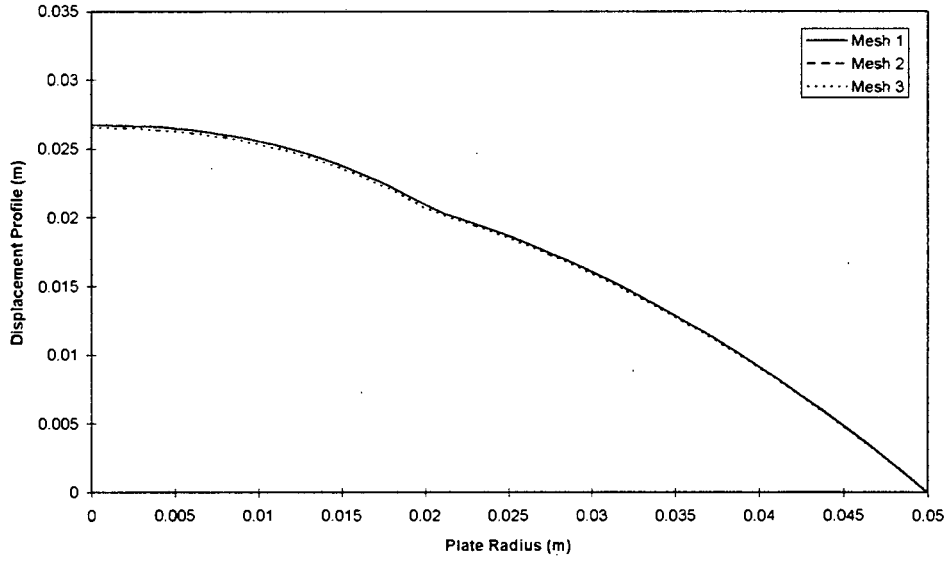

Figure H.7 Theoretical displacement profile for the **quadratic shape function, load, plate diameter** of **40mm** and **100mm** respectively and **impulse** of **12.41Ns,** using the three meshes.

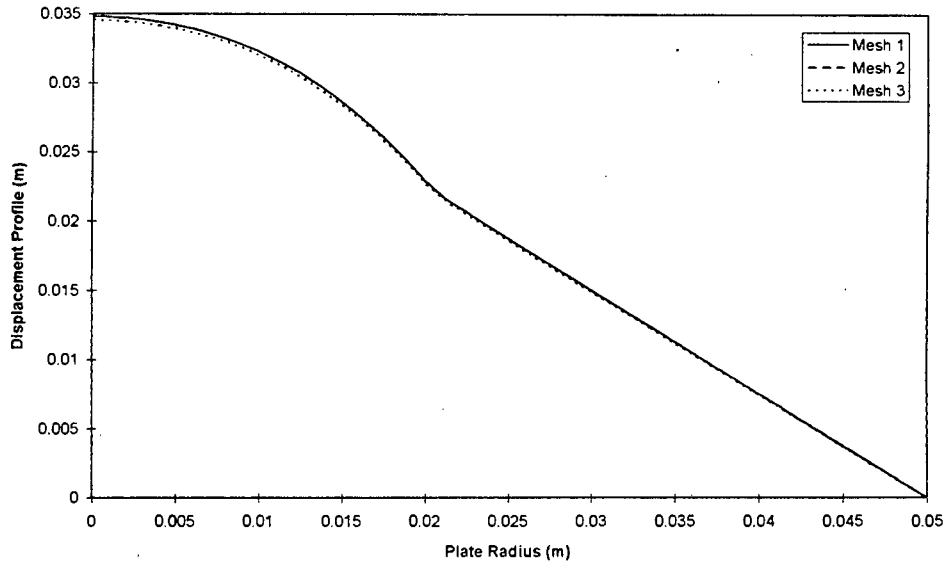

Figure H.8 Theoretical displacement profile for the **linear shape function, load, plate diameter** of **40mm** and **100mm** respectively and **impulse** of **12.41Ns,** using the three meshes.

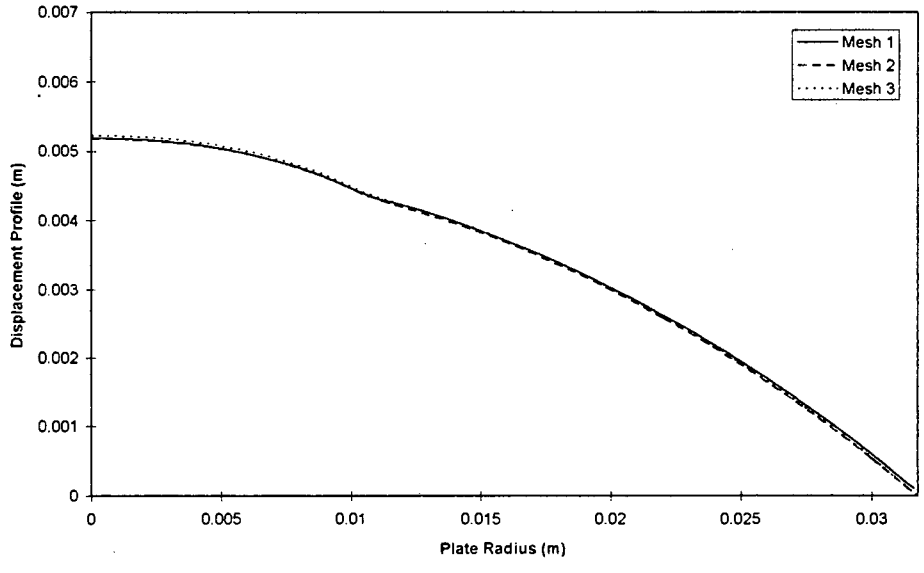

Figure H.9 Theoretical displacement profile for the **quadratic shape function, load** to **plate diameter** ratio of **1/3** (as used by Bodner and Symonds [4]) and **impulse** of **1.89Ns,** using the three meshes.

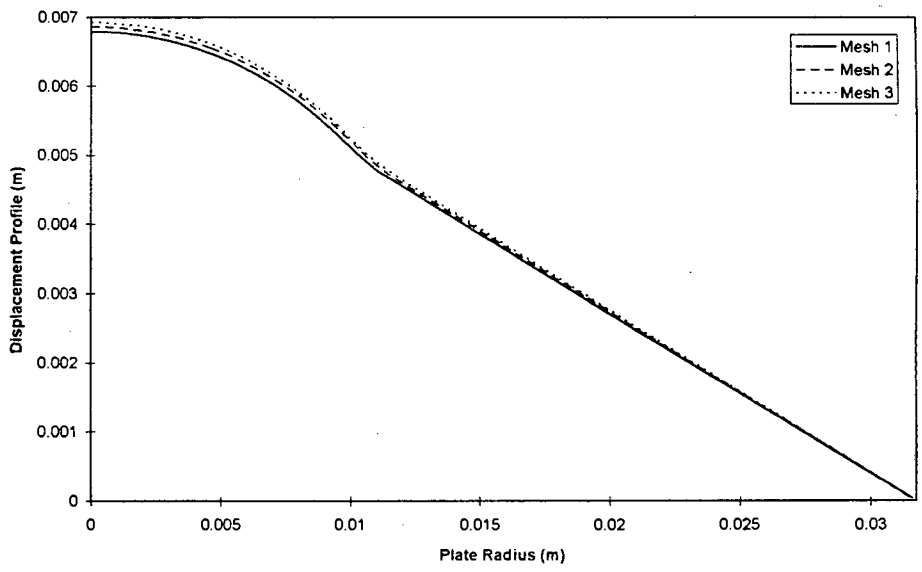

Figure H.10 Theoretical displacement profile for the **linear shape function, load** to **plate diameter** ratio of **1/3** (as used by Bodner and Symonds [4]) and **impulse** of **1.89Ns,** using the three meshes.

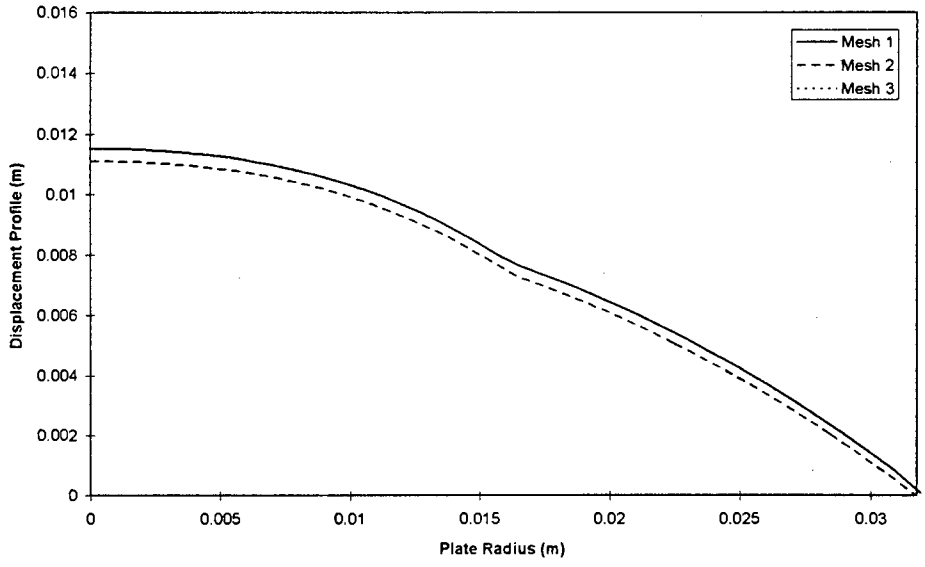

Figure H.11 Theoretical displacement profile for the **quadratic shape function, load** to **plate diameter** ratio of **1/2** (as used by Bodner and Symonds [4]) and **impulse** of **4.007Ns,** using the three meshes.

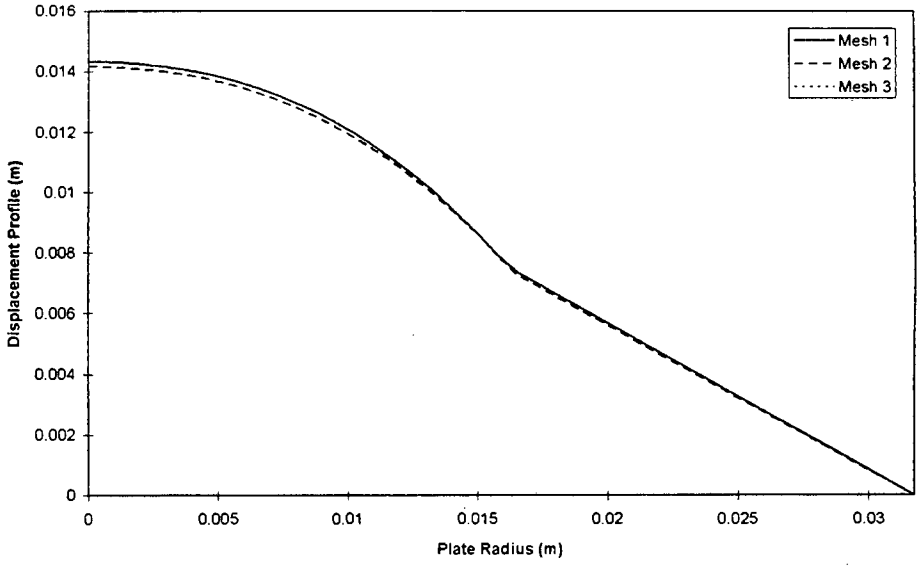

Figure H.12 Theoretical displacement profile for the **linear shape function, load** to **plate diameter** ratio of **1/2** (as used by Bodner and Symonds [4]) and **impulse** of **4.007Ns,** using the three meshes.

APPENDIX I

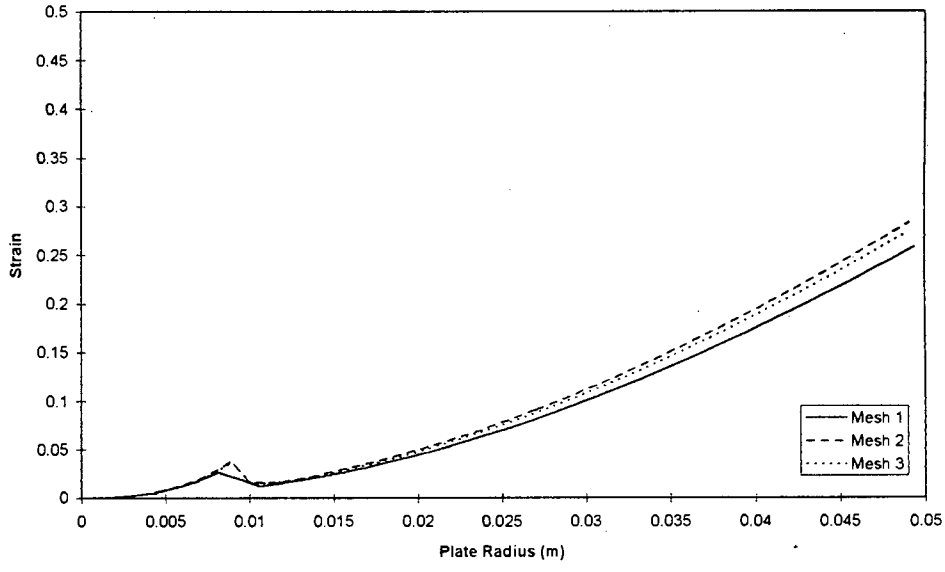

Figure I.1 Theoretical strain distribution for the **quadratic shape function, load, plate diameter** of **18.3mm** and **100mm** respectively and **impulse** of **9.85Ns,** using the three meshes.

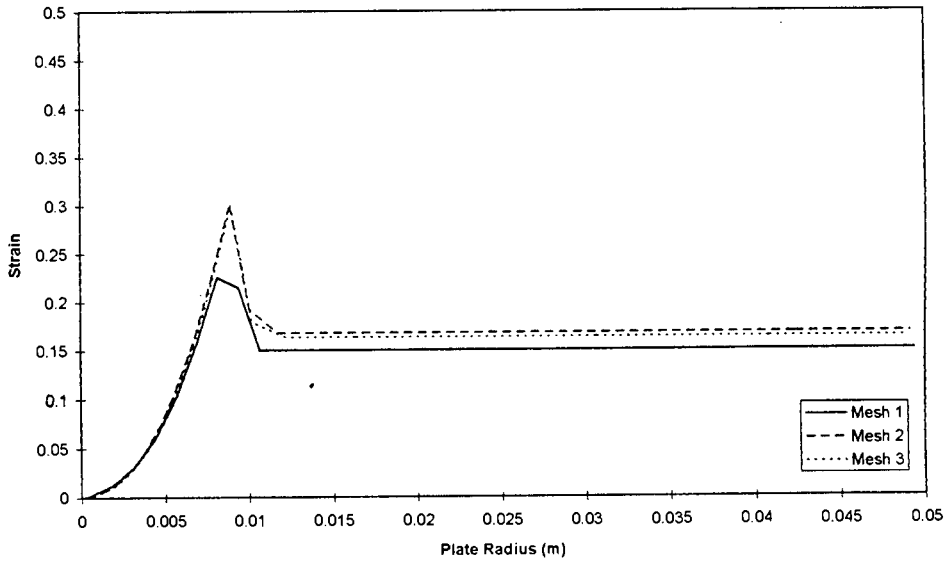

Figure I.2 Theoretical strain distribution for the **linear shape function, load, plate diameter** of **18.3mm** and **100mm** respectively and **impulse** of **9.85Ns,** using the three meshes.

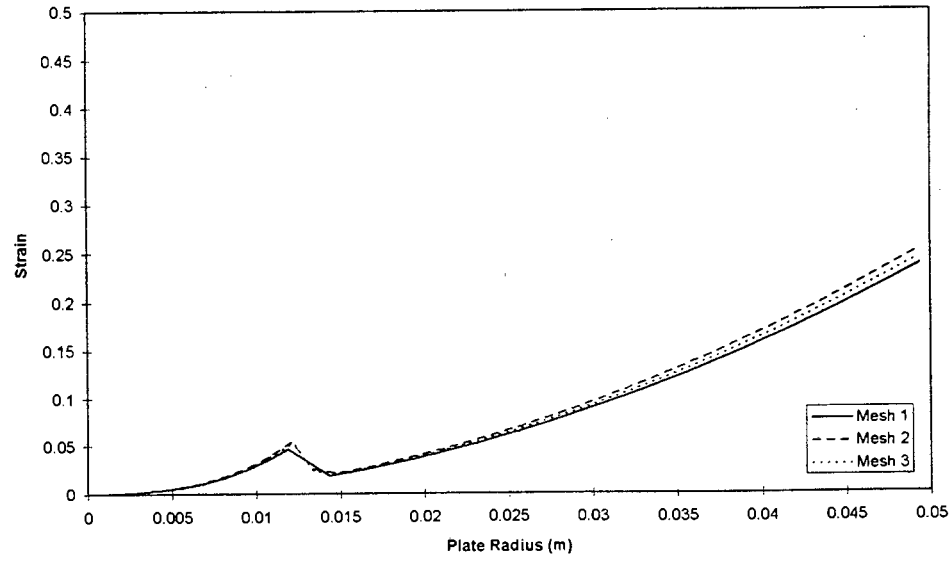

Figure I.3 Theoretical strain distribution for the **quadratic shape function, load, plate diameter** of **25mm** and **100mm** respectively and **impulse** of **9.10Ns,** using the three meshes.

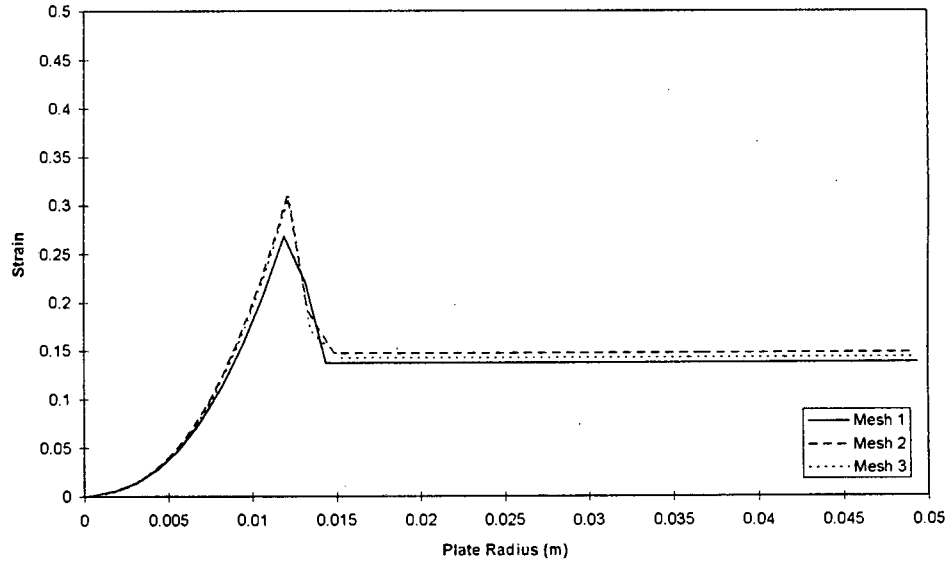

Figure I.4 Theoretical strain distribution for the **linear shape function, load, plate diameter** of **25mm** and **100mm** respectively and **impulse** of **9.10Ns,** using the three meshes.

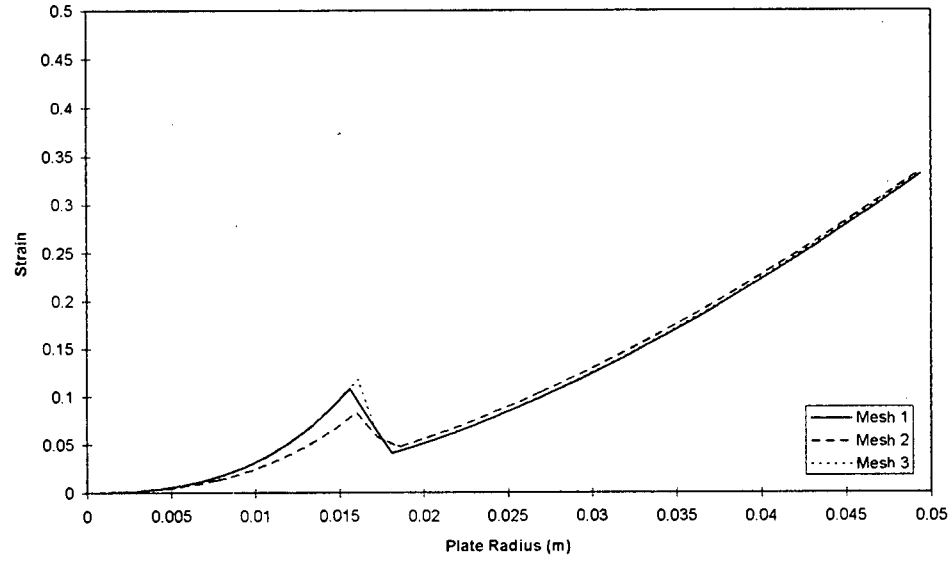

Figure I.5 Theoretical strain distribution for the **quadratic shape function, load, plate diameter** of **33mm** and **100mm** respectively and **impulse** of **10.88Ns,** using the three meshes.

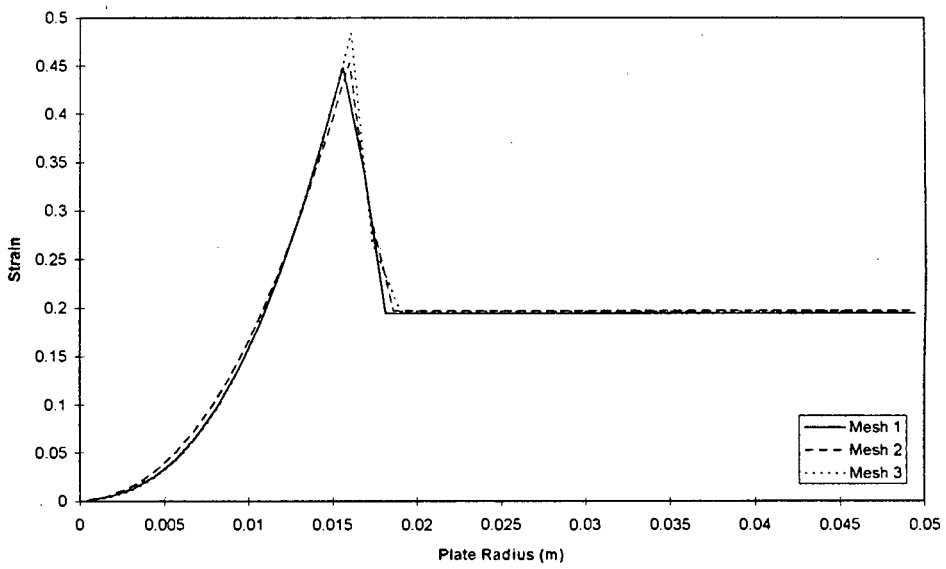

Figure I.6 Theoretical strain distribution for the **linear shape function, load, plate diameter** of **33mm** and **100mm** respectively and **impulse** of **10.88Ns,** using the three meshes.

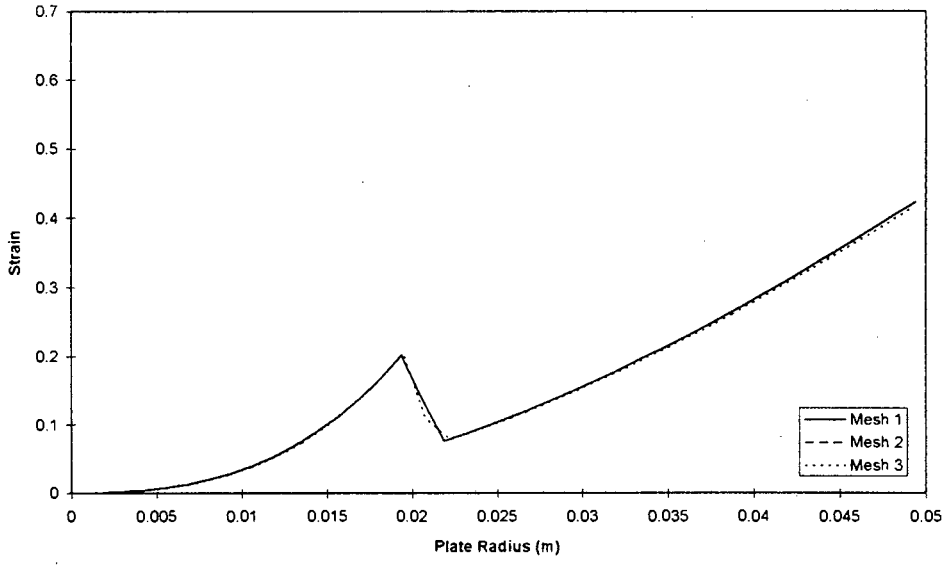

Figure I.7 Theoretical strain distribution for the **quadratic shape function, load, plate diameter** of **40mm** and **100mm** respectively and **impulse** of **12.41Ns,** using the three meshes.

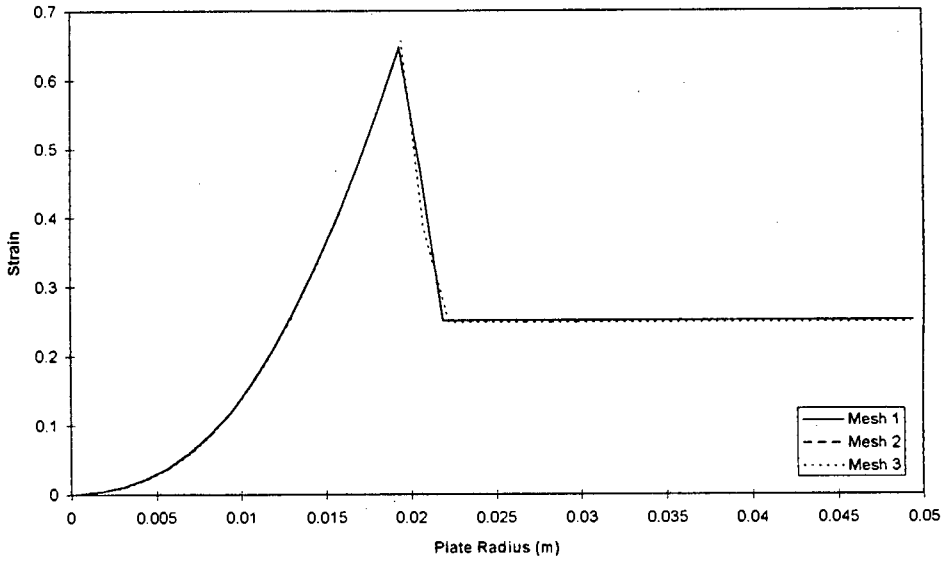

Figure I.8 Theoretical strain distribution for the **linear shape function, load, plate diameter** of **40mm** and **100mm** respectively and **impulse** of **12.41Ns,** using the three meshes.

APPENDIX J

18.3mm LOAD DIAMETER AND 100mm PLATE DIAMETER

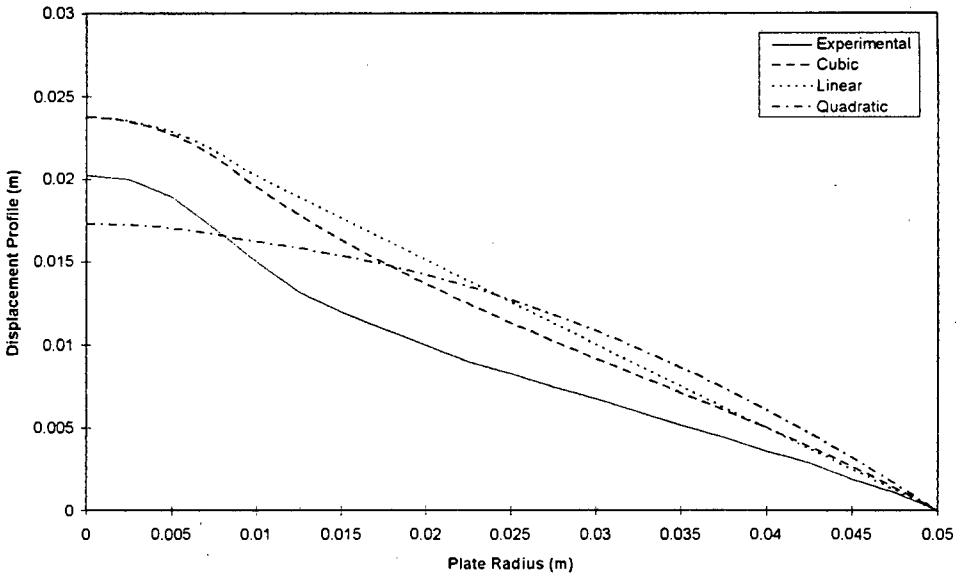

Figure J.1 Comparison between experimental and theoretical displacement profiles for the cubic, quadratic and linear shape functions, **plate diameter 100mm, load diameter 18.3mm** and **impulse** of **8.29Ns.**

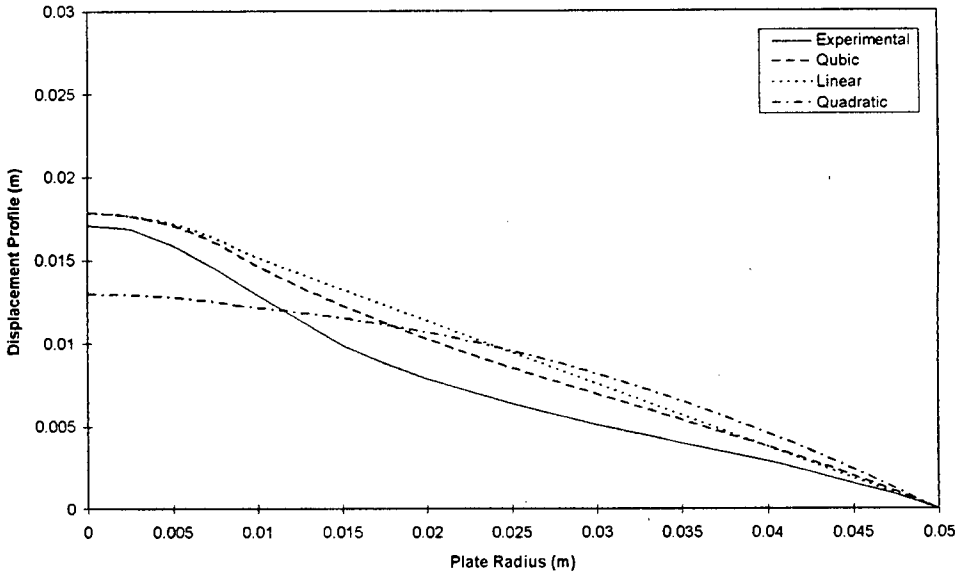

Figure J.2 Comparison between experimental and theoretical displacement profiles for the cubic, quadratic and linear shape functions, **plate diameter 100mm, load diameter 18.3mm** and **impulse** of **6.13Ns.**

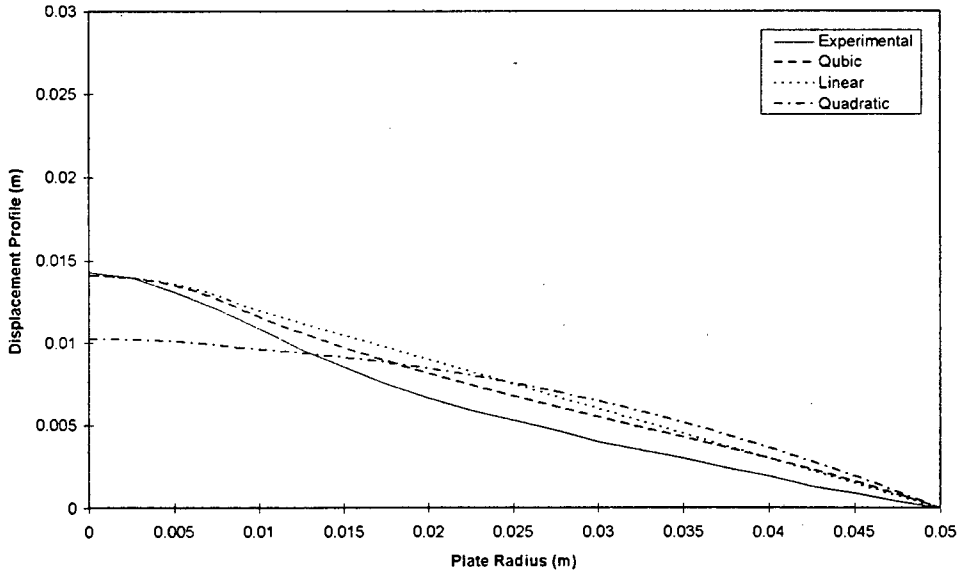

Figure J.3 Comparison between experimental and theoretical displacement profiles for the cubic, quadratic and linear shape functions, **plate diameter 100mm, load diameter 18.3mm** and **impulse** of **4.79Ns.**

25mm LOAD DIAMETER AND 100mm PLATE DIAMETER

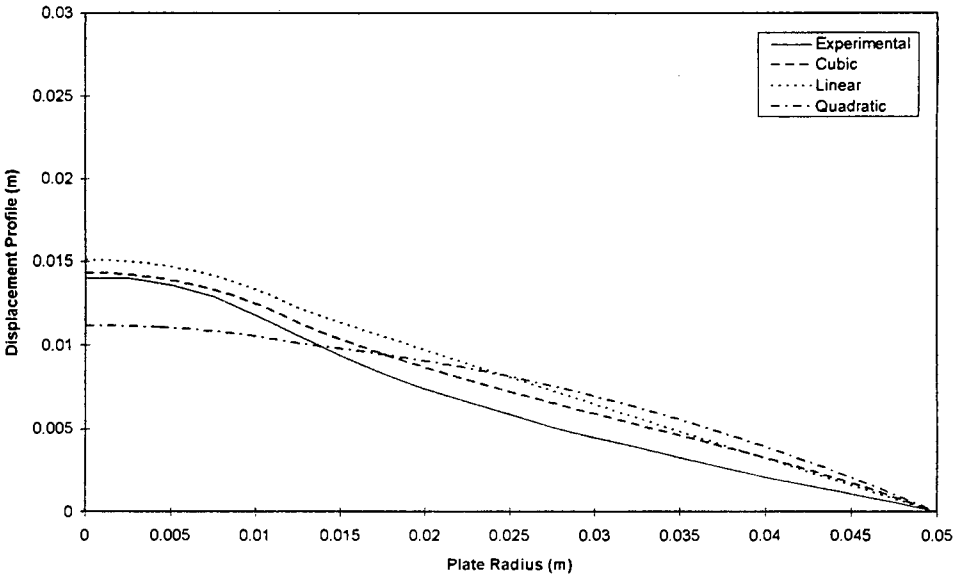

Figure J.4 Comparison between experimental and theoretical displacement profiles for the cubic, quadratic and linear shape functions, **plate diameter 100mm, load diameter 25mm** and **impulse** of **5.19Ns.**

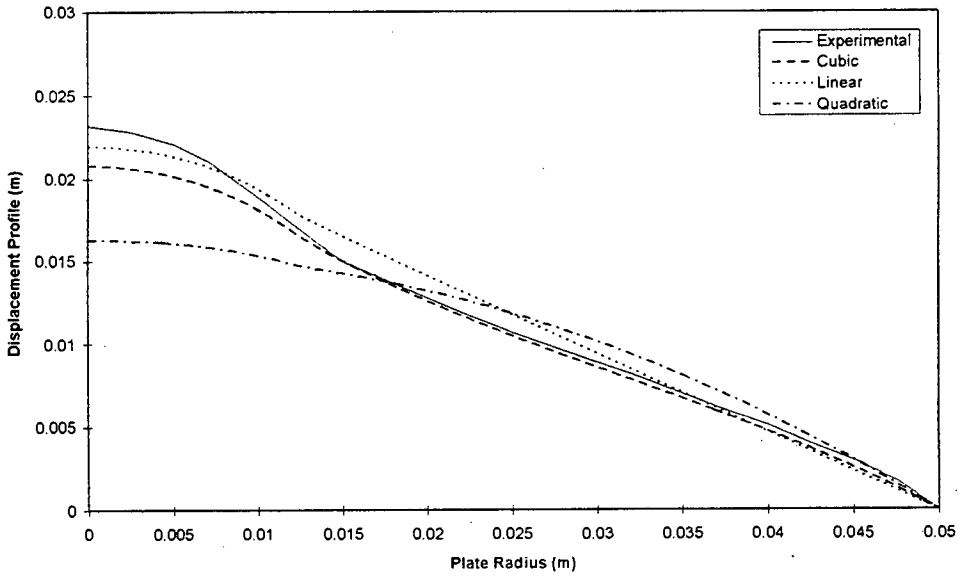

Figure J.5 Comparison between experimental and theoretical displacement profiles for the cubic, quadratic and linear shape functions, **plate diameter 100mm, load diameter 25mm** and **impulse** of **7.70Ns.**

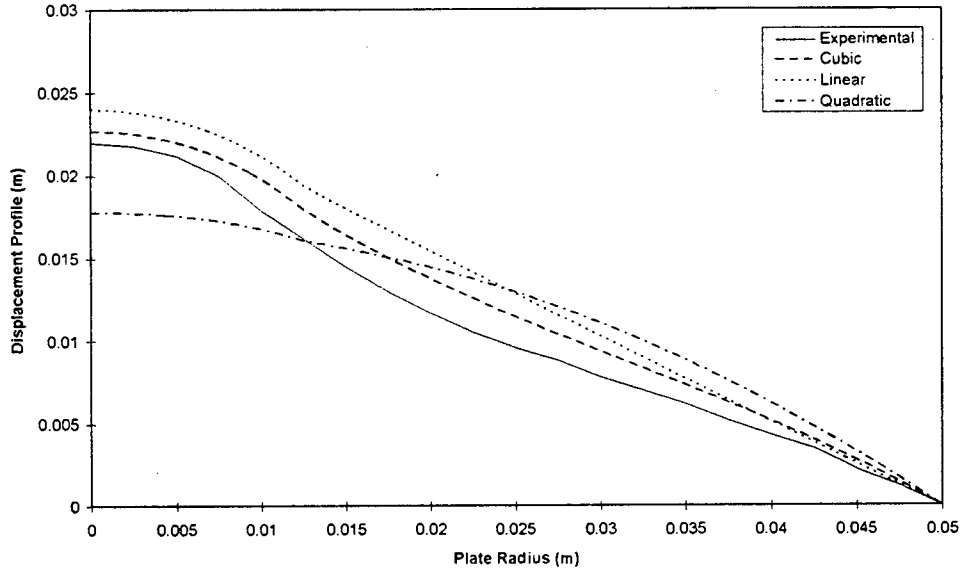

Figure J.6 Comparison between experimental and theoretical displacement profiles for the cubic, quadratic and linear shape functions, **plate diameter 100mm, load diameter 25mm** and **impulse** of **8.45Ns.**

33mm LOAD DIAMETER AND 100mm PLATE DIAMETER

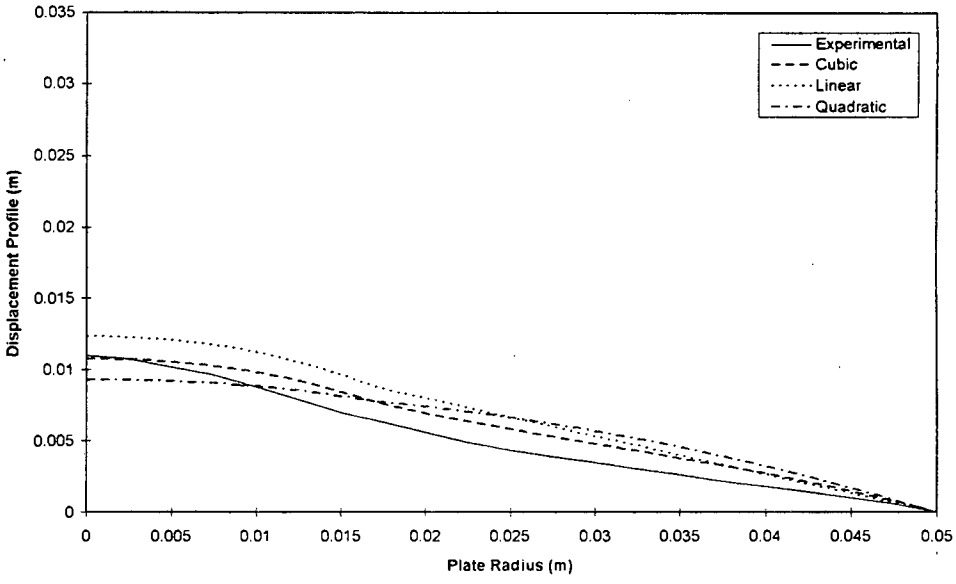

Figure J.7 Comparison between experimental and theoretical displacement profiles for the cubic, quadratic and linear shape functions, **plate diameter 100mm, load diameter 33mm** and **impulse** of **4.21Ns.**

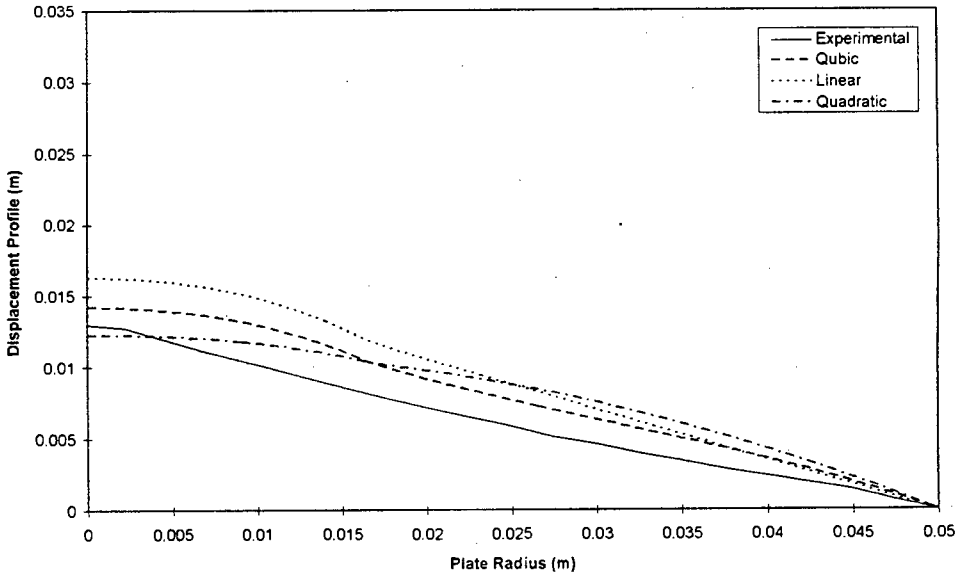

Figure J.8 Comparison between experimental and theoretical displacement profiles for the cubic, quadratic and linear shape functions, **plate diameter 100mm, load diameter 33mm** and **impulse** of **5.63Ns.**

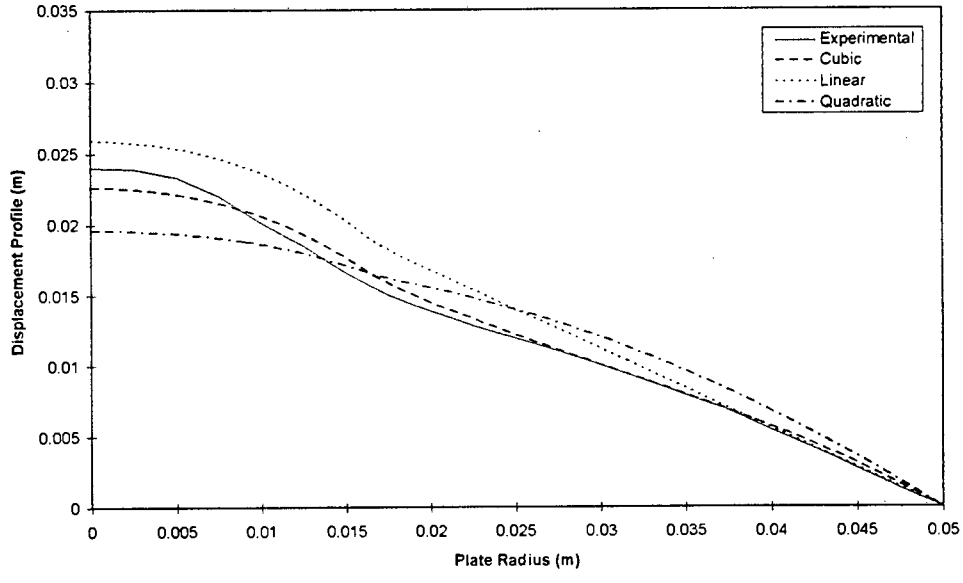

Figure J.9 Comparison between experimental and theoretical displacement profiles for the cubic, quadratic and linear shape functions, **plate diameter 100mm, load diameter 33mm** and **impulse** of **9.19Ns.**

40mm LOAD DIAMETER AND 100mm PLATE DIAMETER

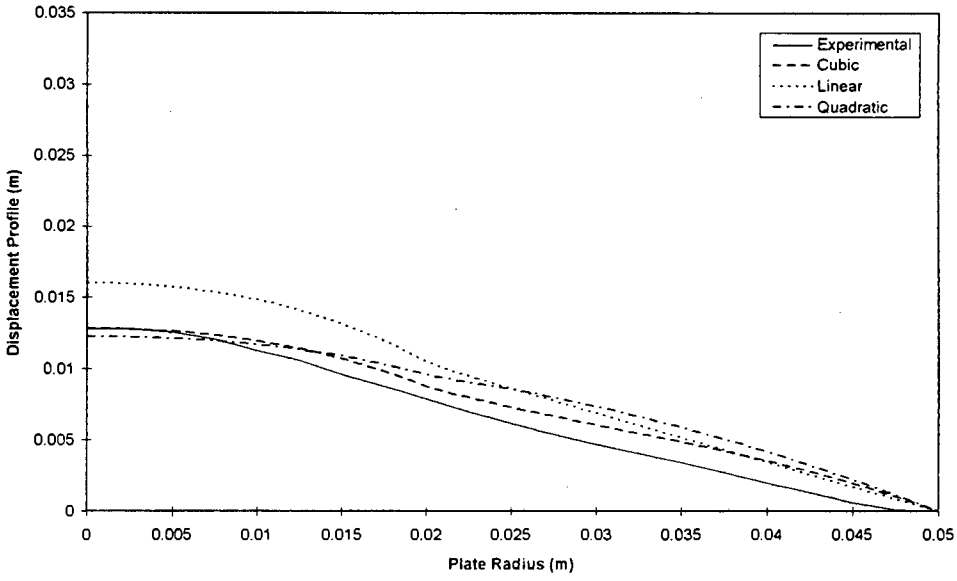

Figure J.10 Comparison between experimental and theoretical displacement profiles for the cubic, quadratic and linear shape functions, **plate diameter 100mm, load diameter 40mm** and **impulse** of **5.51Ns.**

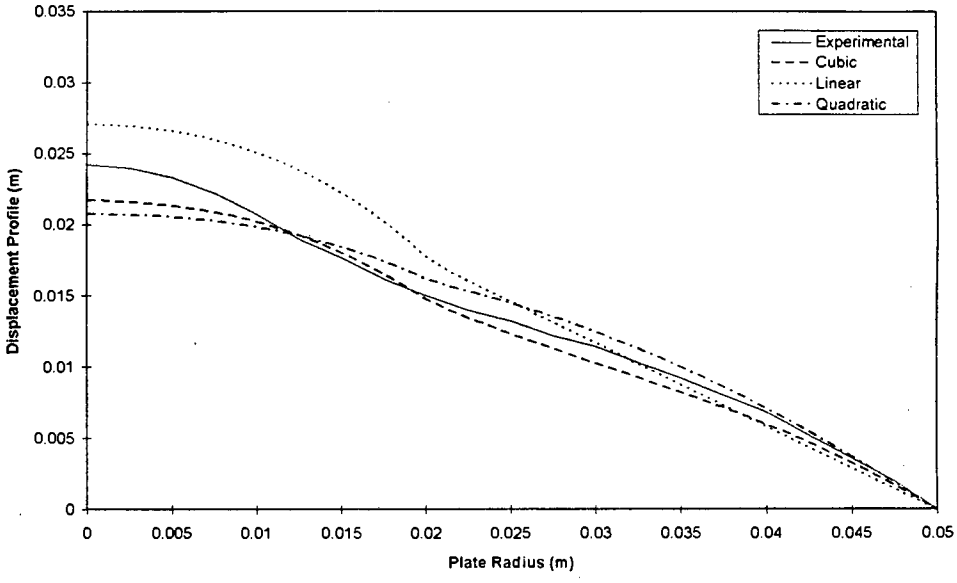

Figure J.11 Comparison between experimental and theoretical displacement profiles for the cubic, quadratic and linear shape functions, **plate diameter 100mm, load diameter 40mm** and **impulse** of **9.58Ns.**

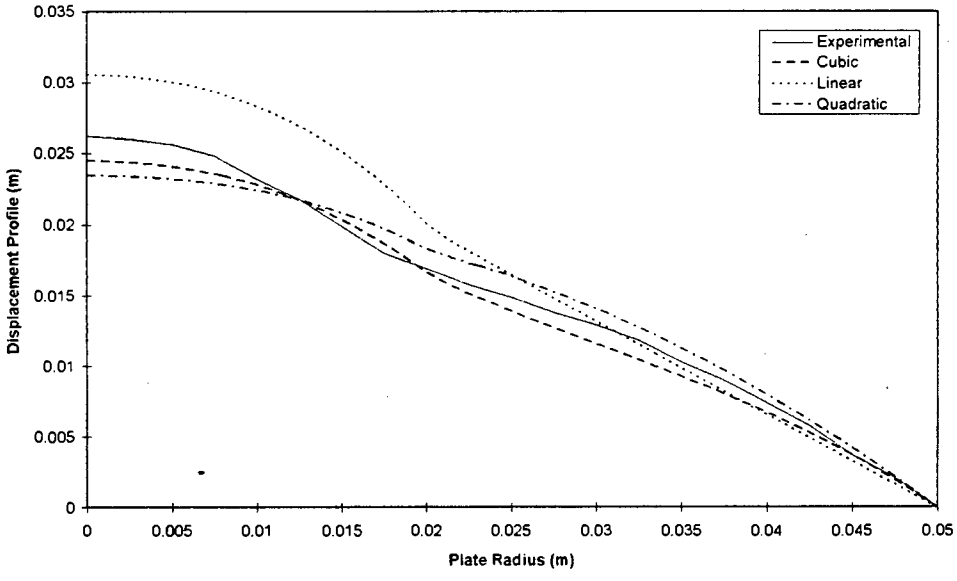

Figure J.12 Comparison between experimental and theoretical displacement profiles for the cubic, quadratic and linear shape functions, **plate diameter 100mm, load diameter 40mm** and **impulse** of **10.89Ns.**

APPENDIX K

18.3mm LOAD DIAMETER AND 100mm PLATE DIAMETER.

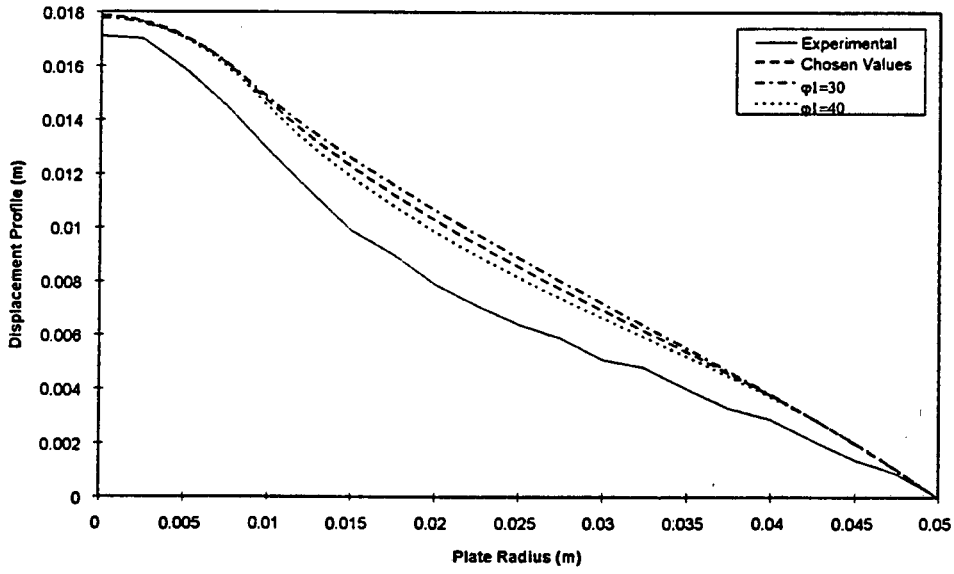

Figure K.1 Affects of varying φ_1 on the displacement profile for a load diameter of 18.3mm, plate diameter 100mm and impulse of 6.13 Ns.

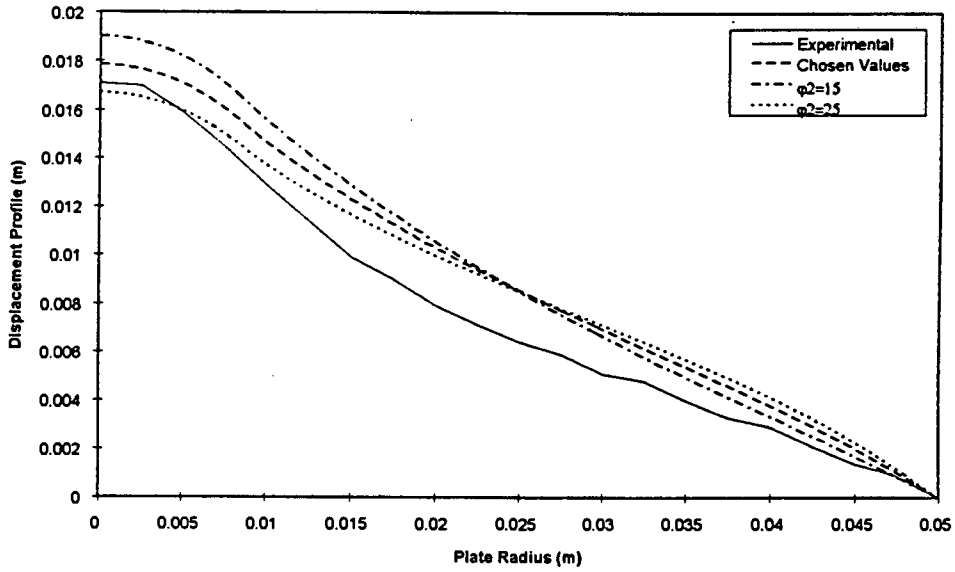

Figure K.2 Affects of varying φ_2 on the displacement profile for a load diameter of 18.3mm, plate diameter 100mm and impulse of 6.13 Ns.

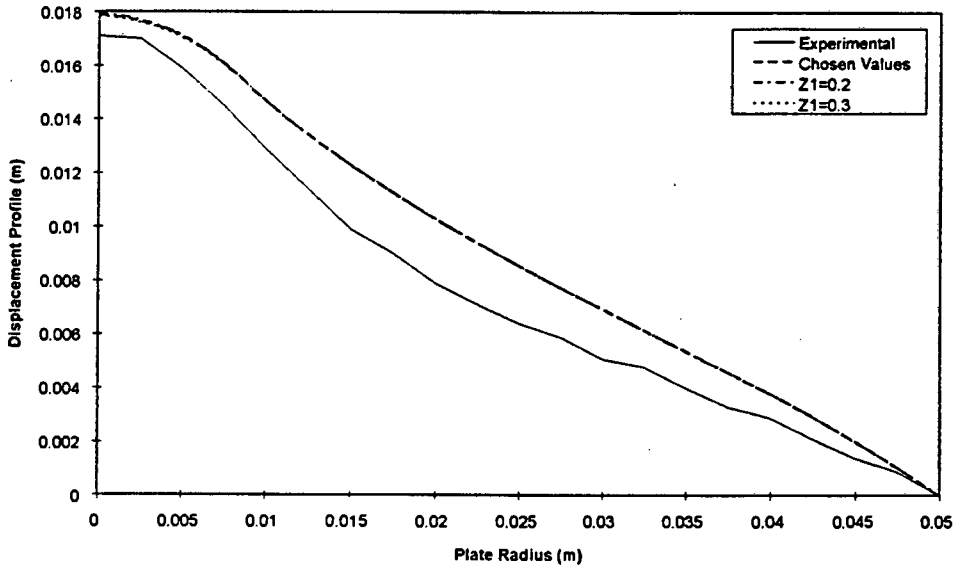

Figure K.3 Affects of varying $Z1$ on the displacement profile for a load diameter of 18.3mm, plate diameter 100mm and impulse of 6.13 Ns.

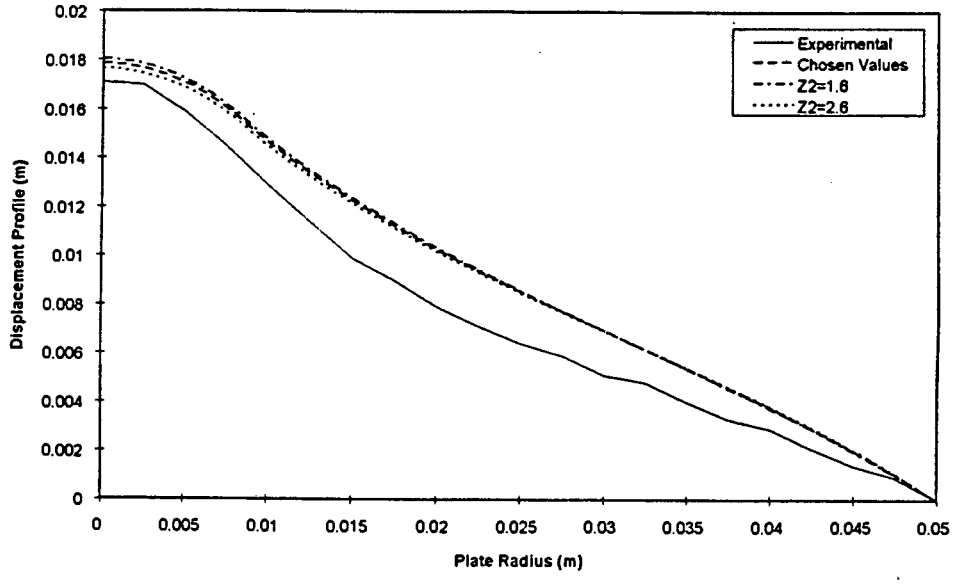

Figure K.4 Affects of varying $Z2$ on the displacement profile for a load diameter of 18.3mm, plate diameter 100mm and impulse of 6.13 Ns.

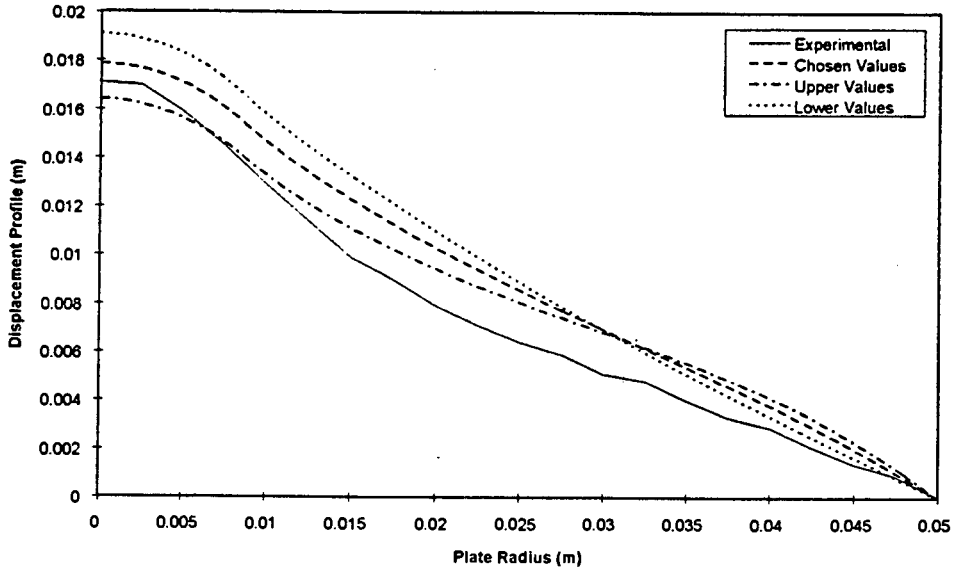

Figure K.5 Combined affects of varying φ_1, φ_2, $Z1$ and $Z2$ on the displacement profile for a load diameter of 18.3mm, plate diameter 100mm and impulse of 6.13Ns.

25mm LOAD DIAMETER AND 100mm PLATE DIAMETER.

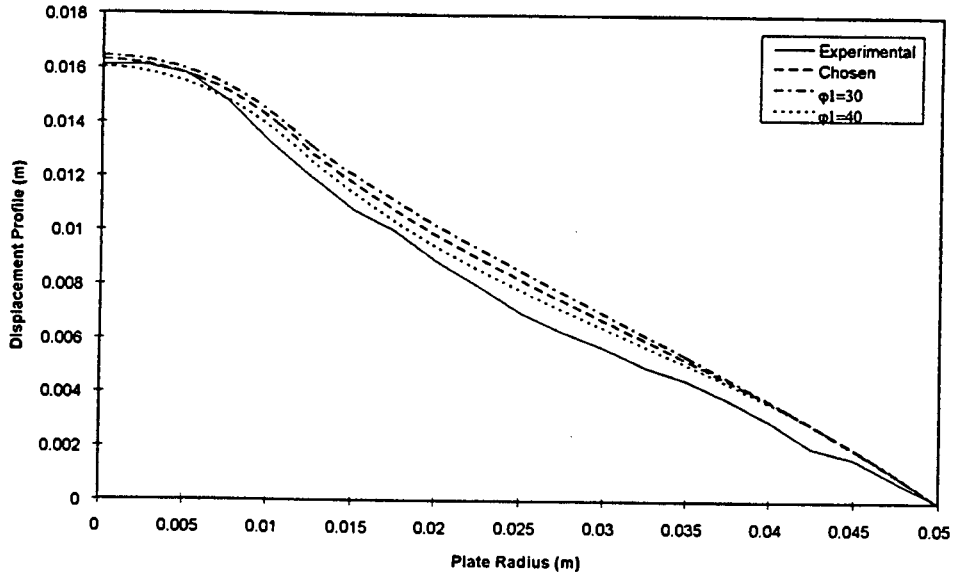

Figure K.6 Affects of varying φ_1 on the displacement profile for a load diameter of 25mm, plate diameter 100mm and impulse of 5.94 Ns.

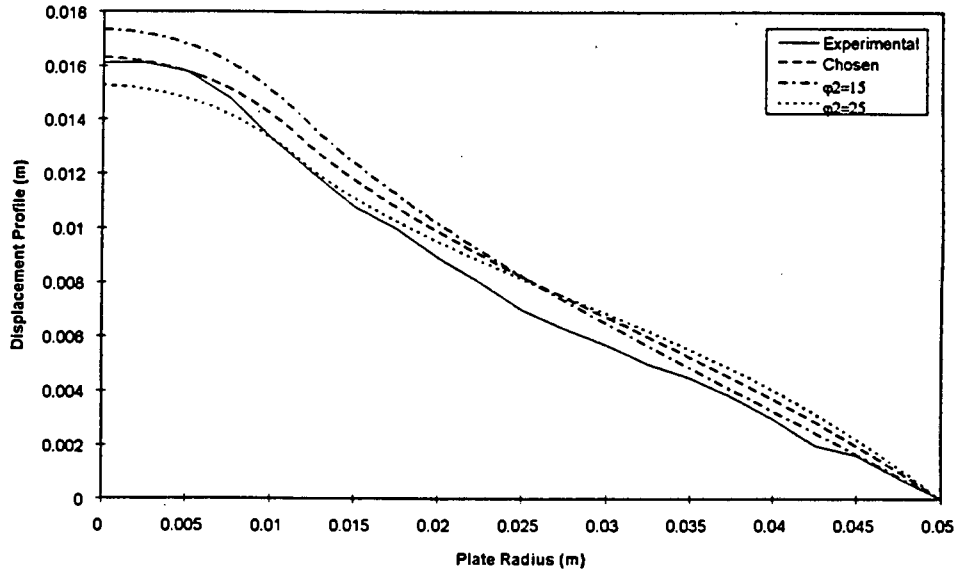

Figure K.7 Affects of varying φ_2 on the displacement profile for a load diameter of 25mm, plate diameter 100mm and impulse of 5.94 Ns.

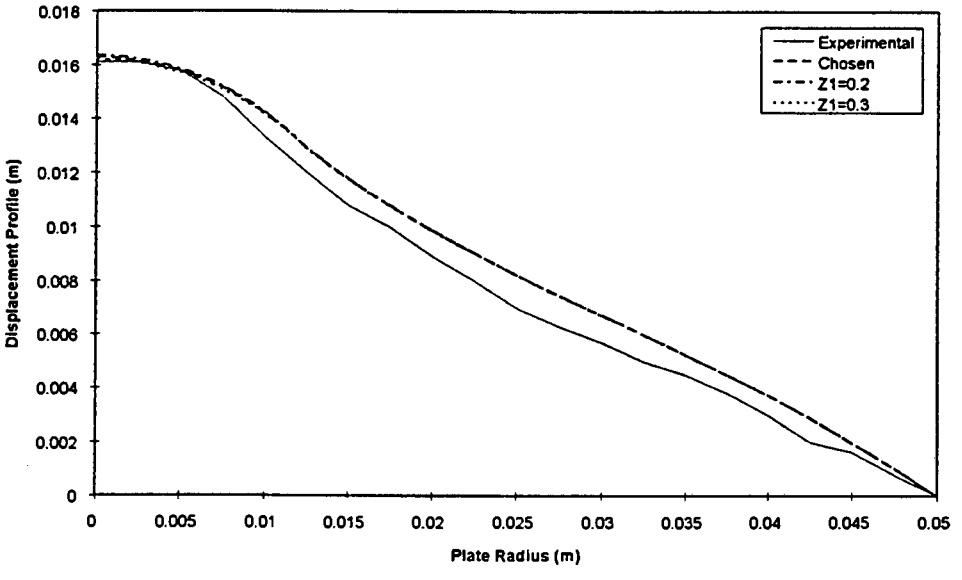

Figure K.8 Affects of varying $Z1$ on the displacement profile for a load diameter of 25mm, plate diameter 100mm and impulse of 5.94 Ns.

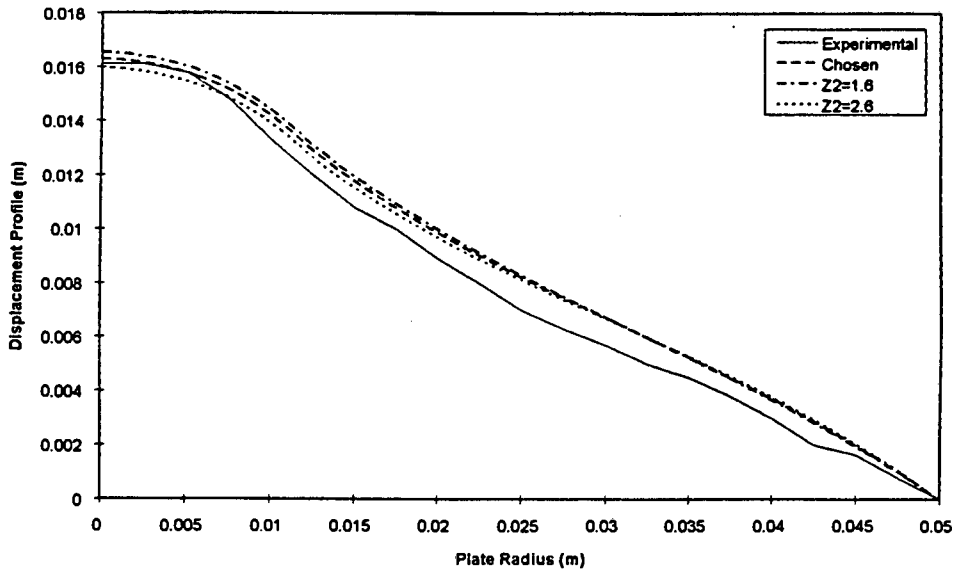

Figure K.9 Affects of varying $Z2$ on the displacement profile for a load diameter of 25mm, plate diameter 100mm and impulse of 5.94 Ns.

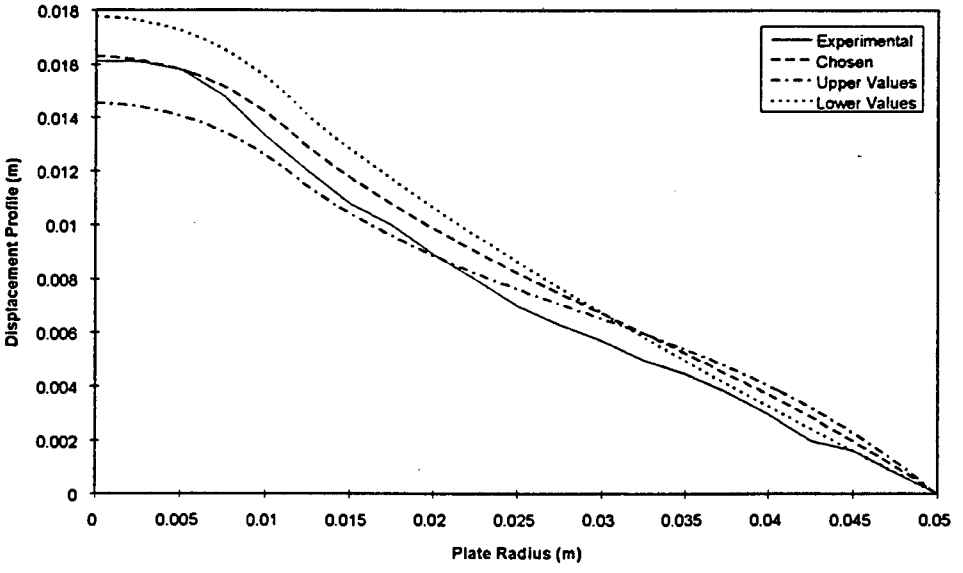

Figure K.10 Combined affects of varying φ_1, φ_2, $Z1$ and $Z2$ on the displacement profile for a load diameter of 25mm, plate diameter 100mm and impulse of 5.94 Ns.

33mm LOAD DIAMETER AND 100mm PLATE DIAMETER.

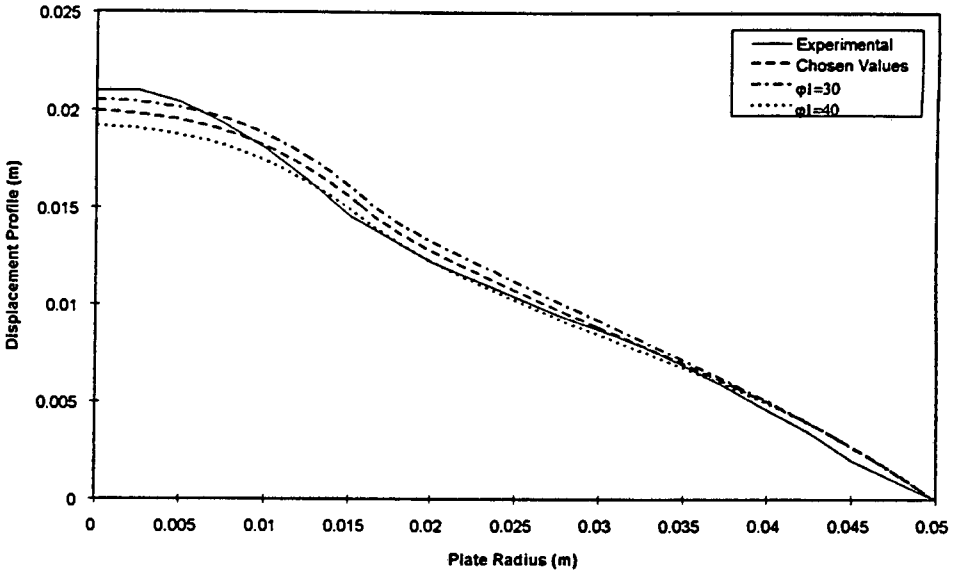

Figure K.11 Affects of varying φ_1 on the displacement profile for a load diameter of 33mm, plate diameter 100mm and impulse of 8.02 Ns.

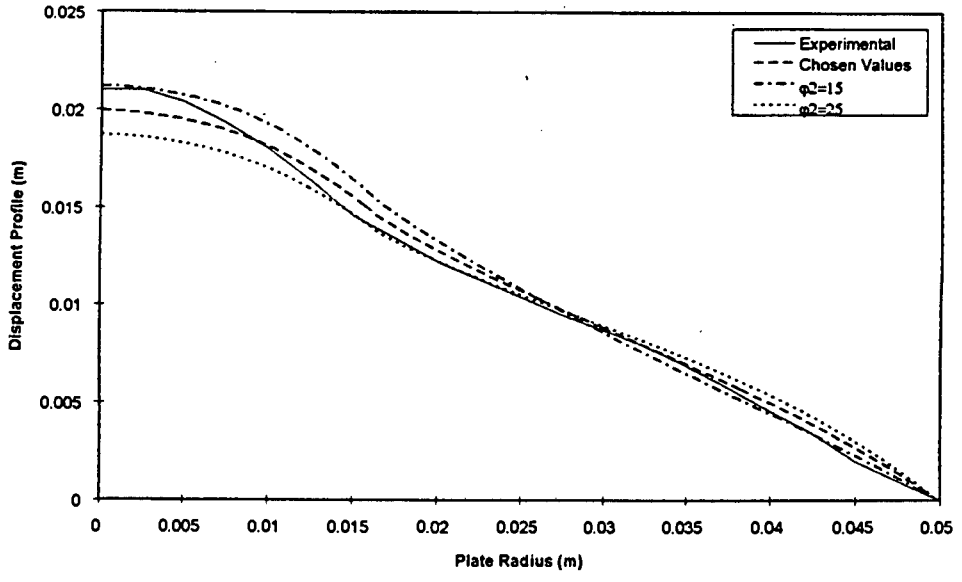

Figure K.12 Affects of varying φ_2 on the displacement profile for a load diameter of 33mm, plate diameter 100mm and impulse of 8.02 Ns.

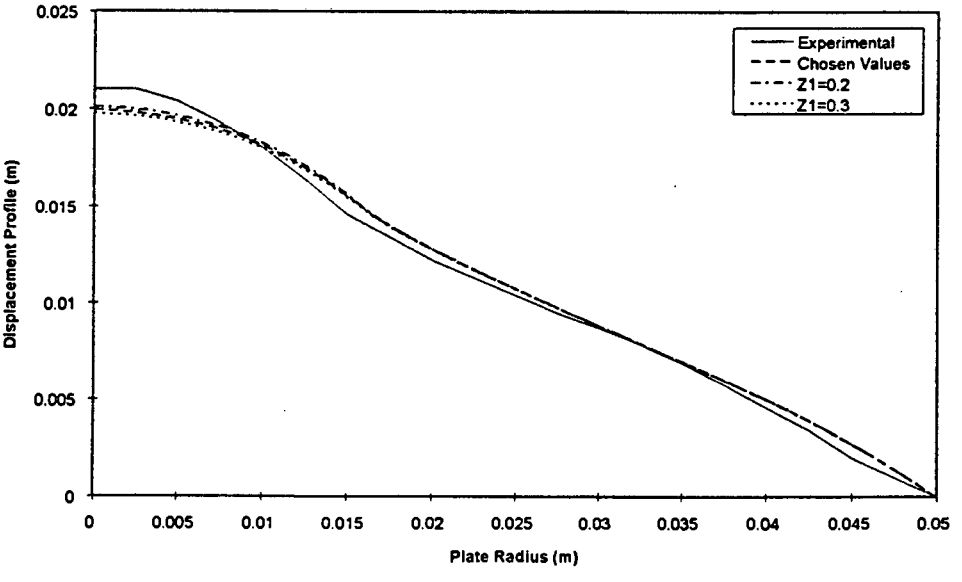

Figure K.13 Affects of varying $Z1$ on the displacement profile for a load diameter of 33mm, plate diameter 100mm and impulse of 8.02 Ns.

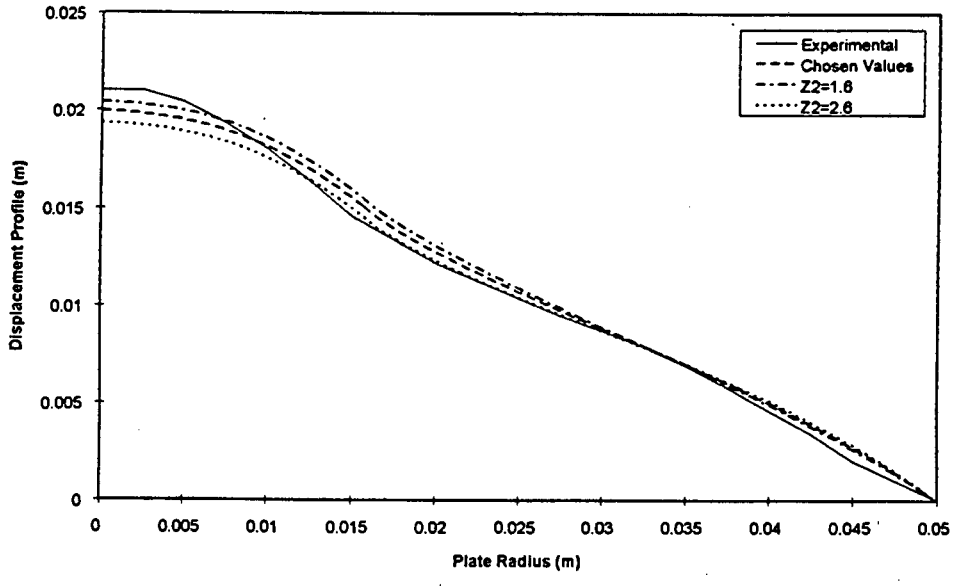

Figure K.14 Affects of varying $Z2$ on the displacement profile for a load diameter of 33mm, plate diameter 100mm and impulse of 8.02 Ns.

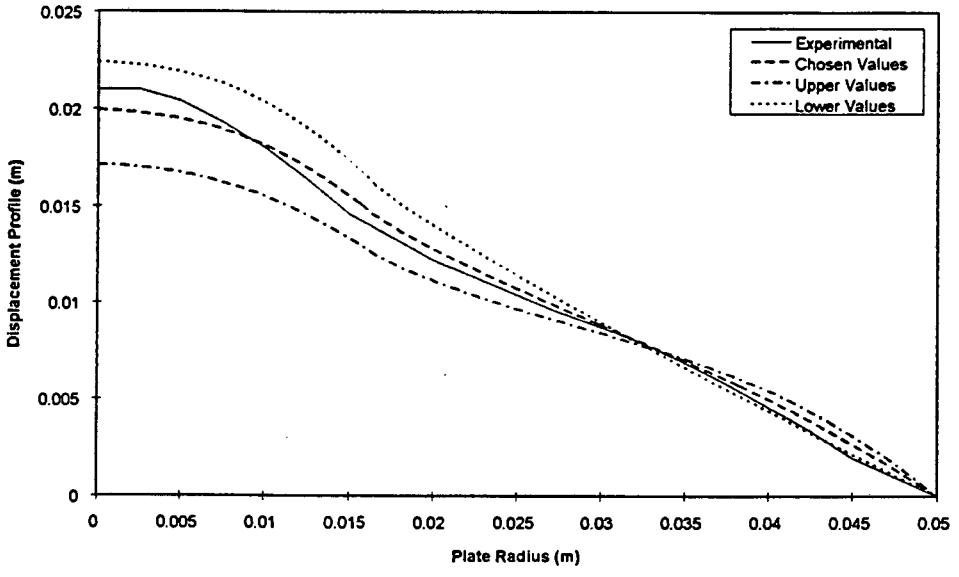

Figure K.15 Combined affects of varying φ_1, φ_2, $Z1$ and $Z2$ on the displacement profile for a load diameter of 33mm, plate diameter 100mm and impulse of 8.02 Ns.

40mm LOAD DIAMETER AND 100mm PLATE DIAMETER.

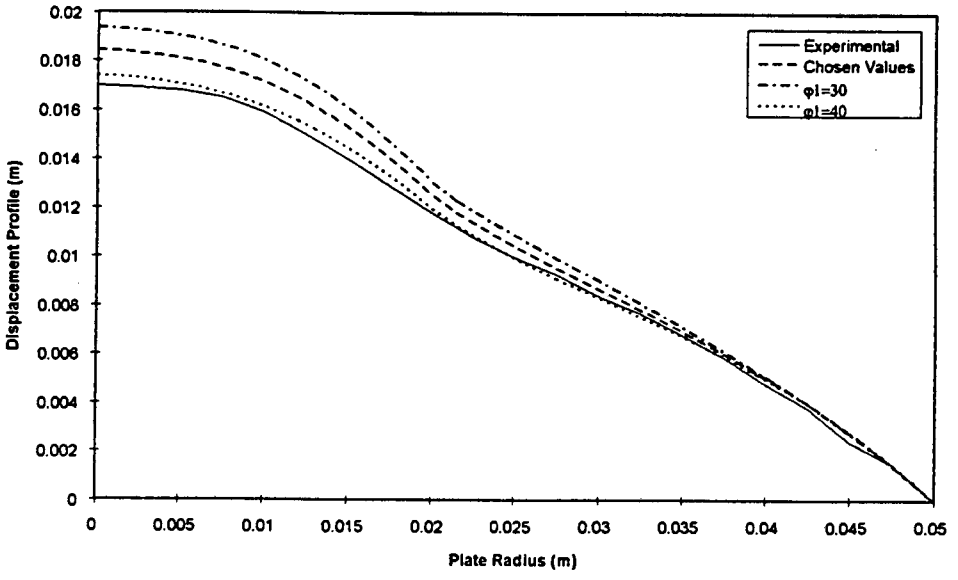

Figure k.16 Affects of varying φ_1 on the displacement profile for a load diameter of 40mm, plate diameter 100mm and impulse of 8.04 Ns.

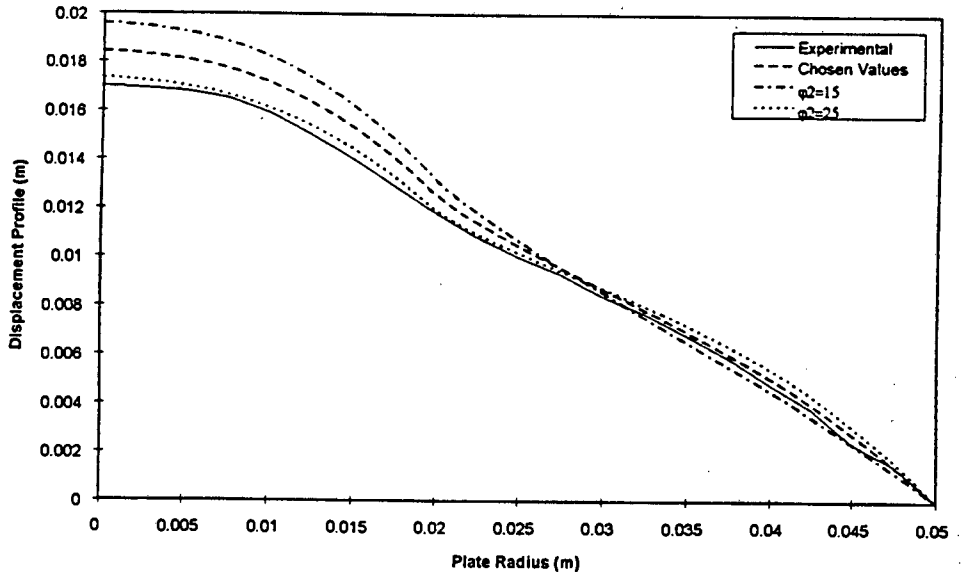

Figure K.17 Affects of varying φ_2 on the displacement profile for a load diameter of 40mm, plate diameter 100mm and impulse of 8.04 Ns.

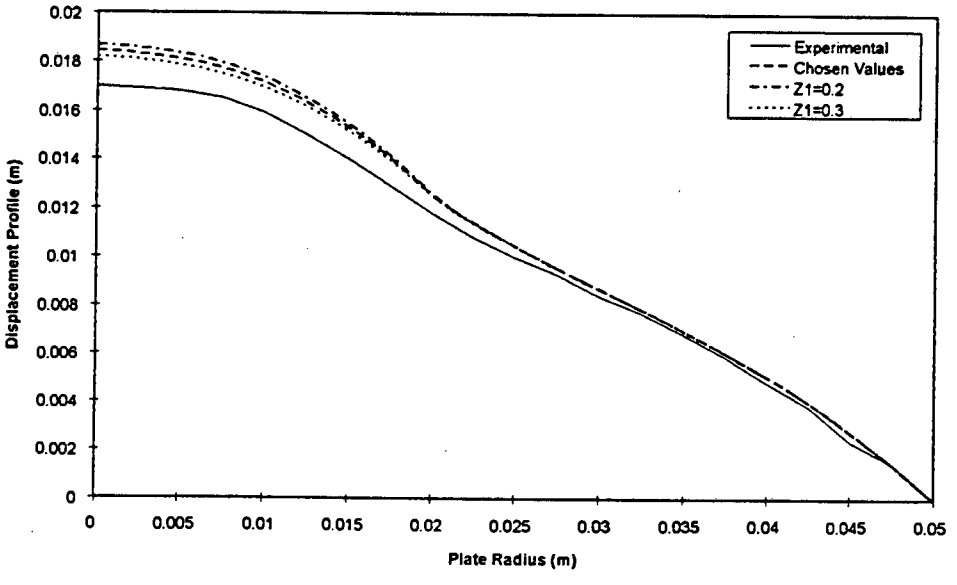

Figure K.18 Affects of varying $Z1$ on the displacement profile for a load diameter of 40mm, plate diameter 100mm and impulse of 8.04 Ns.

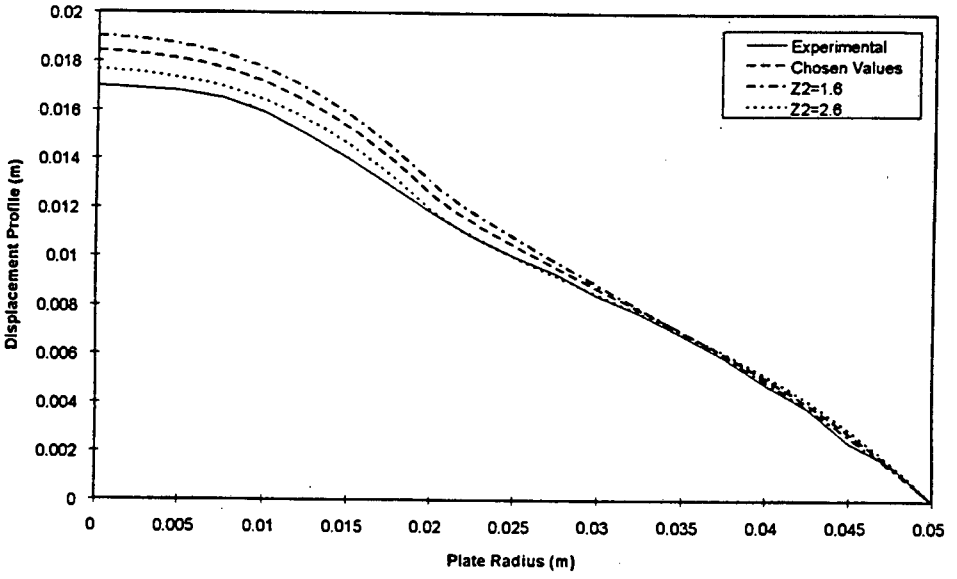

Figure K.19 Affects of varying $Z2$ on the displacement profile for a load diameter of 40mm, plate diameter 100mm and impulse of 8.04 Ns.

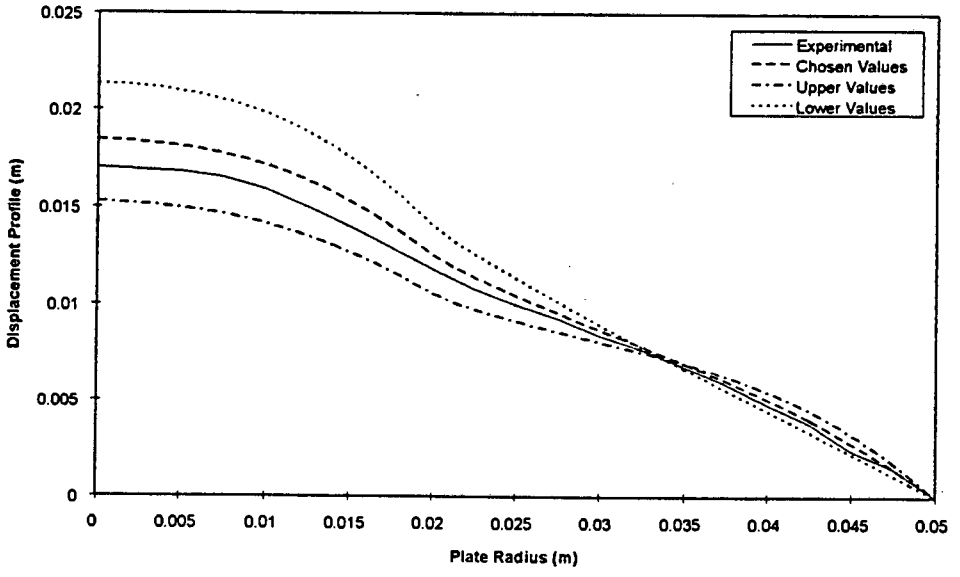

Figure K.20 Combined affects of varying φ_1, φ_2, $Z1$ and $Z2$ on the displacement profile for a load diameter of 40mm, plate diameter 100mm and impulse of 8.04 Ns.